UNIVERSITA' DEGLI STUDI DI MILANO

Doctorate School in Industrial Chemistry

Iron oxide nanoparticles and nanocomposites: a diffractometric study

Supervisor: Dr. Marco SCAVINI

Co-Supervisor: Prof. Cesare OLIVA

Ph.D. thesis by

Paolo Giuseppe Masala

A. Y. 2013/2014

to my father

Abstract

Iron oxide nanoparticles and nanocomposites: a diffractometric study

By

Paolo Masala

Nanosized magnetic structures are currently key materials for advancements in electronics, optoelectronics, magnetic storage, and many bio-inspired applications. What is usually termed ‘‘nanostructured systems’’ comprises those materials whose properties are determined by particles, crystallites, or clusters with characteristic lengths between about 1 and 100 nm. If the grain or domain size becomes comparable or smaller to the characteristic length scale of the interaction processes controlling a particular property, different effects and unusual chemical and physical properties can be expected that are highly attractive in a number of technical applications. In recent times, large advancements have been achieved related to the synthesis and characterization of well-defined, discrete magnetic nanoparticles for both fundamental and technological purposes. However, precise knowledge of the relationships between particle shape and size distribution, surface structure, and the resulting magnetic properties of magnetic nanoparticles is still lacking.

In particular, iron oxide nanoparticles have been the subject of many theoretical and experimental studies.

The goal of this thesis is to provide a crystallographic structural description of the atomic rearrangements in superparamagnetic maghemite (γ-Fe_2O_3) nanoparticles and in magneto-

plasmonic nano heterostructures formed by metallic gold and magnetite (Fe_3O_4), looking for a relationship between the structure and the properties.

The thesis is organized in 3 chapters.

The first chapter is divided in two part: in the first a briefly introduction about nanomaterials is presented, in the second one all the used techniques are described. First the main concepts about powder diffraction are briefly recalled, then the Pair Distribution Function method is introduced, then there is a description of theory about Small angle X-Ray Scattering and finally ESR theory is shortly presented.

In the second chapter all the beamlines of the European Synchrotron Radiation Facility, used for the data collection, are described.

The heart of the thesis consists in the last chapter where all the data and the results about nanomaterials (γ-Fe_2O_3) and nanocomposites (Au-Fe_3O_4) are shown. In this chapter a thorough structural characterization was performed by using X-ray powder diffraction by means of conventional Rietveld analysis, Pair Distribution Function and Small Angle X-ray Scattering; in addition Electron Spin Resonance spectroscopy was performed on the systems to shed light on their magnetic properties.

Table of Contents

1. INTRODUCTION and TECHNIQUES

1.1 Nanomaterials and Nanocomposites

Nanomaterials are the foundation of nanoscience and nanotechnology and have become one of the most important field in a very short period **[1]**. Materials constituted by particles in the range of 1-100 nm are prepared and used since a long time, but it is in the last 20 years that it was possible to understand and describe their exceptional properties. The small dimensions of the particles make their properties different from bulk materials for several reasons. In particular:

- most atoms lie on the surface;
- surface free energy has an important role in the thermodynamics of nanoparticles;
- some assumptions of band theory are no longer valid (e.g. continuity of density of states).

Furthermore, during last decades there has been an improvement in the miniaturization technique and in the engineering of components, with the possibility to obtain components smaller and smaller. One of the main reason for this field of research is that materials show different properties

when their dimension is below the critical length scale associated with any given properties. These scales do not apply only to the external structure of the material but also in the internal structure and it is well known that properties of material strongly depend on their microstructure. Microstructure includes all aspect of atomic arrangement, compositional inhomogeneity, the amount of the phases in the material, the grain size and its distribution and the shape, the concentration and distribution of crystal defects as vacancies, dislocation, stacking and twin faults and lattice distortion due to strain. Materials with nanoscale size, where most of the grain size is below 100nm, have been classified by Siegel **[2]** with the following classification, which is shown in **Fig. 1.1**.

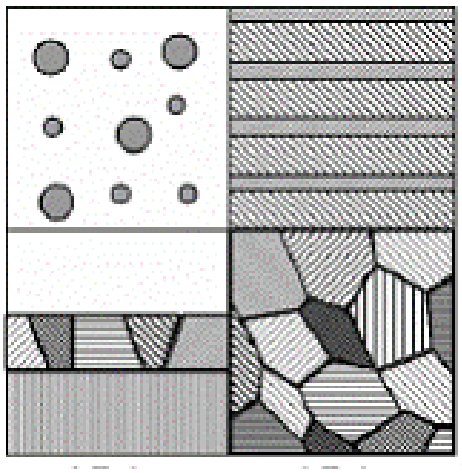

Figure 1.1: Siegel's classification: zero-dimensional system (up left), one-dimensional system (up right), two-dimensional system (bottom left) and three-dimensional system (bottom right).

The first category is zero-dimensional (0D) system, e. g. an isolated nanoparticle embedded into a matrix. Objects with alternating coherent domains of nanometer thickness are one-dimensional (1D) system (nanotubes, nanowires, nanorods). Films supported on a carrier are the best example for two-dimensional (2D) materials. Finally, there are the three-dimensional (3D) systems represented by materials with coherently scattering domains of a few nanometers in size.

Nanocrystalline materials have generated large interest in the last two decades in terms of challenges in the fundamental science and for their potential for technological applications **[3-5]**;

catalysts, nanoceramics, and nanocrystalline heat-resisting alloys represent only a small amount of materials widely used in different fields of science and technology with industrial interest. Of particular interest are the scaling laws related to mechanical, electrical, magnetic and corrosion properties. Inter-crystalline region becomes important when the grain size is below 100 nm, often resulting in unusual properties at the smallest grain sizes. It is important to note that the strength of nanocrystalline materials depends also on the width and the shape of the grain distribution function and it is not determined only by the grain size **[6]**.

During the last 10 years researchers have begun to explore nanocomposites.

Nanocomposites are composed by multiple phases, where each phase is selected for a specific goal. The researchers have begun to explore heterostructured nanoparticles by integrating multiple nanoparticle components assembling into a single nanocomposite **[7-11]**. Double-components systems received much attention because of the improve properties in respect to single constituents **[11,12]**, an import advance in nanotechnology and in the comprehension of nanoscale phenomena. None of such unusual effects could be otherwise accessed with any of the single components alone or their physical mixture counterparts **[13,14]**.

References

[1] G. Cao, *"Nanostructures and Nanomaterials"*, **2004**, Imperial College Press, London, England

[2] R.W. Siegel, *Proc. of NATO ASI*, **1993**, 233, 509

[3] K.S. Kumar, H. Van Swyggenhoven, S. Suresh, *Acta Mater.*, **2003**, 51, 5743

[4] M.A. Meyers, A. Mishra, D.J. Benson, *Prog. Mater. Sci.*, **2006**, 51, 427

[5] M. Dao, L. Lu, R.J. Asaro, J.T.M. De Hosson, E. Ma, *Acta Mater.*, **2007**, 55, 4041

[6] Y.M. Wang, E. Ma, *Acta Mater.*, **2004**, 52, 1699

[7] Z. Xu, Y. Hou and S. Sun, *J.Am. Chem. Soc.* **2007**, 129, 8698-8699

[8] L. Wang, J. Luo, Q. Fan, M. Suzuki, I.S. Suzuki, M.H. Engelhard, Y. Lin, N. Kim, J.Q. Wang and C.J. Zhong, *J. Phys. Chem. B* **2005**, 109, 21593-21601

[9] C. Xu, J. Xie, D. Ho, C. Wang, N. Kohler, E.G. Walsh, J.R. Morgan, Y.E. Chin and S. Sun, *Angew. Chem. Int. Ed.* **2008**, 47, 173-176

[10] E.V. Shevchenko, M.I. Bodnarchuk, M.V. Kovalenko, D.V. Talapin, R.K. Smith, S. Aloni, W. Heiss and A.P. Alivisatos, *Adv. Mater.* **2008**, 20, 4323-4329

[11] K.L. Krycka, J.A. Borchers, G. Salazar-Alvarez, A. Lopez-Ortega, M. Estrader, S. Estrade, E. Winkler, R.D. Zysler, J. Sort, F. Peirò, M.D. Barò, C.C. Kao and J. Nogues, *ACS Nano* **2013**, 7, 921-931

[12] J.J. Urban, D.V: Talapin, E.V. Shevchenko, C.R. Kagan and C.B. Murray, *Nat. Mater.* **2007**, 6, 115

[13] F. Pineider, C. de Julian Fernandez, V. Videtta, E. Carlino, A. al Hourani, F. Wilhelm, A. Rogalev, P.D. Cozzoli, P. Ghigna and C. Sangregorio, *ACS Nano* **2013**, 7, 857-866

[14] M.B. Cortie, A.M. McDonagh, *Chem. Rev.* **2011**, 112, 3713-3735

1.2 X-Ray Diffraction

Diffraction techniques are powerful tools to investigate, in a non-destructive way, the microstructure of even the smallest engineering components. The most common used X-ray diffraction techniques in material science include:

- *Bragg diffraction*: crystal structure, residual stress, texture, size distribution;
- *Pair Distribution Function*: real space arrangement of atoms over a wide *r*-range;
- *Small-angle scattering*: particle shape, size distribution, volume fraction;
- *Quasielastic diffuse scattering*: local atomic arrangements in glasses and amorphous systems, chemical disorder, strain fields in impurity;
- *Fluorescence*: quantitative analysis of elements;
- *Imaging techniques*: radiography, topography, tomography, coherent diffraction imaging.

In this section we will show the basic concepts related to the X-ray diffraction techniques. We will show a general overview on the diffraction theory, present the *pair distribution function* together with the procedure to analyze the total scattering from powder diffraction data and, finally, the *small angle X-ray scattering* and *electron spin resonance spectroscopy* theory.

1.2.1 X-Ray Powder Diffraction

X-Ray Powder Diffraction (XRPD) is nowadays a routine technique for the characterization of crystalline materials. It is possible to extract a large amount of structural information with an accurate study of the diffraction data, not only the determination and the quantification of the crystalline phases. To obtain this kind of information, sometimes given by little modifications in the diffraction pattern, such as variations in the peak intensity, peak splitting or little peak growing up in the background, high quality data are needed. Therefore, their detection is often precluded using laboratory instruments, because of their limited resolution and signal to noise ratio, so that synchrotron radiation, which has high brilliance, a small instrumental contribution to peak broadening and a high signal to noise ratio, is needed.

X-Ray Powder Diffraction is based on powdered material and its randomly distribution of the crystallites. If this powder is an aggregate of randomly oriented crystallites, the vector r_H^*, a reciprocal lattice point (see section "**1.2.2 Reciprocal Space Analysis**"), is in all the possible orientations with respect to the X-ray beam producing the diffraction cone, as shown in **Fig. 1.2**. This cone represents all the possible directions in which diffraction is observed.

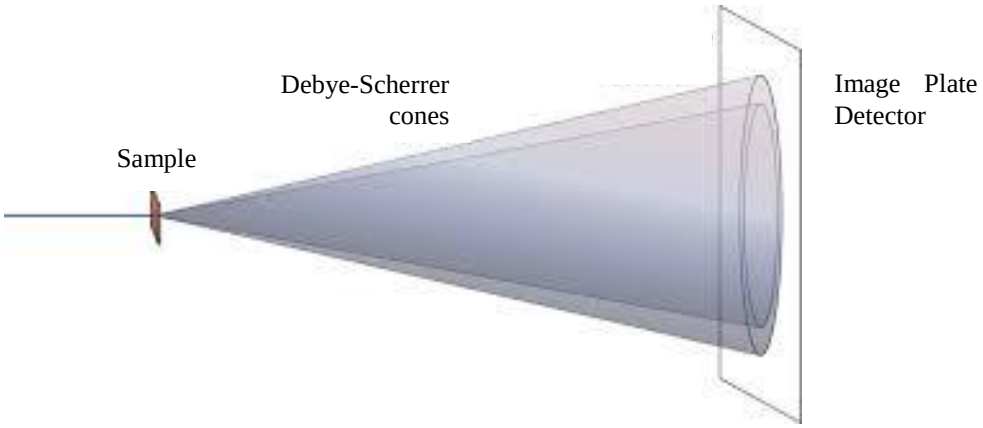

Figure 1.2: Diffraction cones produced by a sample in a X-ray diffraction experiment.

Presently, diffraction cones, which contain the structural information, are detected in two different ways:

a) The first one is by using a two-dimensional detector perpendicular to the incident beam. We know that the diffraction cones "draw" on the detector a series of rings, the so called Debye rings. If the crystallites are really randomly oriented, their distribution will be isotropic and the diffracted intensity in each ring will be homogeneous. In this case, a section of the diffraction rings can be considered representative of the reflection intensity profile in the reciprocal space.

b) The second one is by using a point detector. Most of the modern instruments use this latter detector geometry to measure the intensity and the position in 2θ of the diffraction pattern.

The structural investigations can be performed both in the reciprocal space and in the real space. The former is the conventional crystallographic method to determine the atomic structure in a crystal. The latter is the so called *Pair Distribution Function* (PDF) method, which describes the atomic arrangement looking at the interatomic distances.

In the next sections a few basics concepts of reciprocal and real space are in depth introduced.

1.2.2 Reciprocal Space Analysis

Between the ultraviolet region and the γ-rays region there are X-rays. X-ray are electromagnetic radiation with a wavelength (λ) ranged from 0.1-10 Å, which include the typical interatomic distances values. For this reason X-rays radiation is the perfect tool to study materials from a structural point of view.

If we place in an electromagnetic field of monochromatic X-ray beam an electron, a particle with mass and electric charge, this particle will oscillate with the same frequency of the electric field and will start to emit radiation by a scattering process because of the acceleration of the electron, and the same occurs in polyelectronic systems like an atom or a sample.

In **Fig. 1.3** a schematic process is shown.

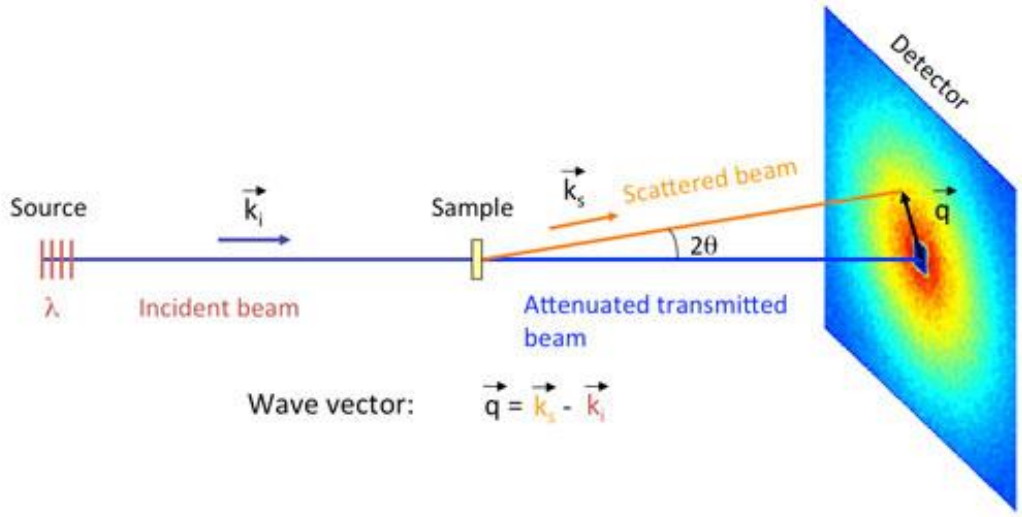

Figure 1.3: Scattering vector.

By defining as k_0 and k_f the wave-vectors associated to the incoming and diffused photon, the difference between the two is given by:

$$Q = k_f - k_0 \qquad \text{Eq. 1.1}$$

A full treatment of the radiation-matter interaction is given, for example, in **[1]**. Here only some useful concepts are introduced.

According to the approximation of elastic scattering (Thompson scattering), since momentum is conserved, the *Q* vector can be replaced by its modulus:

$$Q = |Q| = 2ksin\theta = 4\pi\frac{sin\theta}{\lambda} \qquad \text{Eq. 1.2}$$

On the other hand, when the X-rays are scattered inelastically (and incoherently), i. e. losing some energy of the incident beam, we have Compton scattering. In this case there is a difference in λ between the incident and the scattered radiation because the incident beam transfers a part of its energy to the electron during the collision. The Compton formula is:

$$\Delta\lambda = \left(\frac{h}{m_e c}\right) * (1 - cos2\theta) \qquad \text{Eq. 1.3}$$

where *h* is the Planck constant, m_e is the rest mass of the electron, *c* is the speed of light and 2θ is the scattering angle.

The amplitude of the interference curve given by the scattering from electrons of a single atom (normalized in respect to the scattering from a free electron) is generally defined as the atomic scattering factor *f* and we have a fully constructive interference only in the case of $Q = 0$, then it decays by reason of the spatial distribution of the electrons. So, if we have different scattering points in an atom, we can easily express the total amplitude of the scattered wave as:

$$F(Q) = \sum_{j=1}^{N} A_j exp\,(2\,\pi i * Qr_j) \qquad \text{Eq. 1.4}$$

where A_j stands for the amplitude of the wave scattered by the j^{th} point.

When a continuous distribution of charge density $\rho(r)$ is considered instead of a finite number of scattering centers and, now, we can rewrite the previous equation as following :

$$F(Q) = \int_V \rho(r)\exp\,(2\pi i * Qr)dr \qquad \text{Eq. 1.5}$$

Hence, the amplitude *F(Q)* is the Fourier Transform (FT) of the *ρ(r)* function and the same is for an atom where the atomic scattering factor denoted as *f* which defines the electron density. An analytical description of the scattering factors is given for example in **[2]**.

The amplitude and the phase of the atomic scattering factor defined above is modified by the so called "anomalous scattering" *f'* and *f''* so that *f*(Q) becomes:

$$f(Q,E) = f^0(Q) + f'(E) + if''(E) \qquad \text{Eq. 1.6}$$

f' and *f''* depend on energy E (not on Q) and they vary steeply when E is close to an absorption edge of the atoms involved.

Suitable values for anomalous scattering are given in **[3]**.

The observed diffracted intensity depends on the atomic coordinates and is proportional to the square modulus of the structure factor *F*,

$$I \div |F(Q)|^2 \qquad \text{Eq. 1.7}$$

with *F(Q)* defined as:

$$F(Q) = \sum_{j=1}^{atoms} T_j\, f_j exp\left[2\pi i Q r_j\right] \qquad \text{Eq. 1.8}$$

where r_j defines the atomic positions and T_j accounts for thermal vibration and every further possible delocalization of the electronic cloud. This is true for every set of atoms, even in the absence of any symmetry rule. In the case of a crystalline material, the whole crystal can be described using the translation of a single unit cell according to linear combinations of the translational vectors **a**, **b** and **c**. The edges *a*, *b* e *c* of the unit cell and the angles α, β e γ between couples of vectors are defined as the cell parameters. As a consequence, the structure factor of equation 1.8 can be described as the product of two different summations:

$$F(Q) = \left(\sum_{j=1}^{atoms} T_j \, f_j exp\left[2\pi i Q r_j\right] \right) \left(\sum_{n=1}^{M} exp\left[2\pi i Q R_n\right] \right) \qquad \text{Eq. 1.9}$$

where $\mathbf{R}_n = u\mathbf{a} + v\mathbf{b} + w\mathbf{c}$, with *u, v, w* integers. The first one runs over the *N* atoms *j* in the unit cell, while the second summation stands for the sum over all the cells in the crystal. The condition to have a non-null value in the latter summation is that the product is an integer number, and this is valid only when *Q* corresponds to a reciprocal space vector r_H^*:

$$QR_n = r_H^* R_n = (ha^* + kb^* + lc^*)(ua + vb + wc) = hu + kv + lw \qquad \text{Eq. 1.10}$$

where *h, k, l* are integer numbers. These integers are called the Miller indexes and are used to identify the points of the reciprocal lattice as well as the families of crystallographic planes, perpendicular to r_H^* vectors.

Another method to obtain the diffraction conditions was proposed by W. L. Bragg with the so called Bragg equation which can be written as:

$$2d * sin\theta = n\lambda \qquad \text{Eq. 1.11}$$

In Bragg view, photons of wavelength λ are scattered by families of crystallographic planes, parallel to each other and separated by constant interplanar distances. In Bragg equation, *d* is the interplanar spacing between two consecutive parallel lattice planes, θ is the angle between the incident beam and the family of lattice planes and *n* is the diffraction order. On the basis of equation 1.11 scattering conditions are fulfilled when the path difference between waves reflected from successive planes must be an integer multiple of the wavelength of the incident radiation. As above reported, each plane is characterized by a tern of Miller indexes (*hkl*); the *hkl* plane closest to the origin of crystallographic axes crosses the *a*, *b* and *c* axes at 1/*h*, 1/*k* and 1/*l* of their length. In **Fig. 1.4(a)** is shown the unit cell of gold (Face Centered Cubic structure, *Fm*-3*m* space group) as

well as two [111] planes; in **Fig. 1.4(b)** is displayed a portion of gold X-ray powder diffraction pattern. Numbers into brackets are the miller indexes.

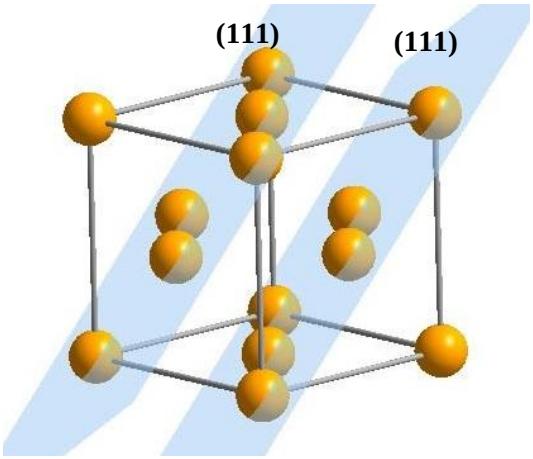

Figure 1.4(a): Structure of gold cell: yellow balls represent gold atoms. Two parallel [111] planes are shown.

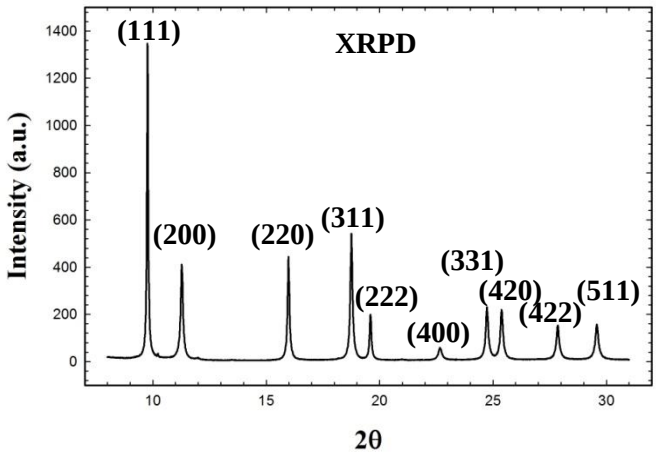

Figure 1.4(b): XRPD pattern of gold. The corresponding Miller indexes are indicated.

One interesting feature of the XRPD pattern, shown in **Fig. 1.4(b)** is that the diffracted intensity decays with 2θ.

This effect is originated by the time averaged spatial distribution of electron density. One hand, the finite distributed of atomic electron density causes the decay of atomic form factors f at increasing 2θ; moreover, in real materials (even at 0 K), atomic vibrations induce a more spread distribution of the electronic cloud, thus producing an even faster intensity decay with 2θ. This effect is accounted for by the parameter T_j:

$$T_j = \exp\left[-8\pi^2 U^2 \left(\frac{sin\theta}{\lambda}\right)\right] \qquad \text{Eq. 1.12}$$

formerly introduced in equation 1.8 when defining the structure factor. In equation 1.12 U indicates the atomic mean square displacement (*msd*) around the equilibrium position.

The mean square displacement is a powerful tool for the study of disordered systems. Basically, in a disordered system atoms which occupy the same site in different cells can have different

equilibrium positions, which average to the one of the long range structure. As a consequence, the electronic cloud is more dispersed and the effect is, though to a larger extent, the same as a huge atomic vibration. It is possible to detect this effect in a diffraction experiment measuring the increase of the mean square displacements provoked by disorder in respect to a disorder free structure. Thus the thermal parameters can be described as follows **[4]**:

$$\langle msd \rangle^{total} = \langle msd \rangle^{thermal} + \langle msd \rangle^{static} \quad \text{Eq. 1.13}$$

where $\langle msd \rangle^{thermal}$ indicates the effective amplitude of vibration and $\langle msd \rangle^{static}$ is the additive contribution given by static disorder in atomic position. Atomic vibrations reduce the structure factor at increasing *Q*, thus the intensity of a diffraction peak; conversely, there are not effects on its width. The width of a diffraction peak, in fact, depends on two main contributions: one due to instrumental effects, such as axial divergence, distribution of wavelengths and finite size of the beam; another one from the sample, in terms of extended defects, finite grain size, strain effects, dislocations, antiphase boundaries and all other defects. All the defects, affecting the profile of a diffraction peak, are defined as microstructure **[5-6]**.

1.1.2.1 Rietveld Method

It is well know that the Rietveld method **[7]** is the most used structural refinement procedure for 3D-ordered crystalline materials using powder diffraction data. In this work, the structural analysis of all the powder diffraction patterns was performed using this method.

The main idea of this method is to represent the profile of the diffraction peak in the XRPD pattern using some empirically chosen approximation functions with specified or refined parameters. Starting from a given structural model, the peak intensity is varied varying structural parameters. The Rietveld method uses a mathematical model, containing both structural and profile parameters,

to represent the diffraction pattern. The observed intensity y_{oi} at the angle i^{th} is compared to the corresponding calculated as follows:

$$Y_{ci} = S \sum m_k L_k |F_k|^2 P(2\theta_i - \theta_k) O_k A + y_{bi} \qquad \text{Eq. 1.14}$$

where S is a scale factor, m_k is the multiplicity factor, L_k is the Lorentz-polarization factor, F_k is the structure factor for the k reflection, $P(2\theta_i - 2\theta_k)$ is the profile function, where $2\theta_k$ is the calculated Bragg angle corrected for the zero-point shift error, O_k is the correction term for a non-ideal crystallites distribution, A is the linear absorption correction coefficient and y_{bi} is the background intensity related to the i^{th} intensity.

The aim of the Rietveld refinement is to minimize the residual M between the calculated and observed pattern by a non linear least-squares refinement. The M parameter is defined as:

$$M = \sum w_i |y_{oi} - y_{ci}|^2 \qquad \text{Eq. 1.15}$$

where w_i is a weight depending on the standard deviation associated with the peak and with the background intensity.

The agreement between the observations and the calculated pattern can be estimated by several indicators. To evaluate the goodness of Rietveld refinement it is possible to consider the profile (R_p), the weighted (R_{wp}) and the Bragg (R) indicators defined as:

$$R_p = \sum |y_{oi} - y_{ci}| \,/\, \sum y_{oi}$$

$$R_{wp} = \left[M / \sum w_i y_{oi}^2 \right]^{1/2} \qquad \text{Eq. 1.16}$$

$$R = \sum \big| |F_O| - |SF_c| \big| \,/\, \sum |F_O|$$

It is important in the Rietveld method, but no only in it, the determination of the profile function which can be written as:

$$P\ (x) = \ H(x) \otimes f(x) \qquad \text{Eq. 1.17}$$

where $x = 2\theta_i - 2\theta_k$ and the *f(x)* is the specimen function and depends on the specimen characteristic such as defects, size, strain, while *H(x)* is the instrumental function. Many analytical functions are used to describe the peak-shape like Gaussian (*G(x)*), Lorentzian (*L(x)*) functions or convolution of these like Voigt (V) or pseudo-Voigt (pV). The latter, an approximation of Voigt function, is commonly used to take into account both the Gaussian and the Lorentzian contribution to the diffraction peak.

In particular the pseudo-Voigt can be written as:

$$pV(x) = \ \eta L(x) \ + \ (1 - \eta)G(x) \qquad \text{Eq. 1.18}$$

where

$$L(x) = \frac{2}{\pi(FWHM)} * \frac{1}{1 + \frac{4x^2}{(FWHM)^2}} \qquad \text{Eq. 1.19}$$

$$G(x) = \frac{2}{(FWHM)} * \sqrt{\frac{ln2}{\pi}}\ exp\left(-\frac{4ln2}{(FWHM)^2}x^2\right) \qquad \text{Eq. 1.20}$$

where FWHM is the so called *Full Width Half Maximum*, and η ($0 \leq \eta \leq 1$) is the mixing parameter between the gaussian and lorentzian function.

In the Rietveld method the evolution of the line shape as a function of 2θ is obtained refining suitable parameters related to FWHM and η **[8]**.

1.1.2.2 Data Analysis Strategy

In the XRPD patterns the average crystallographic structure was determined through Rietveld method **[9]**, using the software GSAS **[8]** with the graphical interface EXPGUI **[10]**. The line profile and the background were fitted with pseudo-Voigt functions and Chebyschev polynomials accounting for asymmetry correction **[11]**, respectively. Absorption correction, for XRPD data, was performed through the Lobanov empirical formula **[12]**. Anomalous scattering was taken into account using the *f'* and *f''* parameters given by [**13**].

In the refinements we varied cell parameters, oxygen position and, when it is possible, one average isotropic mean square displacement (*msd)* parameter per phase.

1.1.2.3 Williamson-Hall Method

The broadening of the peak in an XRPD pattern is due to instrumental and physical factors. The latter depends on the nature and the chemistry of the sample. In particular the diffraction profile can be represent as the convolution of different contributes depending on the crystallites size and shape, the strain and, in complex case, on the nature and the distribution of defects **[14]**. In this thesis, the analysis is focused in the determination of the crystallites dimension (D_V) and the strain (ε) in the samples presented.

The determination of ε and D_V is obtain by means of the Williamson-Hall (W-H) method. By using a pseudo-Voight function, the method correlates the *Full Width Half Maximum* of a peak with the integral breadth β according to the follow equation:

$$\beta_{pV} = \frac{FWHM}{2} * \left[(1-\eta) * \sqrt{\left(\frac{\pi}{ln2}\right)} + \eta * \pi \right] \qquad \text{Eq. 1.21}$$

D_V and ε parameters can be evaluated using the follow relation **[15, 16]**:

$$\beta * \cos\theta = 4\varepsilon * \sin\theta + \frac{\lambda}{D_V} \qquad \text{Eq. 1.22}$$

According to the equation 1.22, it is possible to extract D_V and ε plotting the value $\beta*cos(\theta)$ as a function of $4*sin(\theta)$. D_V is given by the intercept of the y axis, while the slope of the function gives the value of ε.

To obtain the right value of β_{pV} a correction of the broadening of the peak for the instrumental factor is needed. This process is the so called *instrumental resolution function*.

1.1.2.3.1 Instrumental Resolution Function

The *instrumental resolution function* (IRF) describes the contribution of the broadening of the peak due to the instrumental factors in terms of U, V, W, a, b, c as a function of θ. The parameters are obtained using the follow equations:

$$FWHM^2 = (U * tan^2\theta + V * tan\theta + W) \qquad \text{Eq. 1.23}$$

$$\eta = (a + b * \theta + c * \theta^2) \qquad \text{Eq. 1.24}$$

In order to consider only the instrumental contribute, the IRF is generally achieved collecting an XRPD pattern of a sample without structural defects and with large crystallites. In this chapter, for example, is presented an instrumental resolution function calculated on CeO_2 (Aldrich) at $\lambda = 0.3542$.

In **Fig. 1.5(a)** the trend of $FWHM^2$ as a function of $tan(\theta)$ is shown, while the trend of η as a function of θ is depicted in **Fig. 1.5(b)**. The FWHM and η values have been obtained fitting each peak of Ceria oxide by means of a pseudo-Voight function implemented in the WinPlotr suite of programs **[17]**.

By fitting the results in **Fig. 1.5(a)** and **1.5(b)** with the equations 1.23 and 1.24, respectively, we obtained U, V, W, a, b ,c values required for the calculation of the IRF as a function of θ.

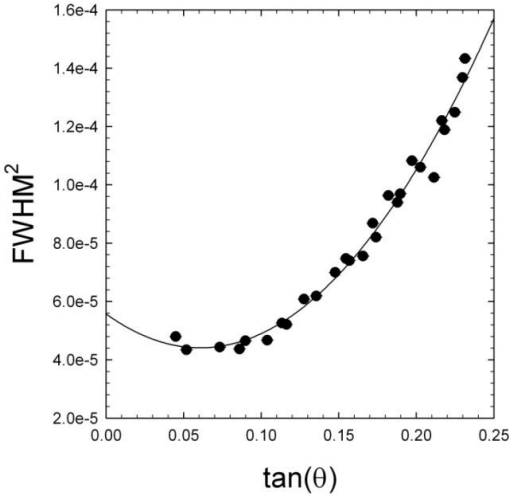

Figure 1.5(a): FWHM^2 as a function of tan(θ).

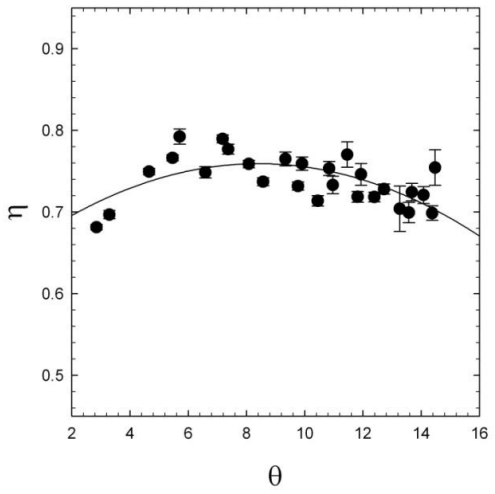

Figure 1.5(b): η as a function of θ.

According to the equation 1.21, now it is possible to subtract, for every sample, the instrumental contribution at the FWHM for every peak. Finally, with the correct β_{pV} it is possible to plot the data in the so called Williamson-Hall plot.

Fig. 1.6 shows an example of W-H plot.

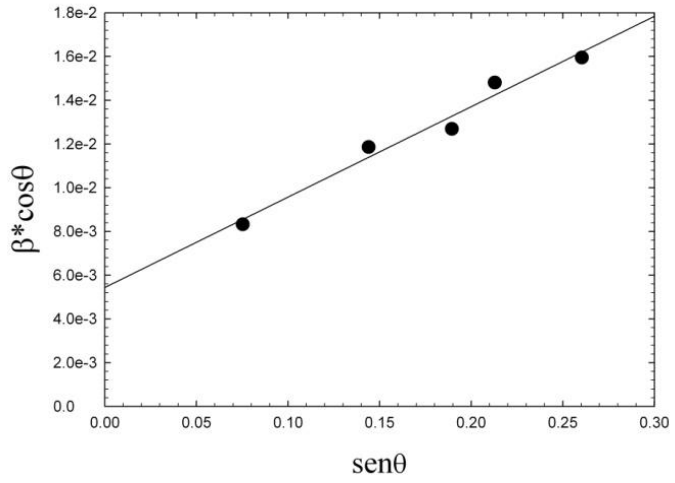

Figure 1.6: W-H plot of gold sample.

1.2.3 Real Space Analysis

Beside the scattering from an ideally periodic arrangement of atoms which, as previously reported, gives rise to the *Bragg* diffraction, there is also the so called *diffuse scattering*. Diffuse scattering is a coherent and quasielastic form of scattering and it is due to same deviations from the periodicity, such as structural disorder or structural modifications with respect to the long range structure, present in same material **[1]**. In the Rietveld analysis every deviation from the periodicity is considered as a background feature and no modeling is generally performed. A more efficient approach to study the structure of a disorder material is to consider the relative positions of atoms in a crystal, instead of the absolute ones. For this reason disorder materials are easier to approach in the real space, the space of the interatomic distances with the so called *Pair Distribution Function*.

1.2.3.1 Pair Distribution Function

The *Pair Distribution Function* (PDF) represents the probability of finding pairs of atoms separated by a distance *r*. See **[18]** for a complete derivation.

The PDF is obtained through Sine Fourier transform of the total scattering function, *S(Q)*, obtained from a powder diffraction experiment after proper normalization and corrections. The first step is the subtraction of the empty capillary and the air contribution, so it is necessary to measure the diffraction pattern of the sample holder and of the empty apparatus. The sum of the Bragg peaks, as previously described, and the diffuse scattering gives the coherent diffracted $I_{coh}(Q)$, which is only a part of the overall diffracted intensity:

$$I_0(Q) = P * A * N[I_{coh}(Q) + I_{inc}(Q) + I_{ms}(Q) + \dots] \quad \text{Eq. 1.25}$$

where *P* is the polarization factor, *A* the absorption coefficient, *N* a normalization factor, $I_{inc}(Q)$ is the incoherent intensity, $I_{ms}(Q)$ is the multiple scattering contribution. It should be noted that, when the measurement is performed at the synchrotron, the polarization factor is very close to the unit.

The other corrections are generally performed with tabulated values. There are suitable corrections in **[19]** for the multiple scattering, which occurs when the incident beam is scattered twice or more time before reaching the detector. Instead for the incoherent scattering, in case of X-ray scattering, it is generally present in the form of Compton scattering and is non-negligible especially when working at high energy. Since it increases with *Q* whilst the coherent intensity decreases, even small error in Compton correction can lead to significant errors in the high-*Q* normalization **[20]**. The theoretical Compton profile can be calculated and subtracted from the measured data. In presence of analyzer crystal on the diffracted beam the Compton scattering at high-*Q* is removed, but in the middle-low-*Q* region this approach is not reliable and in order to remove it the method suggested by Ruland can be applied. In this method the Compton intensity is smoothly attenuated with increasing *Q* by applying a monochromator cut-off function *Y(Q)* with a given window value. The incoherent intensity is then calculated by multiplying the *Y(Q)* with the theoretical Compton profile and subtracted from the experimental data.

Generally other corrections are necessary depending on the instrument set-up, the type of detectors, the experimental condition and the probe employed. Now the coherent diffracted intensity, which is the results of Bragg and diffuse scattering contributions, needs to be normalized in order to obtain the total scattering function, shown in the follow equation:

$$S(Q) = \frac{I_{coh}(Q) - \langle b^2(Q)\rangle + \langle b(Q)\rangle^2}{\langle b(Q)\rangle^2} \qquad \text{Eq. 1.26}$$

Where $\langle b(Q)\rangle^2 = [\sum_i c_i b(Q)_i]^2$ and $\langle b^2(Q)\rangle = \sum_i c_i\ [b(Q)_i]^2$ are the square of mean and the mean of square scattering lengths weighted over the concentration of the i^{th} atom in the sample.

A typical XRPD *S(Q)* and *F(Q)* curves and the *G(r)* calculated of nano-CeO_2 sample are shown in **Fig. 1.7(a)**, **1.7(b)** and **1.7(c)**, respectively.

Where the so-called reduced structure *F(Q)* is derived from *S(Q)*:

$$F(Q) = Q[S(Q) - 1] \qquad \text{Eq. 1.27}$$

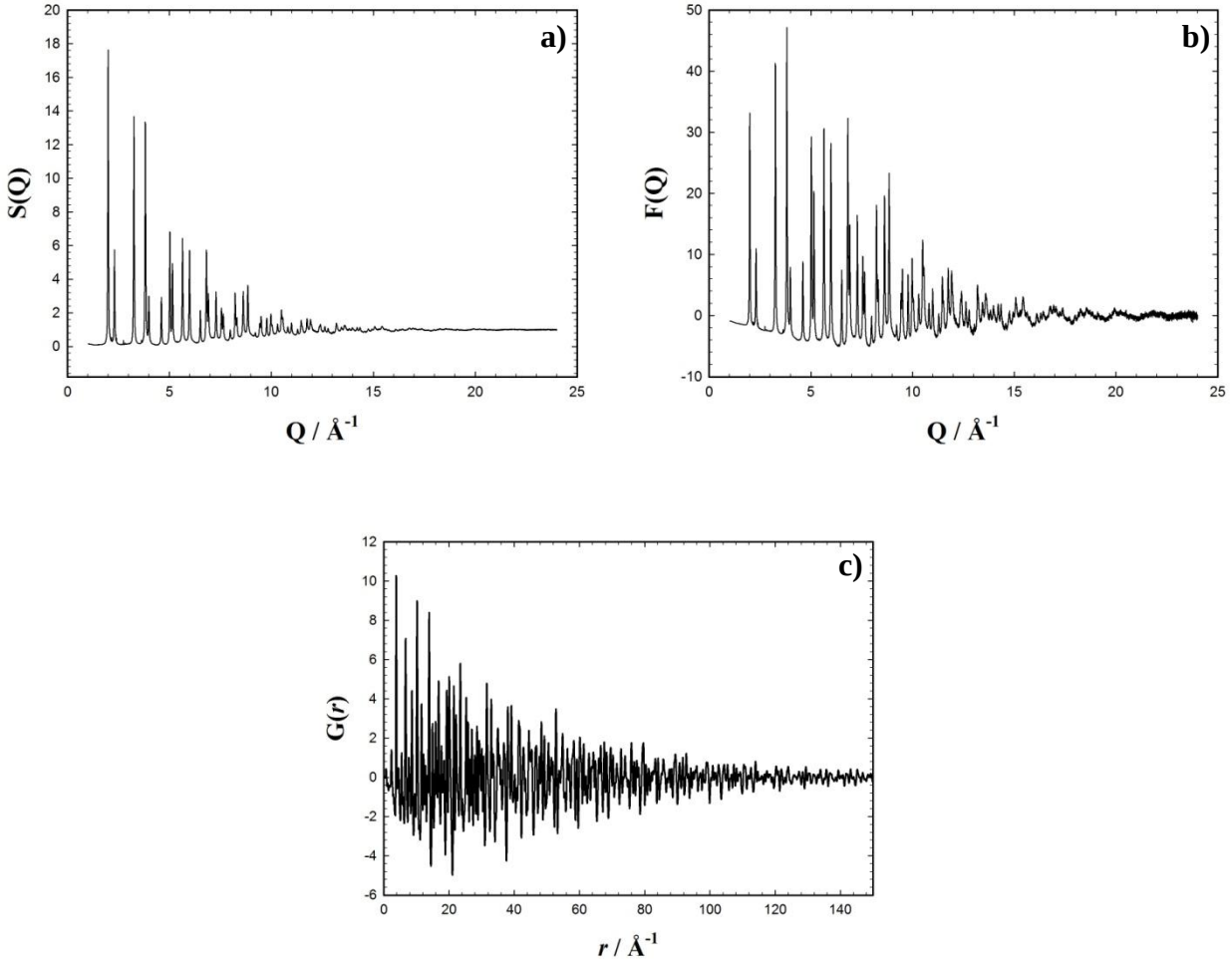

Figure 1.7: a) *S(Q)*, b) *F(Q)* and c) *G(r)* curves determined on nano-CeO_2 sample.

The form of *F(Q)* implies that, at high *Q* values, the dispersion of experimental data around the mean value as well as the noise is magnified.

In the present thesis, we refer to *G(r)*, defined as the sine Fourier Transform of total scattering function *S(Q)*:

$$G(r) = \frac{2}{\pi}\int_0^\infty Q[S(Q) - 1]\sin(Qr)\,dQ = \frac{2}{\pi}\int_0^\infty F(Q)\sin(Qr)\,dQ \qquad \text{Eq. 1.28}$$

It should be noted that many different formalisms are used to describe the pair distribution function and, in general, the distribution of interatomic distances as a function of *r*; an overview on this matter is given by Keen **[21]**. Each positive *G(r)* peak indicates *r* value where the probability of finding two atoms separated by a certain distance is greater than that determined by the so called number density ρ_0, i.e. the number of atoms for $Å^3$. Hence, the *G(r)* gives the probability of finding two atoms separated by a distance *r* averaged over all pairs of atoms in the sample. In this context, the structure of the material is studied in terms of interatomic distances and, since no periodicity is assumed, both the long range structure and the local deviations with respect to this average structure can be explored.

The integration of the equation 1.28 should obtained in an infinite range of *Q*, but this is impossible and the upper limit of the integration is the maximum value of *Q* (Q_{max}) experimentally reached. It depends on the incident wavelength and the maximum 2θ value investigated during the data collection of the experiment. Collecting data up to a certain Q_{max} is equivalent to multiply *S(Q)* by a step function [=1 for $Q<Q_{max}$; = 0 for $Q>Q_{max}$], that in real space produces the convolution of *G(r)* with a broadening function, given by:

$$\frac{\sin(Q_{max}\,\Delta r)}{\Delta r} \qquad \text{Eq. 1.29}$$

corresponding to the Fourier Transform of the step function **[10]**.

The finite value of Q_{max} induces peak broadening and the appearance of spurious oscillations in *G(r)* with wavelength ~ $\frac{2\pi}{Q_{max}}$, the so called *termination ripples*, which are evident, especially, at low *r* (see **Fig. 1.8**).

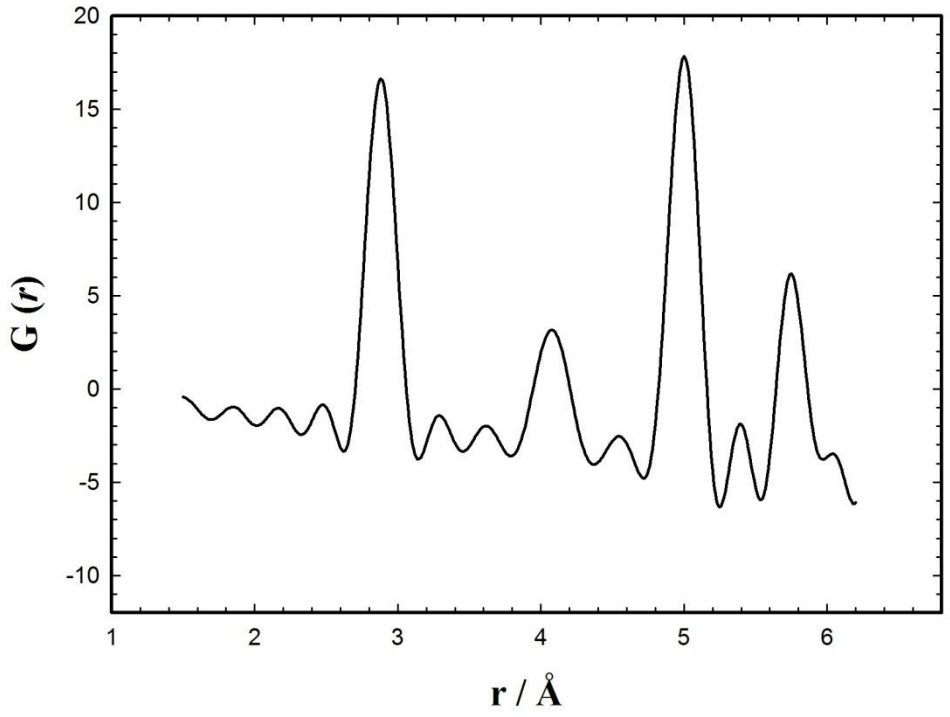

Figure 1.8: *G(r)* of gold with Q_{max} = 20 Å^{-1}. Termination ripples, especially at low *r*, are evident.

At high enough Q_{max} values the truncation induced broadening becomes negligible with respect to the thermal broadening. Increasing Q_{max} also reduces the intensity of the *termination ripples* (see **Fig. 1.9**).

Often it is reported in the literature that suitable *G(r)* functions are obtained when Q_{max} values exceed ~25-30 Å^{-1} in order to minimize the termination effects. However, the correct *Q* range to investigate depends also on the sample nature, the temperature and on the instrument set-up. Surely, collecting data with a limited *Q* range the *G(r)* peaks could be affected by an additional broadening,

which will reduce the resolution in the real space and will change the peak positions. Thus, collecting data at Q_{max} as high as possible seems to be mandatory to obtaining good *G(r)* curves.

In **Fig. 1.9** XRPD *G(r)* curves calculated at different Q_{max} are shown. The green curve refers to a PDF obtainable using a laboratory diffractometer equipped with a Cu anode, which can reaches Q_{max} = 8 Å^{-1}. Modern improvements in laboratory diffractometers give the possibility to mount Mo, or even Ag anode, which allows to access higher Q_{max}, around 16 Å^{-1}. The Ag anode *G(r)* curve is depicted in black. But to obtain higher Q_{max} we need synchrotron facility, and the red curve represented the PDF curve with a Q_{max} = 25 Å^{-1}. All the *G(r)* curves shown in this thesis are collected by ourselves at the *European Synchrotron Radiation Facility* (ESRF). Obviously, some ripples are again present, but they are considerably reduced. To eliminate almost entirely the termination ripples we need to reach Q_{max} = 50 Å^{-1}, the blue curve.

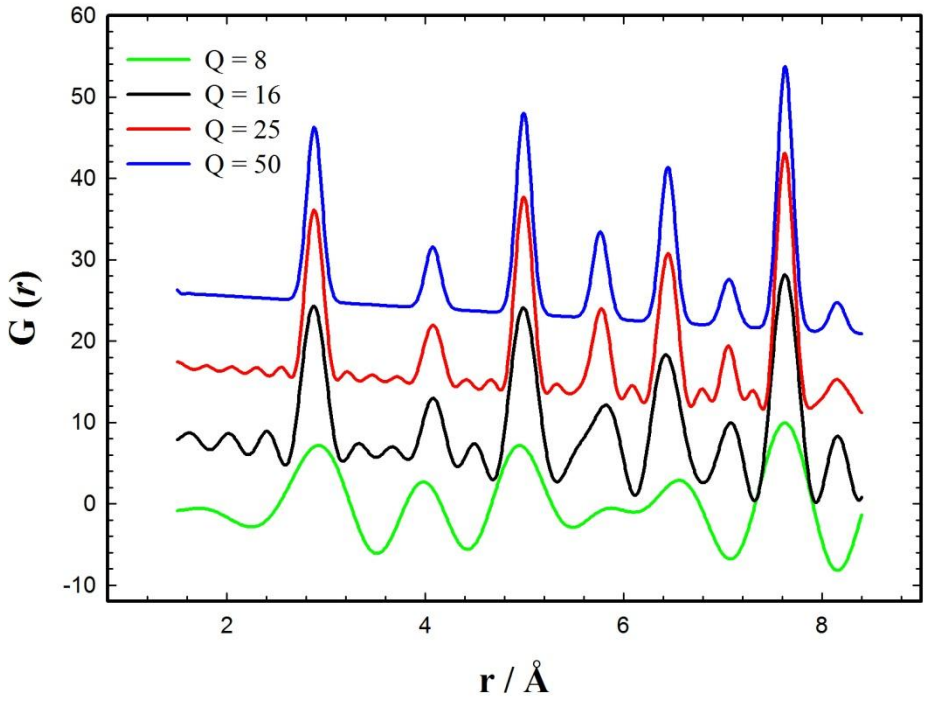

Figure 1.9: Calculated *G(r)* for gold with different Q_{max}. The Q_{max} values indicated are in Å^{-1} units.

However, we have to remind that the atomic form factors *f* decay at increasing *Q*; as a consequence high-*Q* values can be noise. Fourier transforming a *F*(Q) function up to *Q* values, where corresponding to low the intensity-noise ratio introduces spurious oscillations which hinder a correct interpretation of the experimental data. To overcome this problem usually patterns are measured for longer time in the high 2θ ranges; however, due to the finite counting time available to collect diffraction pattern Q_{max} is a compromise between two necessity: minimize truncation error and noise.

Toby and Egami **[10, 13]** provided an experimental rule to evaluate the suitable Q_{max} values: termination effects are negligible when Q_{max} is greater then $\frac{3}{2\langle msd\rangle}$, where $\langle msd\rangle$ is the average mean square displacement. The presence of ripples can also arise by a non-correct high-*Q* normalization, as shown by **[20]**.

As for the data presented in this thesis, full structure profile refinements are carried out using PDF data. The PDF of a given structure can be calculated using the relation**:**

$$G(r) = \frac{1}{r}\sum_i\sum_j\left[\frac{b_i b_j}{\langle b\rangle^2}\delta(r - r_{ij})\right] - 4\pi\rho_0 r \qquad \text{Eq. 1.30}$$

with the sum running over the atoms *i* and *j* separated by a distance r_{ij}. The equation 1.30 does not account for atomic vibrations. For this goal, the delta term can be replaced by a modified Gaussian function **[22]**:

$$T_{ij}(r) = \frac{1}{\sqrt{2\pi}\sigma_{ij}(r)}exp\left[-\frac{(r - r_{ij})^2}{2\sigma_{ij}^2(r)}\right] * \left[1 + \left(\frac{r - r_{ij}}{r_{ij}}\right)\right] \qquad \text{Eq. 1.31}$$

where $\sigma_{ij}(r)$ is related to the *msd* of atoms *i* and *j*. In some cases the 1st neighbors pairs are subjected to correlated motion, which produces a sharpening of some peaks in the low-*r* region. This effect is detailed in **[23]**.

The observed *G(r)* can be then fitted against the calculated *G(r)* ($G^c(r)$) by applying suitable symmetry constrains and varying cell parameters, atomic positions and thermal parameters. The degree of accuracy of the PDF refinement can be assesses by agreement factor of type:

$$R_W = \left[\frac{\sum w_i \, (G_i - G_i^c)^2}{\sum w_i \, (G_i)^2}\right]^{1/2} \qquad \text{Eq. 1.32}$$

where $w_i = 1/\sigma^2(r_i)$ and $\sigma(r_i)$ is the standard deviation at a distance r_i.

In the equation 1.30 all *G(r)* curves have a negative slope in the limit, while, in the limit of large *r*, they tend to zero. Thanks to the damping of the amplitude of the oscillations we have a direct measure of the structural coherence of the sample. For example, when dealing with nanoparticles, for interatomic distances larger than the size of the particle, the coherence is lost and the *G(r)* will fall to zero. It should be noted that the damping is influenced also by the instrumental resolution. In fact, the lower the instrumental resolution, the faster the *G(r)* amplitude decays with *r*. But, generally, the diffractometers resolution are known, and they show a constant *ΔQ/Q* resolution, which can be easily modeled **[18]**.

1.2.3.2 Data Analysis Strategy

XRPD real space data reported in this thesis were processed using the PDFGetX3 software **[24]** and were corrected for background, sample self-absorption, multiple and Compton scattering. For each sample, empty container and sample environment contributions were subtracted from raw data, taking into account attenuation effects **[25]** as well as the incoherent-scattering contribution.

We modeled the experimental *G(r)* function by means of the *Real Space Rietveld* method **[18].** For this purpose we used the software PDFGUI **[26]**. As done with the Rietveld method in the reciprocal space analysis section, some parameters of a structural model are refined against the

experimental *G(r)* curve. The quality of the fit is defined by the agreement factor written in the equation 1.32.

After the modeling, we continued the data analysis with the direct analysis. In this analysis, each *G(r)* peak is fitted, after proper baseline subtraction, with a Gaussian in order to determine its peak position, its width and its area.

References

[1] C. Giacovazzo, *"Fundamentals of crystallography"*, Chap. 2, 3, 4, **2002**, Oxford University Press

[2] D. Waasmaier and A. Kirfel, *Acta Cry*st., **1995**, A51, 416-431

[3] S. Brennan and P.L. Cowan, *Rev. Sci. Instrum*,, **1992**, 63, 850

[4] D.N. Argyriou, *J. Appl. Cryst.*, **1994**, 27, 155-158

[5] E.J. Mittemeijer and P. Scardi, "*Diffraction Analysis of the Microstructure of Materials*", **2004**, Springer

[6] R.L. Snyder, J. Fiala and H.J. Bunge, "*Defect and Microstructure Analysis by Diffraction*", **1999**, Oxford University Press

[7] H.M. Rietveld, *J. Appl. Cryst.*, **1969**, 2, 65

[8] A.C. Larson and R.B. Von dreele, *General Structure Analysis System (GSAS)*, Los Alamos National Laboratory Report LAUR, **2004**, 86-748

[9] R.A. Young, "*The Rietveld method*", **1993**, Oxford University Press

[10] B.H. Toby and T. Egami, *Acta Cryst.*, **1992**, A48, 336-346

[11] L.W. Finger, D.E. Cox and A.P. Jephcoat, *J. Appl. Cryst.*, **1994**, 27, 892-900

[12] N.N. Lobanov and L. Alte de Veiga, *6th European Powder Diffraction Conference*, **1998**, Abstract P12-16

[13] T. Egami, *Z. Kristallogr.*, **2004**, 219, 122-129

[14] S. Brandstetter et al., *Acta Materialia*, **2008**, 56, 165

[15] O.J. Durà et al., *J. Phys.D. : Appl. Phys.*, **2008**, 41, 1

[16] H. Mandar et al., *J. Appl. Cryst.*, **1999**, 32, 345

[17] T. Roisnel and J. Rodriguez-Carvajal, *Materials Science Forum, Proceedings of the European Powder Diffraction Conference (EPDIC7)*, **2001**, 378-381, 118-123

[18] T. Egami and S.J.L. Billinge, "*Underneath the Bragg peaks*", **2003**, Pergamon

[19] C.W. Dwiggins and D.A. Park, *Acta Cryst.*, **1971**, A27, 264

[20] P.F. Peterson, E.S. Bozin, T. Proffen and S.J.L. Billinge, *J. Appl. Cryst.*, **2003**, 36, 53-64

[21] D.A. Keen, *J. Appl. Cryst*, **2001**, 34, 172-177

[22] R.B. Neder and T. Proffen, "*Diffuse scattering and defect structure simulations: a cook book using the program DISCUS*", **2009**, Oxford University Press

[23] I.K. Jeong, T. Proffen, F. Mohiuddin-Jacobs and S.J.L. Billinge, *J. Phys. Chem. A*, **1999**, 103, 921-924

[24] P. Juhas, T. Davis, C.L. Farrow and S.J.L. Billinge, *J. Appl. Cryst.*, **2013**, 46, 560-566

[25] M.A. Howe, R.L. McGreevy and P. Zetterstrom, **1996**, NFL Studsvik internal report

[26] C.L. Farrow, P. Juhàs, J.W. Liu, D. Bryndin, E.S. Bozin, J. Bloch, T. Proffen and S.J.L. Billinge, *J. Phys.: Condens. Matter*, **2007**, 19, 335219

1.3 Small-Angle X-ray Scattering (SAXS)

The *Small-Angle X-ray Scattering* (SAXS) is a powerful technique for studying nanostructures and nanostructured materials with characteristic length scales ranging from 1 up to 100 nm. It is possible to determine with a quantitative SAXS analysis crucial information such as the average size, size distribution and shape of the particles of the studied material.

The most important SAXS equations are described in detail in this chapter. For a fulfill discussion about the scattering theory the reader is referred to the textbook **[1]**.

1.3.1 Introduction

SAXS equations are derived from the scattering theory using the following approximations: (1) the system is statistically isotropic and (2) there exist no long-range order. According to restrictions (1) and (2) the intensity can be written as:

$$I(Q) = 4\pi \int \frac{\sin(Qr)}{Qr}\gamma(r)r^2 dr \qquad \text{Eq. 1.33}$$

where $\gamma(r)$ is the probability of finding a point within a particle at distance r from a given point (in the same particle) and it is equal to zero at $r \geq D$, where D is the larger distance between two point within the same nanoparticle.

The intensity is related to the volume and the shape of the scattering object. So that, via SAXS, it is possible to obtain the shape of the scattering object by inverse Fourier Transform of the measured intensity.

Equation 1.33 applies in case of a single scattering particle, but, obviously, real systems are more complex and include a huge number of particles. In the case of a dilute solution, the total diffraction pattern is simply the sum of the intensity scattered by individual particles. But, if we increase the concentration, interparticle interference becomes not negligible. This interference is due to the impenetrability of the particles and to the electrostatic Coulomb force.

A system of volume V with N similar particles is the simplest case. By increasing the concentration, the interparticle interference for each particle becomes stronger. The scattered intensity from all the particles can be written as:

$$\frac{d\sum(Q)}{d\Omega} = \frac{1}{V}\frac{d\sigma}{d\Omega} = \frac{1}{V}\sum_{k=1}^{N}\langle|f_k(Q)|^2\rangle + \frac{1}{V}\langle\sum_{k=1}^{N}\sum_{J=1}^{N} f_k(Q)f_k^*(Q)e^{-iQ(r_k - r_j)}\rangle \qquad \text{Eq. 1.34}$$

where r_k and r_j are the centers of mass of particle k and j, respectively, and $d\sigma/d\Omega$ is the differential scattering cross section defined as:

$$\frac{d\sigma}{d\Omega} = \frac{(number\ of\ scattered\ photons/s)}{(incident\ flux)} \qquad \text{Eq. 1.35}$$

But for monodispersed spherical particles we have $f(Q) = f_k(Q) = f_j(Q)$. According to this, the previous equation can be rewritten as:

$$\frac{d\sum(Q)}{d\Omega} = \frac{N}{V}\langle|f(Q)|^2\rangle\left\{1 + \langle\sum_{k=1}^{N}\sum_{j=1}^{N} e^{-iQ(r_k - r_j)}\rangle\right\} \qquad \text{Eq. 1.36}$$

In equation 1.36 the scattered intensity is composed of two parts: the first one is the interparticle interference factor, called the *form factor P(Q)*; the second one arises from the interparticle interference and is called *structure factor S(Q)*. Equation 1.36 can be rewritten as:

$$\frac{d\sum(Q)}{d\Omega} = \frac{N}{V}\frac{d\sigma}{d\Omega} = NV^2\Delta\rho^2 P(Q)S(Q) \qquad \text{Eq. 1.37}$$

this equation represents the most general form of the SAXS equations.

In the next section the Guinier approximation is presented.

1.3.2 Guinier Approximation

If we take a SAXS pattern, we can divide it in two regions: the low-*Q* and the high-*Q* region (see **Fig. 1.10**).

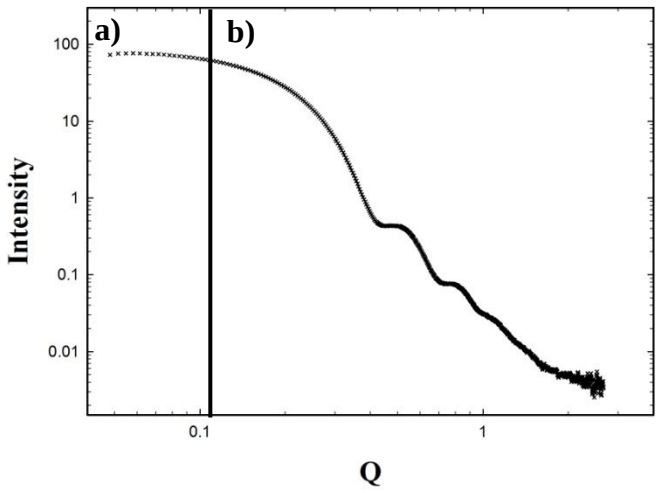

Figure 1.10: a) the low-*Q* and b) the high-*Q* region of a SAXS pattern.

At very low-*Q* values, the diffraction data are insensitive to details at atomic or molecular level. In a system of (ideally identical) particles without long-range order, it is possible to obtain their particle dimension throughout the Guinier equation, which can be derived as follows:

$$\frac{\sin(Qr)}{Qr} = 1 - \frac{Q^2r^2}{6} + \frac{Q^4r^4}{120} - \ \ldots \qquad \text{Eq. 1.38}$$

Combining the equation 1.33 and 1.38 as:

$$I(Q) = I(0)\left(1 - \frac{Q^2R_g^2}{3}\right) \qquad \text{Eq. 1.39}$$

where *I(0)* is:

$$I(0) = 4\pi \int \gamma(r)r^2dr \qquad \text{Eq. 1.40}$$

and the gyration radius *Rg* is:

$$R_g^2 = \frac{\frac{1}{2}\int \gamma(r)r^4\,dr}{\int \gamma(r)r^2\,dr} \qquad \text{Eq. 1.41}$$

Now it is possible to describe the scattering curve at low-*Q* values using the so called Guinier equation:

$$I(Q) = I(0)exp\left(\frac{Q^2 * R_g^2}{3}\right) \qquad \text{Eq. 1.42}$$

It is important to fulfill the terms of the restrictions (1) and (2), by remembering that the Guinier approximation is only valid for dilute solution of monodispersed objects and not valid for concentrated or polydispersed systems.

1.3.3 Shape, Size and Size-Distribution Function

The quantitative analysis of SAXS patterns provides information about the object shape and the size-distribution function of the sample (not only on the average nanoparticles size).

According to equation 1.37, the SAXS intensity can be described as the product between the form and the structure factors. In a dilute solution *S(Q)* is equal to one and can be neglected.

Instead, according to equation 1.33 the scattering cross-section is related to the object shape via the function *γ(r)*:

$$\frac{d\sigma}{d\Omega} = 4\pi \int_0^\infty \gamma(r) r^2 \frac{\sin Qr}{Qr} dr \qquad \text{Eq. 1.43}$$

In this chapter we will focus only on the classic spherical shape. We describe this shape because it is the easiest example to understand and to explain the information contained in a SAXS intensity profile.

Equation 1.43 can be analytically solved and it is equal to the Rayleigh function:

$$\frac{d\sigma}{d\Omega} = N(\Delta\rho)^2 V^2 P_{sph}(Q,R) = N(\Delta\rho)^2 V^2 \left[\frac{3(\sin QR - QR\ \cos QR}{(QR)^3}\right]^2 \qquad \text{Eq. 1.44}$$

where *N* is the number of spheres in solution, $\Delta\rho^2$ is the electron density difference between the spherical objects and the solvent and *R* is the radius of the spheres.

Terms between squared bracket are the sphere form factor $P_{sph}(Q,R)$ and *Q* is the module of the scattering vector.

In **Fig. 1.11** the intensity for different values of *R* are shown. Looking at the plots some observations can be made: i) for monodispersed spherical objects, the form factor is characterized by a series of minima with *I(q)* = 0 and ii) the position of these minima shift toward smaller *Q* values by increasing *R*.

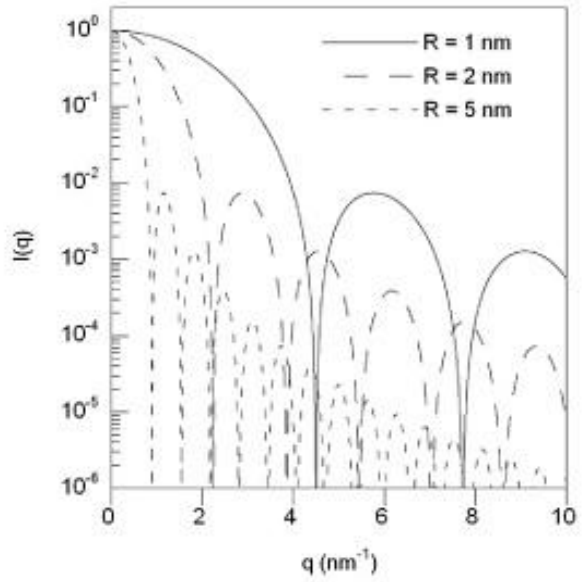

Figure 1.11: Semilogarithmic plot of the form factor for spheres with different radius *R*.

Let us consider an ensemble of spherical objects but with size polydispersity. Its SAXS pattern can be imagined as the sum of spheres with different *R* (see **Fig. 1.12**).

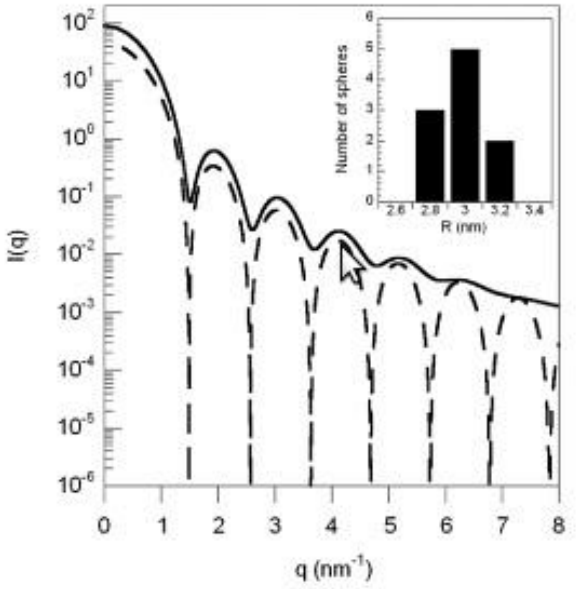

Figure 1.12: Simulated intensity (continuous line) for a mixture of 10 spheres: three of radius 2.8 nm, five of 3 nm and two of 3.2 nm. Intensity for a single sphere of 3 nm (broken line).

It should be note that the minima are smeared out in the scattered intensity and the higher the polydispersity, the less marked the minima.

Moreover, it should be notice that in equation 1.44, the intensity is weighted for the V^2 term, which means that the objects with larger dimension will contribute more to the total measure intensity.

Let us consider, now, an ensemble of particles with a continuous size distribution described by the function $D_N(R)$. The measured intensity is given by the sum over all the contribution from the different size, the probability of which is described by $D_N(R)$:

$$\frac{d\sigma}{d\Omega} = (\Delta\rho)^2 \int_0^\infty D_N(R)V(R)^2P(Q,R)dR \qquad \text{Eq. 1.45}$$

In most of the practical cases the Gaussian distribution is used as "probability function" D_N:

$$D_N(R) = \frac{1}{\sigma\sqrt{2\pi}} exp\left[\frac{(R-\bar{R})}{2\sigma^2}\right] \qquad \text{Eq. 1.46}$$

where $\bar{R}$ is the mean sphere radius value and σ is the standard deviation.

As alternative are also used the Schultz and the Weibull distribution which are reported in equations 1.47 and 1.48 respectively.

$$D_N(R) = \left[\frac{Z+1}{\bar{R}}\right]^{z+1} R^z exp\left[-\left(\frac{z+1}{\bar{R}}R\right)\right]\frac{1}{\Gamma(z+1)} \qquad \text{Eq. 1.47}$$

where z is the parameter related to the width of the distribution and:

$$D_N(R) = \frac{\bar{R}}{\beta}\left(\frac{R}{\bar{R}}\right)^{\beta-1} exp\left(\frac{R}{\bar{R}}\right)^{\beta} \qquad \text{Eq. 1.48}$$

here, β is the parameter related to the distribution.

The Gaussian function is the most used due to its simplicity; the Schultz distribution is able to describe the polydispersity in microemulsion droplets **[2]**, while the Weibull distribution works better for alloy and system with hard-sphere interaction potential **[3-5]**. The advantage of using the

last two distributions is that they can account for asymmetry in the shape of the size-distribution function, which is often the case in real systems.

1.3.4 The Structure Factor

Only in few cases it is possible to calculate an analytical expression for the structure factor *S(Q)*. For a homogeneous and isotropic system of spherical particles, the static structure factor is:

$$S(Q) = 1 + \frac{N}{V}\int e^{iQr}(g(r) - 1)dr = 1 + \frac{4\pi N}{V}\int_0^\infty r^2(g(r) - 1)\frac{\sin(Qr)}{Qr}dr \quad \text{Eq. 1.49}$$

It should be noted that the static structure factor is related to the pair distribution function *G(r)* via Fourier Transform. This equation gives the link between the static structure factor *S(Q)* measured in a scattering experiment and the pair distribution function *G(r)* representing the description of the microstructure of the system.

References

[1] *"Characterization of semiconductor heterostructures and nanostructures 2nd ed."*, **2013**, edited by C. Lamberti and G. Agostini

[2] M. Kotlarchyk, R.B. Stephens and J.S. Huang, *J. Phys. Chem.*, **1988**, 92, 1533-1538

[3] B.P. Gu, G.L. Liedl, K. Mahalingam and T.H. Sanders Jr., *Mat. Sci. Eng.*, **1986**, 78, 71-85

[4] J.S. Pedersen, *J. App., Cryst.*, **1994**, 27, 595-608

[5] J.S. Pedersen, *Phys. Rev.B*, **1993**, 47, 657-665

1.4 Electron Spin Resonance (ESR) Spectroscopy

This chapter is an introduction to the basic theory of *Electron Spin Resonance* (ESR) spectroscopy **[1]**.

During the early part of this century, when scientists began to apply the principles of quantum mechanics to describe atoms or molecules, they found that a molecule or an atom has discrete states, each with a corresponding energy. Spectroscopy is the measurement and interpretation of the energy differences between the atomic or molecular states. With knowledge of these energy differences, you gain insight into the identity, structure and dynamics of the sample under study.

We can measure these energy differences, ΔE, because of an important relationship between ΔE and the absorption of electromagnetic radiation. According to Planck's law, electromagnetic radiation will be absorbed if:

$$\Delta E = h\upsilon \qquad \text{Eq. 1.50}$$

Where h is Planck's constant and υ is the frequency of the radiation

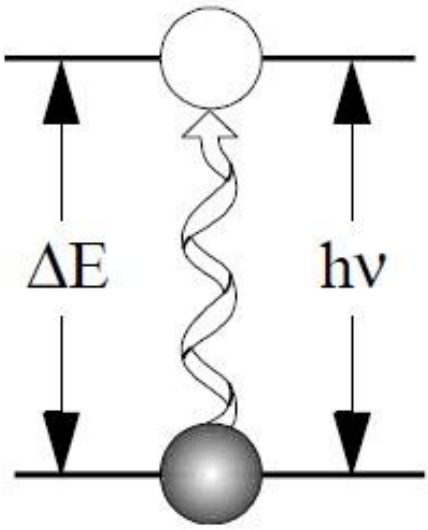

Figure 1.13: Transition associated with the absorption of electromagnetic energy.

The absorption of energy causes a transition from the lower energy state to the higher energy state (see **Fig. 1.13**). In conventional spectroscopy, υ is varied and the frequencies at which absorption occurs correspond to the energy differences of the states. Typically, the frequencies vary from the megahertz range for NMR, trough visible light, to ultraviolet light and X-rays. For an ESR experiment radiation in the gigahertz range is needed.

The energy differences we study in ESR spectroscopy are predominately due to the interaction of unpaired electrons in the sample with a magnetic field produced by a magnet in the laboratory. This effect is called the Zeeman effect. Because the electron has a magnetic moment, it acts like a compass or a bar magnet when it is placed in a magnetic field, B_0. It will have a state of lowest energy when the moment of the electron, μ, is aligned with the magnetic field and a state of highest energy when μ is aligned against the magnetic field (see **Fig. 1.14**).

The two states are labeled by the projection of the electron spin, M_s, on the direction of the magnetic field. Because the electron is a spin ½ particle, the parallel state is designated as M_s = - ½ and the antiparallel state is M_s = + ½.

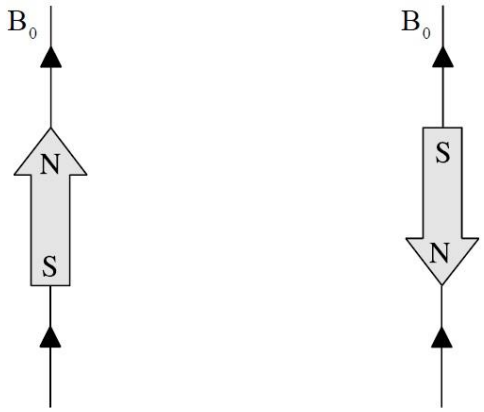

Figure 1.14: Minimum and maximum energy orientations of μ with respect to the magnetic field B_0.

For quantum mechanics, we obtain the most basic equations of ESR:

$$E = g\mu_B B_0 M_S = \pm \frac{1}{2} g\mu_B B_0 \qquad \text{Eq. 1.51}$$

and

$$\Delta E = h\upsilon = g\mu_B B_0 \qquad \text{Eq. 1.52}$$

g is the g-factor, which is a proportionality constant approximately equal to 2 for most sample, but varies depending on the electronic configuration of the radical or ion. μ_B is the Bohr magneton, which is the natural unit of electronic magnetic moment.

Following equations 1.51 and 1.52 it is possible to assert that:

- The two spin states have the same energy in the absence of a magnetic field.
- The energies of the two spin states diverge linearly as the magnetic field increases.

The variation of the spin state energies as a function of the applied magnetic field is shown in **Fig. 1.15**.

Since we can change the energy differences between the two spin states by varying the magnetic field strength, we have two alternative way to obtain spectra. We could apply a constant magnetic

field and scan the frequency of the electromagnetic radiation as in conventional spectroscopy. Alternatively, we could keep the electromagnetic radiation frequency constant and scan the magnetic field (see **Fig. 1.15**).

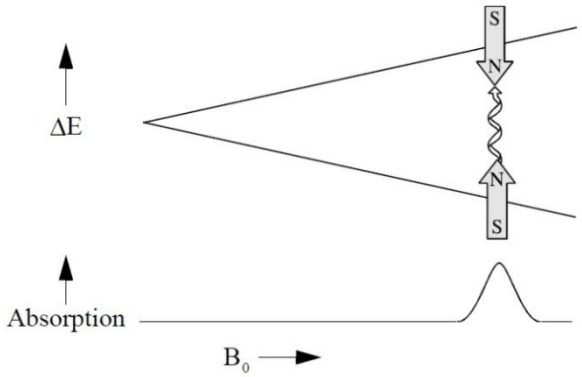

Figure 1.15: Variation of the spin state energies as a function of the applied magnetic field.

A peak in the absorption will occur when the magnetic field "tunes" the two spin states so that their energy difference matches the energy of the radiation. This field is called the "field for resonance". By owing to the limitations of microwave electronics, the latter method offers superior performance.

The "field for resonance" is not a unique fingerprint for identification of a compound because spectra can be acquired at several different frequencies. The g-factor, $g = \frac{h\upsilon}{\mu_B B_0}$, being independent of the microwave frequency, is much better for that purpose. Notice that high values of g occur at low magnetic fields and vice versa.

Measurements of g-factors can give us some useful information; however, it does not tell us much about the molecular structure of our sample. Fortunately, the unpaired electron, which gives us the ESR spectrum, is very sensitive to its local surroundings. The nuclei of the atoms in a molecule or complex often have a magnetic moment, which produces a local magnetic field at the electron. The interaction between the electron and the nuclei is called the hyperfine interaction. It gives us a

wealth of information about the sample such as the identity and the number of atoms which make up a molecule or complex as well as their distances from the unpaired electron.

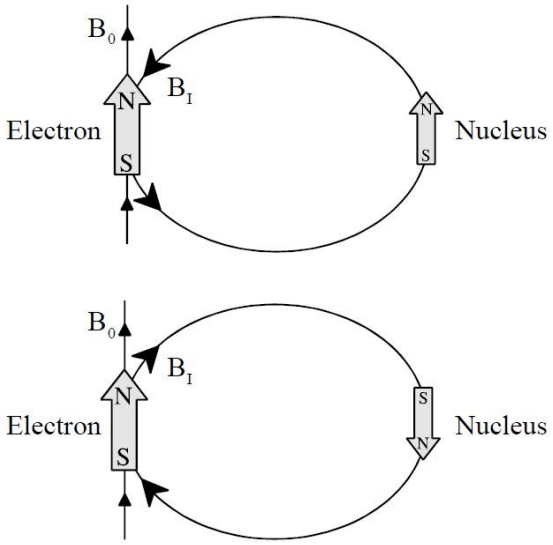

Figure 1.16: Local magnetic field at the electron, B_I, due to a nearby nucleus.

In **Fig. 1.16** the origin of the hyperfine interaction is shown. The magnetic moment of the nucleus acts like a bar magnet and produces a magnetic field at the electron, B_I. This magnetic field opposes or adds to the magnetic field from the laboratory magnet, depending on the alignment of the moment of the nucleus. When B_I adds to the magnetic field, we need a smaller applied magnetic field and therefore the field for resonance is lowered by B_I. The opposite is true when B_I opposes the applied field.

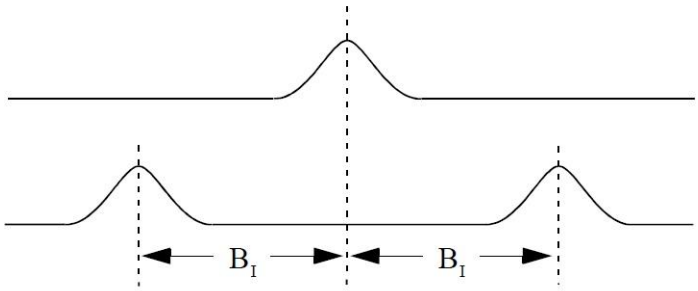

Figure 1.17: Splitting in an ESR signal due to the local magnetic field of a nearby nucleus.

For a spin ½ nucleus such as a hydrogen nucleus, we observe that our single ESR absorption signal splits into two signals which are each B_I away from the original signal (see **Fig. 1.17**).

If there is a second nucleus, each of the signals is further split into a pair, resulting in four signals. For N spin ½ nuclei, we will generally observe 2^N ESR signals. As the number of nuclei gets larger, the number of signals increases exponentially. Sometimes there are so many signals that they overlap and we only observe one broad signal.

So far, we have concerned ourselves with where the ESR signal is, but the size of the signal is also important if we want to measure the concentration of the ESR active species in the sample. In the language of spectroscopy, the size of a signal is defined as the integrated intensity, i.e. the area beneath the absorption curve (see **Fig. 1.18**). The integrated intensity of an ESR signal is proportional to the concentration.

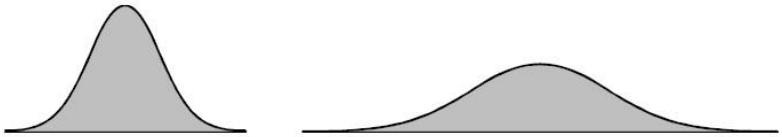

Figure 1.18: Integrated intensity of absorption signals. Both signals have the same intensity.

Signal intensities do not depend solely on concentrations. They also depend on the microwave power. If you do not use too much microwave power, the signal intensity grows as the square root of the power. At higher levels, the signal diminishes as well as broadens with increasing microwave power levels. This effect is called saturation, if you want to measure accurate line-widths, line-shapes, and closely spaced hyperfine splitting, you should avoid saturation by using low microwave power. A quick means of checking for the absence of saturation is to decrease the microwave power and verify that the signal intensity also decrease by the square root of the microwave power **[2]**.

References

[1] J.A. Weil, J.E. Wertz and J.R. Bolton, "*Electron Paramagnetic Resonance: Elementary Theory and Practical Applications*", **1999**, John Wiley & Co, New York

[2] A. Lund, M. Shiotani, S. Shimida, "*Principles and Applications of ESR spectroscopy*", **2011**, Springer, New York

2. BEAMLINES

2.1 ID22

ID22 is the high resolution powder diffraction beamline of the *European Synchrotron Radiation Facility* (ESRF) of Grenoble in France **(1)**. The ID22 diffractometer works in a Debye-Scherrer geometry. The powdered samples are loaded in glass, or kapton capillaries, mounted on the axis of the diffractometer and spun to improve powder randomization. The X-rays are supplied by means of three 11-mm-gap ex-vacuum ondulators of the synchrotron which cover the entire energy range from 5 keV to 60 keV with a λ which can be varied between 2.48 Å and 0.21 Å. The wavelength can be selected using a double-crystal Si monochromator. In particular a Si (111) crystals for the standard operation mode and Si (311) crystals used for application for which an higher energy resolution is needed. The first monochromator crystal is side cooled by copper blocks through which liquid nitrogen flows. The second crystal is cooled by thermally conducting braids that link to the first crystal. The dimension of the beam is regulated by some slits, typically the size is 0.5 – 2.5 mm (horizontal) and 0.1 – 1.5 mm (vertical). Usually a sufficient amount of sample illuminated by a large beam is needed in order to obtain good data. For this reason the monochromatic beam from the source passes unperturbed to

the sample without focusing. The diffractometer, shown in **Fig 2.1(a)**, mounts a bank of nine detectors, each one preceded by a Si(111) analyzer crystal, which covered 16° in 2θ to measure the diffracted intensity as a function of 2θ.

A standard material (generally Si standard NIST 640c) is measured to for different calibrations needed i.e. to settle out accurately the wavelength, the efficiency of the detectors, their position and the zero error. The use of an analyzer crystal eliminate fluorescence radiations; moreover it renders the positions of diffraction peaks immune to aberrations and increases the accuracy and precision for determining the position of powder diffraction peak. Finally, with a perfect setup of the instruments and thanks to the high resolution, to the high statistic and to the good collimation of the beam is possible to obtain diffraction peaks with the right position and with a narrow instrumental contribution to their FWHM (*Full Width Half Maximum*) (see **Fig. 2.1(b)**).

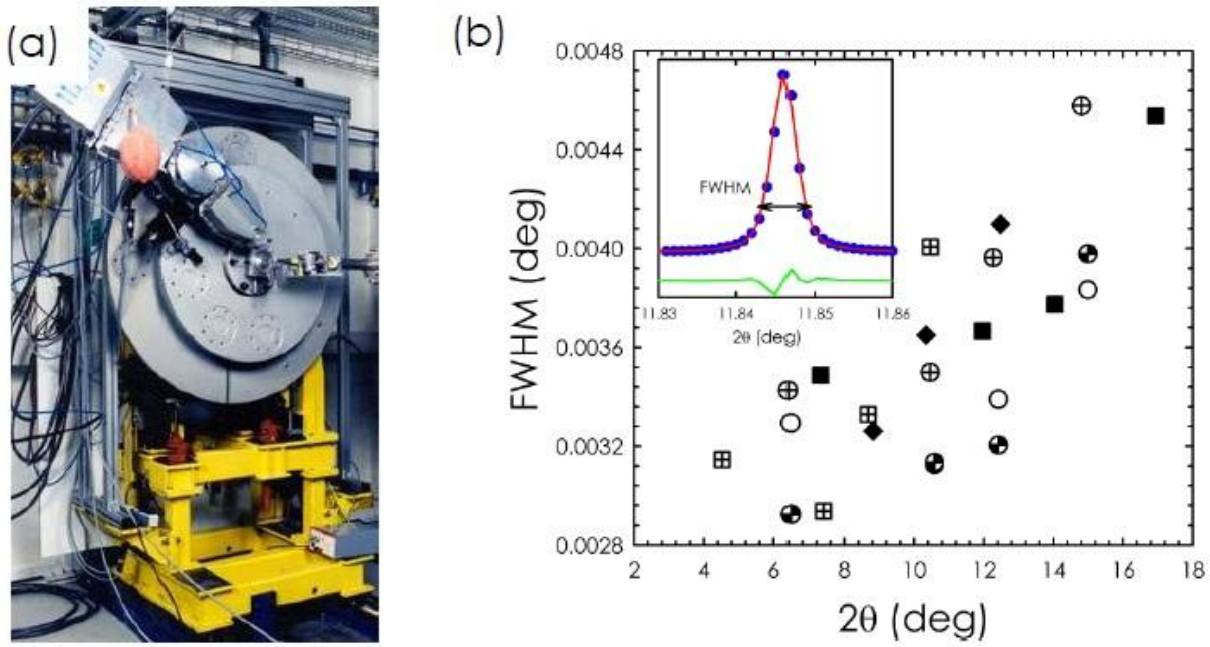

Figure 2.1: (a) Powder diffractometer at ID22. (b) Angular dependence of FWHM related to diffraction peaks of Si standard sample.

This makes ID22 particularly apt to both size and strain and Rietveld analysis: the peak overlap is extremely reduced and it is possible to detect peak splits otherwise impossible to resolve with a lab diffractometer and even most of the synchrotron radiation and neutron powder diffraction beamline. Thus at ID22 it is possible to study both the reciprocal and the real space arrangement of atoms over a wide *r*-range.

References

[1] A.N. Fitch, The high resolution powder diffraction beamline at ESRF, *J. Res. Natl. Inst. Stand. Technol.*, **2004**, 109, 133–142

2.2 ID15

ID15 beamline is composed by two different hutches: ID15A and ID15B **[1]**. The two hutches are dedicated to applications using very high energy x-ray radiation up to several hundred keV. ID15A has two experimental setups: energy dispersive diffraction (EDD) and high energy micro-diffraction (HEMD) setup. ID15B holds the angular dispersive diffraction (ADD) setup using large area detector and high resolution Compton spectrometer. In addition, a high pressure high temperature gas loading system, combining SXRD and MS, is available for gas/solid and liquid/solid catalyzed reactions.

The beamline gives the possibility to exploit the properties of very hard x-rays and for this goal their characteristics are large penetration depth and large Ewald sphere.

The X-ray optics and beamline layout, shown in **Fig. 2.2**, are designed to operate two independent branches simultaneously. ID15A and ID15B share the equipment, and have always been operated more as a single entity than as isolated facilities.

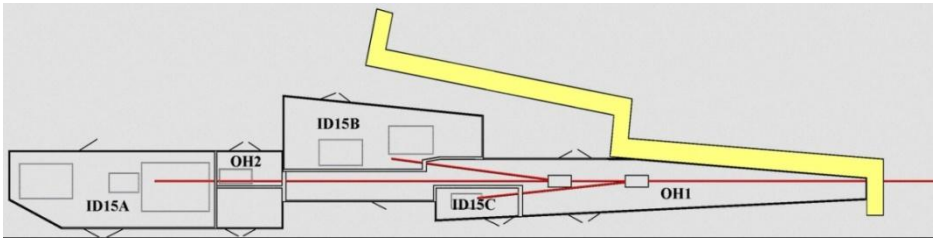

Figure 2.2: Layout of the beamline: ID15A can take white or monochromatic radiation and ID15B takes monochromatic radiation (30, 60 or 90 keV).

The ID15 insertion straight section holds a 7 pole 1.84T asymmetric multipole wiggler (AMPW) and an in-vacuum ondulator (U22). The critical energy of AMPW is 44 keV, and the useful spectrum extends up to 500 keV. Below 120 keV U22 gives a superior flux (see **Fig. 2.3**). The wiggler gives circularly polarized radiation off-axis so that elastic and inelastic magnetic scattering experiments are feasible. The beamline operate usually between 70 and 400 keV, which contrasts sharply with conventional X-ray terminology (home diffractometers), where anything greater than 20 keV is considered exotically high. The X-ray energies below 30 keV are not available at ID15.

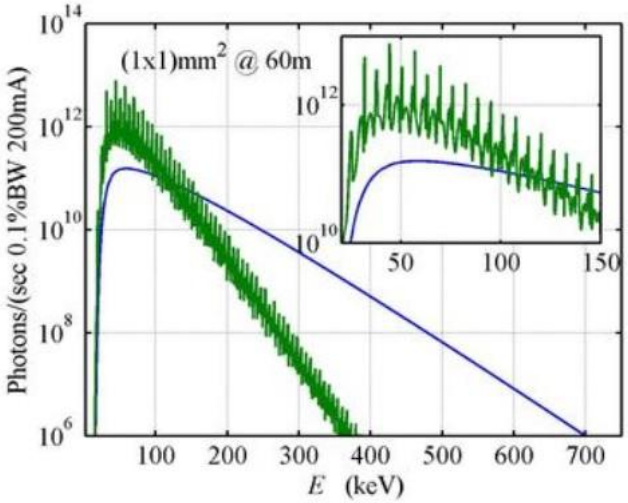

Figure 2.3: The fluxes of the AMPW (blue) and U22 (green) at the orbit through (1x1)mm^2 pinhole at 60 m distance.

In the present thesis, data have been collected at ID15B. This hutch of ID15 was originally a single-purpose beamline dedicated to high resolution inelastic X-ray scattering, but now it is also designed for diffraction experiments. In this beamline there are two different setups as shown in **Fig. 2.4**.

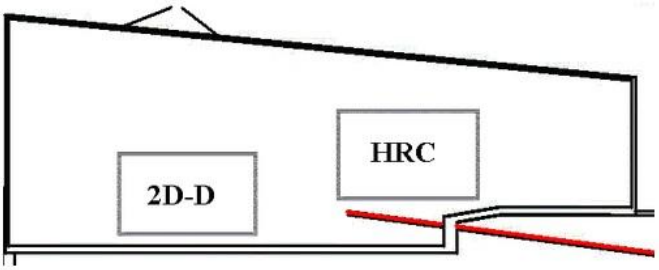

Figure 2.4: The different setups: high resolution Compton setup (HRC) and 2D-diffraction setup (2D-D).

ID15B is a side-station, i.e. it cannot receive the white beam. It receives monochromatic beam from an horizontally focusing monochromator located in Optics Hutch 1, 10 m upstream of the experimental hutch. The scattering angle for the monochromator is almost fixed (10% tunebility) by the beamline geometry. This determines the range of available energies. In-vacuum monochromator tank holds three monochromators providing 30, 60 or 90 keV radiation. The first two are 40cm long bent Bragg crystals and the third one is a bent Laue-crystal.

The two different setups have different purposes and characteristics and the first is the high resolution Compton spectrometer, while the second is the 2D-Diffraction setup.

As for the Compton spectrometer we know that Compton scattered X-rays from a material provide information about the electron momentum distribution. Within the impulse approximation the energy of scattered X-rays is simply determined by the energy of the incident X-rays, the scattering angle and the primary electron momentum. The energy spectrum provides the momentum densities projected on the direction of the momentum transfer.

As mentioned before the ID15B end-station was reconstructed to have place for a diffraction setup. An important and useful characteristic of this setup is the presence of an area detectors by

measuring complete scattering pattern. The 2D-detector and sample towers are on penta-pod optical table (see **Fig. 2.5**).

Figure 2.5: 2D-Diffraction setup on penta-pod table. In this experimental configuration the detector stage holds Mar133 CCD-detector and sample stage holds ETMT-rig. Al-plate before the detector cuts low energy fluorescence background and holds the beam-stop.

The setup can be used on studies of many materials: amorphous, liquids, powders and single crystals. The sample stage is such that several different sample environments can be interchanged depending upon experimental needs. The detector stage, which is translatable along the beam direction in order to cover a range of momentum transfers to match experimental needs, can carry a variety of 2D detectors (MARCCD133, MARCCD165, MARIP345, Pixium, and the image-intensifier).

References

[1] M. Di Michiel, J.M. Merino, D. Fernandez-Carreiras, T. Buslaps, V Honkimaki, P. Falus, T. Martins and O. Svensson, *Rev. Sci. Instrum.*, **2005**, 76, 043702

2.3 BM26

The Dutch-Belgian beamline (DUBBLE) is a beamline of the *European Synchrotron Radiation Facility* (ESRF) in Grenoble **[1]**. DUBBLE has been designed to be used for four experimental techniques: small- and wide-angle X-ray scattering (SAXS/WAXS), interface diffraction (ID), X-ray absorption spectroscopy (XAS) and high-resolution powder diffraction (HRPD).

The ESRF bending magnets start with 6 mrad having a magnetic field of 0.4 T (soft edge, with a critical energy of 9.8 keV) and continue with 0.8 T (hard edge, critical energy 19.6 keV). So, we have two different hutches: one with the soft (S) and the other with hard (H) branch. XAS and HRPD are located in the S-hutch, while SAXS/WAXS and ID occupy the H-hutch.

In the present thesis all the SAXS measurements were performed in the H-hutch, the so called BM26B beamline.

This beamline is specialized in time-resolved small- and wide-angle X-ray scattering and is especially equipped to handle complicated sample environments.

In the H-branch the main optical components are a double-crystal monochromator, followed by a focusing mirror. Instead in the S-branch there are two additional components, a collimating mirror in front of the monochromator. This mirror enhances both the energy resolution for XAS and the angular resolution for HRPD. The focal length of all focusing elements is variable.

The energy spectrum of the ESRF is very hard and thus the rejection of higher-order harmonics is an important issue.

The monochromators use either Si(111) or Si(311) crystals. For the H-branch there are Si and Pt as mirror coatings and an angle of incidence of 2.8 mrad. This configuration leads to a calculated total flux and harmonic fraction as shown in **Fig. 2.6**.

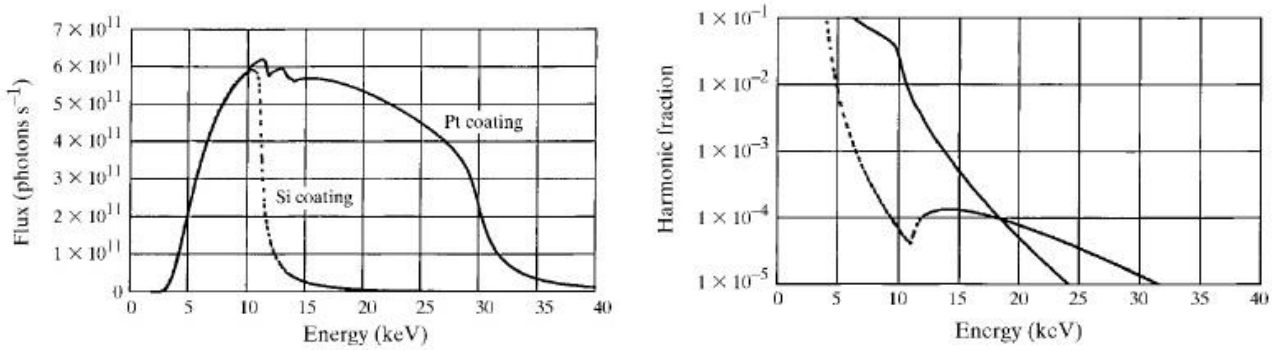

Figure 2.6: Calculated flux (left) and harmonic contents (right) of the H-branch assuming a 100 mA beam current and an Si(111) monochromator. The two choices for the mirror coating are shown.

It is possible to cover two different energy range with different mirrors; with Pt coating the energy range is 11-30 keV, while with Si the usable energy range is 5-11 keV. In addition to the mirrors and monochromators, the beamlines have the usual slits equipped with phosphor screens, filters and beam-position monitors. The two beamlines can operate independently.

The monochromators are based on a commercial platform that delivers an accurate and stable rotating disc inside a vacuum vessel. The water cooling, in this case, is sufficient for the power load from an ESRF bending magnet. The first crystal is placed in the centre of the monochromator. The focusing second crystal and its bender are based on an ESRF design.

The mirrors are made from Si boules and have a surface area of 1200 * 130 mm. The large width is required to have adjacent strips of bare Si and with Pt coating that each accept 2 mrad of radiation. The bender uses transducers to convert the displacements of stepper motors into a constant bending force (ESRF design). The mirror and bender are mounted onto a heavy granite block that decouples the mirror from the vessel. Bellows plus linear translation stages allow a complete alignment of the mirror, including the 60 mm sideways translation to put either the Si or Pt coating into the beam. The mirror tilt angle is read using a commercial sensor **[2]**.

The beam size can be tuned from few millimeters down to about 300 x 300 micrometers in standard configurations. Post-focusing systems are available in order to achieve a smaller beam size. The experimental hutch contains the SAXS camera with a maximal and minimal camera length of 7 and 1.3 m, respectively. This allows simultaneous SAXS/WAXS measurements with a time resolution down to a few msec/frame.

In this thesis only the SAXS/WAXS equipment was employed. The SAXS/WAXS equipment, that is located in the H-hutch, is shown in **Fig. 2.7**.

The SAXS/WAXS station has been designed in such a way that it is possible to mount and interface relatively large equipment. In fact, it is designed with a maximum of flexibility and it is made up of two parts. The first one contains the sample environment and the WAXS detector, while the SAXS detector is mounted on the second part.

The two parts are connected by a vacuum pipe of variable length. Changing of the SAXS camera length is very easy because both parts are mounted using an alignment rail that covers the entire range (1±7 m) of the camera, while the sample position remains fixed. This is useful when complicated sample environments are used. The mounting of the SAXS and WAXS detectors is such that they can be used simultaneously and that they can have an overlapping angular range. On the sample stage additional equipment can be mounted for sample environment control.

Figure 2.7: Beamline BM26 at the European Synchrotron Radiation Facility.

To reduce the parasitic scatter which determines the minimum observable scattering angle (and thus the maximum distance), three slit sets are used with a total separation of 12 m. Due to the large difference in beam divergence and beam size between the horizontal and vertical directions, there is a large difference in the resolution along those directions. Using the full beam, the maximum observable distances are 100 and 1000 Å along the horizontal and vertical directions, respectively. With reduced flux, these values can be improved considerably. As **Fig. 2.6** shows, the SAXS/WAXS equipment can make use of a wide spectral range.

As to the SAXS detector, SAXS images are collected using a Pilatus 1M detector (169mm x 179mm active area). The minimum value attainable with 7m sample-to-detector distance (maximum distance used in our experiment) and a photon wavelength of 1.54 Å is about 0.0175 nm^{-1} (equivalent to a real-space d = 500 nm).

References

[1] M. Borsboom, W. Bras, I. Cerjak, D. Detollenaere, D Glastra van Loon and E. Vlieg, *J. Synchrotron Rad.*, **1998**, 5, 518

[2] G. S. Knapp, H. You and G.R. Holzhausen, *Rev. Sci. Instrum.*, **1995**, 66, 1712

3. IRON OXIDE NANOPARTICLES and NANOCOMPOSITES

3.1 Nanocrystalline Maghemite (γ-Fe_2O_3)

Even before the advent of "nanoscale science" and "nanotechnology" as recognized fields of science and engineering, small particles, colloids, and high-surface-area materials have been critical in applications ranging from catalysis to waste management. The high surface-to-volume ratio in nanomaterials makes them much more reactive toward their surroundings than bulk materials. When particles are so small such perturbed regions are dominant, and the very notions of "phase" and "surface" become murky. These structural complexities also make it difficult to compare the results of theory and experiment. The scientific community has long realized that control of the complexity of surfaces and interfaces at the nanoscale is critical for their function in applications ranging from catalysis of organic reactions in zeolite pores **[1]** to water splitting by transition-metal oxide catalysts **[2]**, to gas sensors **[3]**, and to cancer therapy **[4]**.

In particular, magnetic particles with size in the nanometers scale are now of interest because of their many technological applications and unique magnetic properties which differ considerably from bulk materials. Magnetic ultrafine particles are applied in ferrofluids, refrigeration systems,

etc, and they have potential applications to storage devices, medical imaging and catalysis. The interesting magnetic properties of nanostructured materials are due to finite size effects and high surface/volume ratio **[5, 6]**, thus making the study of the interrelation between microstructure and magnetism very appealing. In this sense, very different magnetic properties have been observed with materials having similar grain sizes but produced by different methods **[6-8]** and, therefore, having different microstructures. As a consequence of that, there is a great variety of data in the literature about the properties of well-characterized γ-Fe_2O_3 nanoparticles.

In particular, because of their promising applications in biomedicine **[9, 10]**, many research activities are currently focused in understanding and improving the magnetic properties of iron oxide nanoparticles. For magnetic materials, it is well known that saturation magnetization values are impacted by the size reduction at the nanometer scale **[11]**. However, different magnetic characteristics are often reported for a same particle size depending on the synthesis procedure used. A few studies have already addressed the correlations between the synthesis parameters and the magnetic properties of iron oxide particles **[12, 13]**, but correlations with their crystal structure and microstructure are still scarce **[14-16]**. Furthermore, it still remain hard to find a process or environment in which iron oxides do not participate. From the surface of Mars to the depths of Earth, from old rusting factories to high-tech magnetic recording devices, from pigeon brains to drug delivery systems, iron oxides are ubiquitous.

In this thesis, the nanocrystalline material γ-Fe_2O_3/PMA (PMA = poly(methylacrylate)) was synthesized by the microwave plasma techniques in collaboration with the Karlsruhe University. For this study the attention is focused on the complete structural characterization by means of the reciprocal and real space analysis of synchrotron radiation XRPD data and via ESR study.

3.1.1 Synthesis

The nanocrystalline powder γ-Fe_2O_3/PMA was synthesized by the microwave plasma techniques by D.V. Szabò and coworkers **[5]**. The precursor chemicals for the core ($Fe(CO)_5$) and the coating (methylacrylic acid (MA), $C_5H_8O_2$) are injected into a constant flow of oxygen and carrier gas (Ar, 20% O_2). The presence of the coating is necessary to prevent an interaction among the clusters. The γ-Fe_2O_3 core is synthesized in a reaction zone heated by a microwave plasma. The apparatus is schematically reported in **Fig. 3.1**. The methylacrylic acid is applied in a second reaction zone and polymerizes on the surface of the ferrite particles.

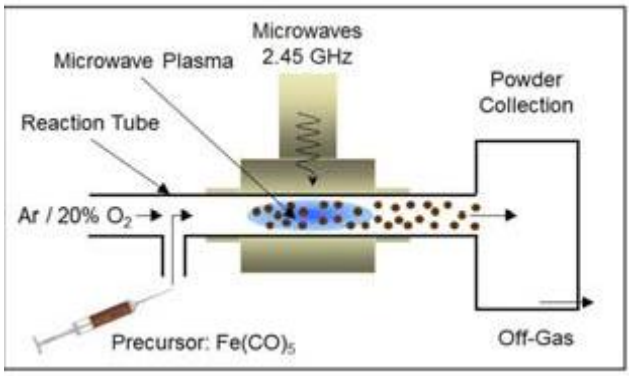

Figure 3.1: Scheme of the apparatus for the microwave plasma.

It should be noted that, for the structural characterizations described below, uncoated maghemite nanoparticles were used, to maximize the γ-Fe_2O_3 volume.

3.1.2 Experimental Section

Five nano-maghemite samples, with size in a range between 2 and 50 nm, were investigated. Two of them were commercial samples (from Aldrich and Iolitec), and, as it will be shown below, their particle dimension were ~50 nm and ~12 nm, respectively. Three maghemite samples labeled C177,

C178 and C179 were synthesized using the microwave plasma techniques described above, and their particle dimensions were of ~2, ~5 nm and ~19 nm, respectively.

As to the structural investigation, XRPD patterns were collected both at ID22 and at ID15 beamline. In addition an ESR study was performed on the maghemite samples in order to investigate their magnetic properties.

Here follows the list of the experiments and of the pertinent experimental conditions related to all the samples investigated in this chapter:

- In the ID22 experiment the samples were investigated at $\lambda = 0.4000$ Å covering a wave-vector Q region up to $Q_{max} \sim 25.7$ Å^{-1}, at Room Temperature. Measurements lasted about 8 hours for each sample, at Room Temperature. Kapton capillaries (1.5 or 2.0 mm diameter) were used.
- In the ID15 experiment the samples were investigated at $\lambda = 0.142$ covering a wave-vector Q region up to $Q_{max} \sim 30$ Å^{-1}, at four different temperatures (T = 120, 180, 240, 295). Measurements lasted about 30 minutes for each temperature. Quartz capillaries (1.5 mm diameter) were mounted on a brass pinhole on the goniometer head of the diffractometer. The latter span during the acquisitions to increase powder randomization.
- In the EPR experiment the magnetic properties of C177, C178, Iolitec and Aldrich samples have been investigated as a function of T in the $120 \leq T \leq 420$ K interval.

As for the diffractometric experiment, data collected at ID22 have been analyzed both in the reciprocal and real space while the ones collected at ID15 only PDF real space analysis has been performed. In fact, to reach a Q_{max} suitable for a PDF a short sample-detector distance was used at the expense of reciprocal space resolution.

As for the diffractometric experiment, it should be noted the huge difference in time for the collection of data in the two beamlines. This difference is due to the presence, at ID15, of an image plate detector (2D camera) placed perpendicular to the incident beam. In this way, the angular resolution can be tuned by acting on the sample to detector distance: by placing the camera far away from the sample, the resolution is increased at the expense of the maximum 2θ, that is Q_{max}, on the other hand, by moving the camera close to the sample, at the expense of the angular resolution, data up to Q_{max} ~30 $Å^{-1}$ can be readily recorded in few seconds acquisition times. Unfortunately in this case, because of the nanometric dimension of the sample particles, the reached Q_{max} is lower than the usual value obtained at these beamlines and the reduction of Q_{max} (down to about Q_{max} ~ 23.5 $Å^{-1}$) was necessary to increase the signal/noise ratio, and then, to study the data at the same conditions.

3.1.3 Structure

An accurate structural and microstructural investigation of the above described γ-Fe_2O_3 samples by means of high resolution X-ray powder diffraction was performed at the ID22 beamline at ESRF with incident wavelength λ = 0.4000(1) Å.

The structure of γ-Fe_2O_3 is closely related to the one of magnetite (Fe_3O_4) which has the inverse spinel structure. The last is displayed in **Fig. 3.2**.

Fe_3O_4 belongs the well known AB_2X_4 spinel structure, that is to the cubic system, space group *Fd*-3*m*. In this structure X forms the cubic close packed structure; A and B ions occupy 1/8 of the tetrahedral interstitial and one half of the octahedral sites respectively.

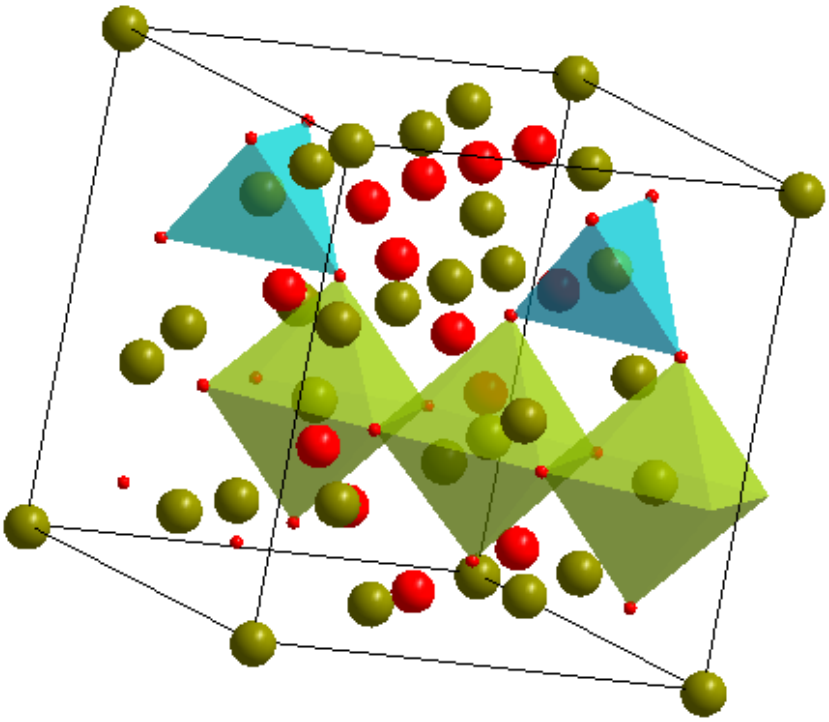

Figure 3.2: Structure of magnetite. Green spheres represent tetrahedral and octahedral iron ions while red spheres represent oxygen ions. The connectivity of tetrahedron and octahedron is highlighted.

In the structure of the iron oxide ions occupy both A and B positions, so that two non equivalent Fe sites are present: in Fe1 site, at 1/8, 1/8, 1/8, iron is in a tetrahedral environment (the A position) while in Fe2 site at ½, ½, ½, it is in a octahedral environment (the B position); oxygen ions occupy only one non equivalent position at *x*, *x*, *x*, with x ~ ¼ (the X position, hereafter the O1 site). We point out that the position in the unit cell for the Fe1, Fe2 and O1 sites described above come from our (non-unique) cell origin choice on the inversion center –3m put, on an octahedral vacancy. Space group *Fd*-3*m* allows an alternative cell origin choice at -43 . In this case Fe1 site is at 0, 0, 0, Fe2 is at 5/8, 5/8, 5/8 and O1 is at *x*, *x*, *x*, with x ~ 3/8. For an exhaustive discussion on spinel structure, see **[17]**.

In the figure above is shown the unit cell of magnetite as well as the coordination polyhedrons of iron ions. Tetrahedron and octahedron are connected by corners, while couples of octahedral are

joined by edges. No contacts among tetrahedron are allowed in spinel structure.

The structure of maghemite is strictly related with the one of magnetite but differs from the latter by the presence of octahedral iron vacancies. In fact, the formula of maghemite can be rewritten as $Fe_8V_{Fe\_oct}O_{12}$, where V_{Fe_oct} is a vacancy of octahedral iron. In respect to magnetite, in maghemite 1/6 of octahedral iron sites are empty. The progressive ordering of iron vacancy causes a symmetry decrease, which can be represented by the following group-subgroup relations:

$$Fd\text{-}3m \rightarrow (F4_132) \rightarrow P4_332 \rightarrow P4_12_12 \; (c'=3a)$$

When vacancies form and (partially) order the structure is primitive cubic, $P4_332$ space group; in this structure octahedral iron ions occupy two non equivalent sites of 12 and 4 multiplicity, the latter is partially empty (occupational factor ≈ 0.333) **[18, 19]**. In the following, we will refer to this phase as "disordered maghemite". XRPD patterns of magnetite and "disordered maghemite" are very close to each other but they differ in cell parameter (a=8.397 Å and a=8.346 respectively) and for the presence of superstructure peaks in the latter due to the different extinction rules of the involved space groups. Four different crystallographic sites exist for oxygen ions **[20, 21]**. Further iron vacancies ordering causes the tripling of the c axis (c~3a,) and a transition to the tetragonal $P4_12_12$ space group **[22]**.

We will refer to this phase as to "ordered maghemite". In ordered maghemite there are three different fully occupied tetrahedral Fe sites and six different fully occupied octahedral Fe sites. An additional octahedral site, which position can be derived following the group subgroup relationships, is empty. Oxygen ions are distributed in twelve different crystallographic sites.

In both maghemite phases connectivity among Fe coordination polyhedron does not change in respect to magnetite. Details on the atomic positions in the two maghemite phases are described in

the references listed above. In respect to “disordered maghemite” in the pattern of the order phase additional superstructure peaks appear.

3.1.4 Reciprocal Space Analysis

The experimental patterns of Aldrich (black curve), C179 (pink curve), Iolitec (red curve), C178 (green curve) and C177(blue curve) samples are shown in **Fig. 3.3**. From the bottom to the top of **Fig. 3.3** a progressive increase of the widths of Bragg reflection is observed suggesting a progressive decrease of the particle size. The size and strain analysis of the pattern will be shown below, using a CeO_2 standard sample to settle on the instrumental line profile broadening parameters.

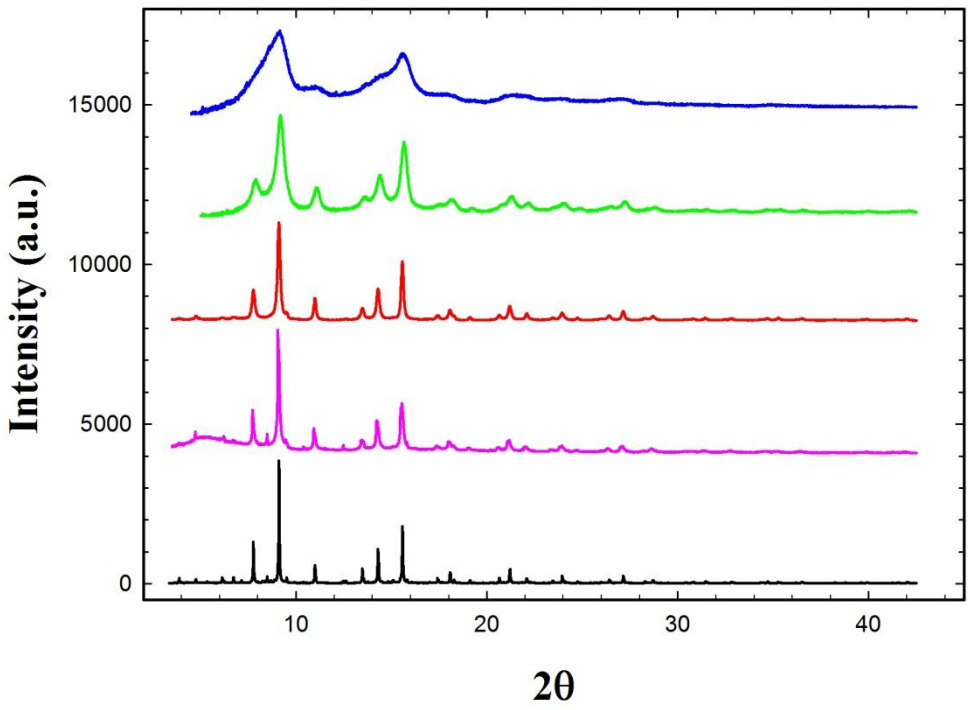

Fig. 3.3: XRPD patterns of Aldrich (black curve), C179 (pink curve), Iolitec (red curve), C178 (green curve) and C177(blue curve) samples.

The average crystallographic structure was determined through Rietveld method varying in the refinement the cell parameter and using wherever it was possible one average mean square displacement (*msd*) for each element: one for cations (Fe) and another one for anions (O).

The ordered maghemite $P4_12_12$ phase is recognizable only in the Aldrich sample, where superstructure peaks typical of this phase are detectable.

For the other samples (Iolitec, C177, C178 and C179), superstructure peaks were not detected. There are two possible reasons: 1) the broadening of the peaks, due to the nanometric size, hides the superstructure peaks or 2) the ordered phase did not occur when the particle size becomes too small.

Fig. 3.4 shows the experimental patterns (black crosses) of Aldrich sample (**Fig. 3.4(a)**), Iolitec sample (**Fig. 3.4(b)**), C179 (**Fig. 3.4(c)**) and C178 (**Fig. 3.4(d)**), and C177 (**Fig. 3.4(e)**) together with their best fits (red curves). The results of the refinements are reported in **Tab. 3.1**

Phase	Parameter	Aldrich	Iolitec	C-179	C-178	C-177
γ-Fe_2O_3 (maghemite)	Space Group	$P4_12_12$	$P4_332$	$P4_332$	$P4_332$	$P4_332$
	a / Å	8.346(1)	8.3531(3)	8.3597(4)	8.3439(11)	8.3464(44)
	c / Å	25.0269(1)	-	-	-	-
	msd (Fe) / $Å^2$	0.00112(14)	0.00778(9)	0.00447(2)	0.00476(4)	0.00141(5)
	msd (O) / $Å^2$	0.00834(44)	0.1501(2)	0.00834(7)	0.00476(4)	0.00141(5)
	Fraction Fe(8c) (tetrahedral)	-	0.9458(1)	0.9093(5)	0.841(4)	0.8766(5)
	Fraction Fe(12d) (octahedral)	-	0.9523(1)	1	1	1
	Fraction Fe(4b) (octahedral)	-	0.586(3)	0.5163(7)	0.653(7)	0.5818(8)
	% Weight	96(0.1)	100	86.6(3)	87.2(1)	80.8(6)
	D_v / nm (W-H)	54.6(5.0)	11.3(1.0)	16.8(1.8)	3.8(1)	2.3(1)
	ε (W-H)	0.0022(5)	0.0084(3)	0.0089(5)	0.0084(6)	0.0095(9)
α-Fe_2O_3 (hematite)	Space Group	*R*-3*cH*	-	*R*-3*cH*	*R*-3*cH*	*R*-3*cH*
	% Weight	4(0.4)	-	3.8(6)	12.8(7)	19.2(9)
Fe_3O_4 (magnetite)	Space Group	-	-	*Fd*-3*m*	-	-
	% Weight	-	-	9.6(5)	-	-
G.o.f.	R (F^2)	0.0448	0.0369	0.0463	0.0734	0.0070

Table 3.1: Rietveld refinement and WH parameters. As to Aldrich sample occupational factors are in line with the structure described in section "**3.1.3 Structure**": one of the octahedral Fe site is empty while the remain sites are fully.

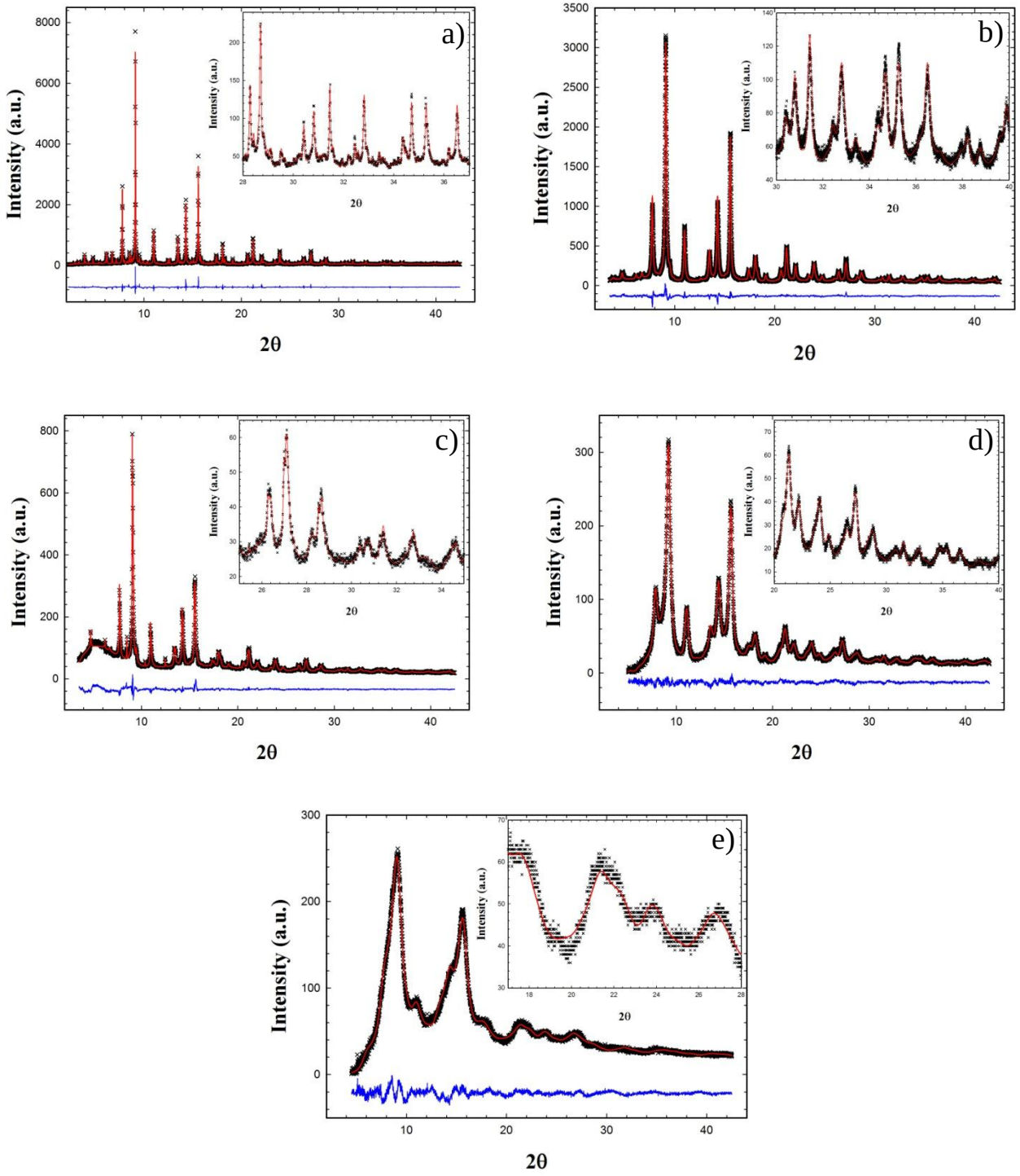

Figure 3.4: Rietveld refinements for Aldrich (a), Iolitec (b), C179 (c), C178 (d) and C177 (e) samples. Experimental pattern (black crosses), fit (red curves) and differential (blue line) are reported. In the insets the high 2θ range is highlighted.

Beside an α-Fe_2O_3 hematite impurity (≈4% weight fraction/WF), the pattern in **Fig. 3.4(a)** can be fitted using the $P4_12_12$ space group; attempts to vary the occupational factors of Fe sites in respect to the "ordered maghemite" phase described above, did not bring to any improvement of the fit.

All the other investigated samples have been fitted using the "disordered maghemite" cubic phase (space group $P4_332$). See Figures **Fig. 3.4(b) - 3.4(e)**.

In **Fig. 3.5** is shown a small angular range of the patterns pertinent to Aldrich (a) and Iolitec (b) samples. The superstructure peaks, related to the iron vacancy ordering and c axis tripling are detected only in the Aldrich sample.

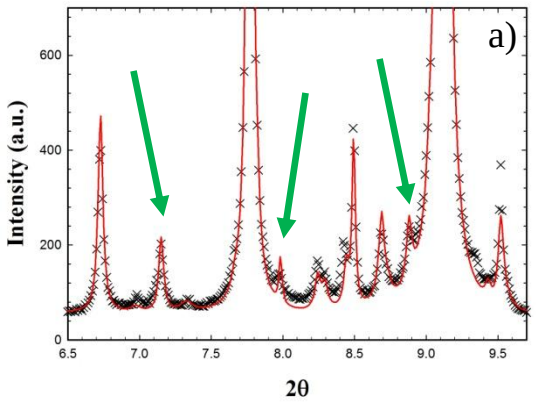

Figure 3.5(a): 2θ range from 6 to 10 of Aldrich sample. The superstructure peak are highlighted by the arrows.

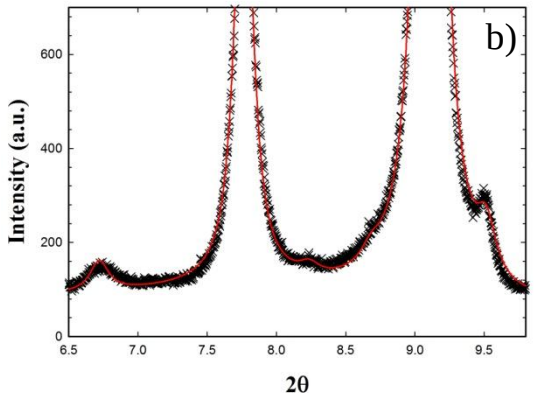

Figure 3.5(b): 2θ range from 6 to 10 of Iolitec sample.

The patterns in **Fig. 3.4(b)**, relative to Iolitec sample, is single phase; in all the synthesized samples, besides the maghemite phase, the presence of hematite is observed: C179 (≈ 4% WF), C178 (≈ 13% WF) and C177 (≈ 19% WF). The C179 sample contains also a magnetite impurity (≈ 10% WF). It should be noted that for the synthesized samples (C177, C178, C179) the amount of hematite increases by decreasing the particle size (see **Tab. 3.2**).

	C179	C178	C177
% of Hematite (*R*-3*cH*)	3.8	12.8	19.2
Particle Size / nm	~19	~5	~2

Table 3.2: Percentage of Hematite as a function of particle size.

During the refinements the occupational factors of iron sites were allowed to vary taking fixed the stoichiometry (Fe_2O_3). In the Iolitec sample a small decrease of both octahedral 12d and tetrahedral 8c sites are observed while the Fe 4b octahedral site increases its occupational factor. In the synthesized samples attempts to vary the occupation of Fe(12d) site do not bring to fit improvement while a noticeable decrease of the tetrahedral Fe(8c) site is apparent. However, we must underline that the excessive broadening of the reflection peaks for the samples with the smallest particle size damps the accuracy of the refinement. As it will be shown in the following section, the PDF analysis of the same data will supply more reliable results.

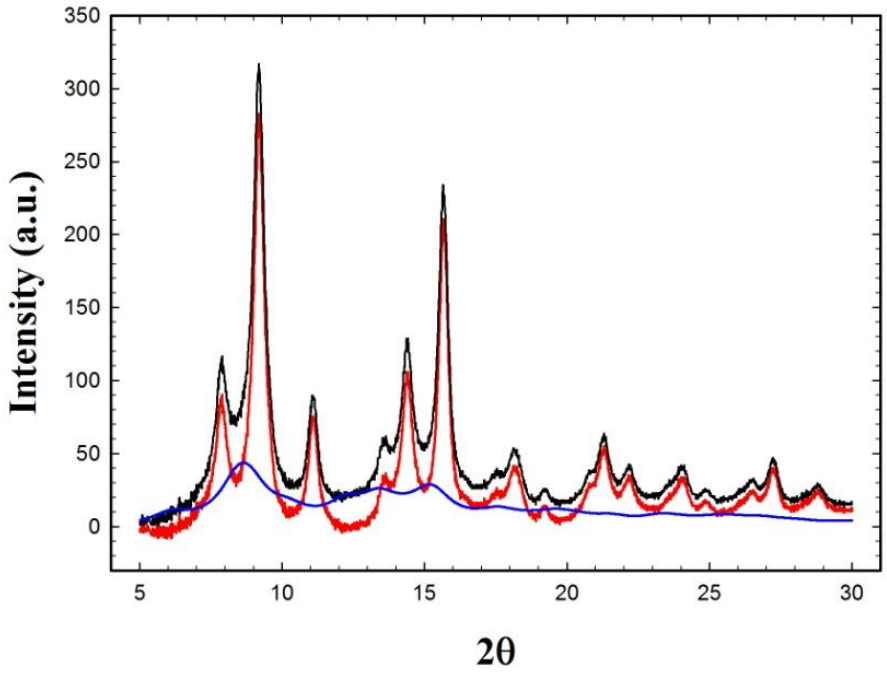

Figure 3.6: C178 pattern: total (black curve), γ-Fe_2O_3, space group $P4_332$(red curve) and hematite, space group *R*-3*cH* (blue curve).

The size and strain analysis of the samples was carried out using the Williamson-Hall method as discussed in section "**1.1.2.3 Williamson-Hall Method**".

Since most of the samples are not single phase, the integral breadth of maghemite peaks was evaluated after subtracting the unwanted peaks of other phases from the experimental pattern.

Let us consider the C178 as an example, shown in **Fig. 3.6**. The W-H analysis was performed on the red curve, that is obtained by subtracting the calculated Hematite phase (blue curve) to the experimental pattern (black curve). The Williamson-Hall results are reported in **Tab. 3.3**.

Sample	Dimension (D_v) /nm	Strain (ε)
Aldrich	54.6(5.0)	0.0022(3)
Iolitec	11.3(1.0)	0.0084(4)
C179	16.8(1.8)	0.0089(3)
C178	3.8(1)	0.0084(6)
C177	2.3(1)	0.0095(7)

Table 3.3: Williamson-Hall results for all samples.

In the **Fig. 3.7** Williamson-Hall plot of C179 is reported as an example.

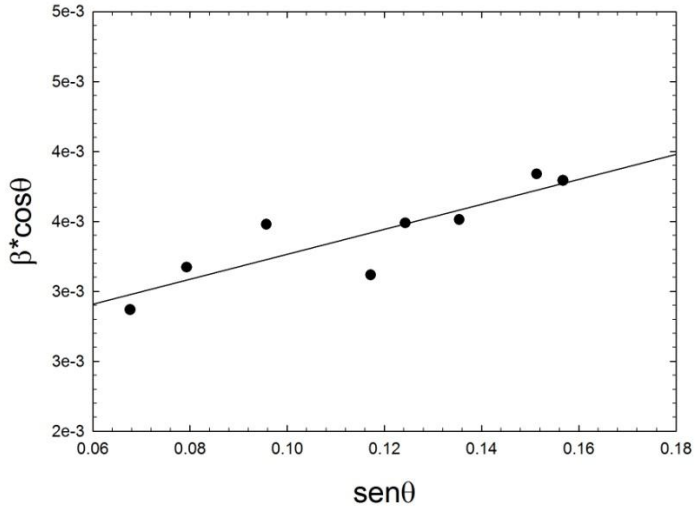

Figure 3.7: Williamson-Hall plot of C179.

3.1.5 Real Space Analysis

As to structural analysis, the Rietveld method could be inaccurate in this case due to the excessive broadness of the diffraction peaks induced by the nanostructure of the samples. For this reason we used the *Pair Distribution Function* (PDF/*G(r)*) analysis, performed at ID22 and ID15 beamlines, to gain insight into the local structure **[23]**. Being a Fourier transform of the total scattering function *S(Q)*, which contains contribution from both Bragg peaks and diffuse scattering, the PDF(*r*) probes also the local atomic arrangements.

As to the ID22 measurements, the *G(r)* functions were processed using the software PDFGetX3 **[24]**. We obtained the experimental *G(r)* curves after background subtraction and multiple and Compton scattering correction. Fits were performed by means of the so called *Real Space Rietveld* analysis using the software PDFgui [**25**].

Fig. 3.8 shows the experimental *G(r)* functions for the five samples considered. The decreasing of the particle size is evident in the damping of the *G(r)* functions, which starts at lower *r* values reducing the particle dimension.

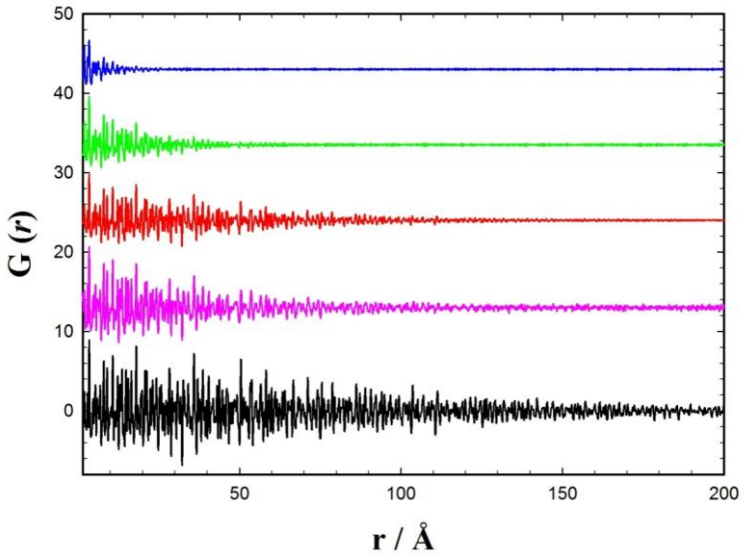

Fig. 3.8: *G(r)* of Aldrich (black curve) , C179 (pink curve), Iolitec (red curve), C178 (green curve) and C177(blue curve) samples.

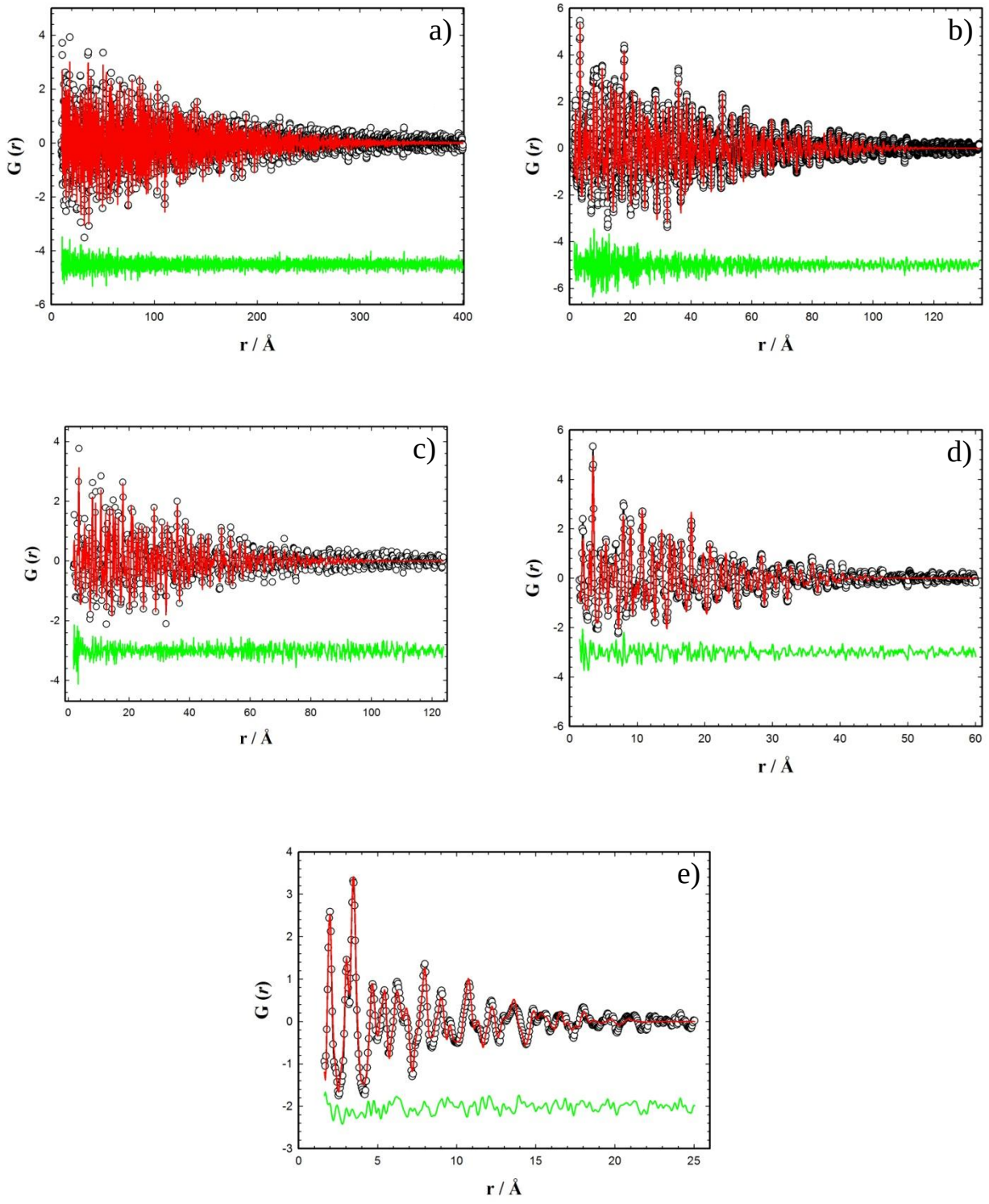

Figure 3.9: PDF refinements for Aldrich (a), Iolitec (b), C179 (c), C178 (d) and C177 (e) samples. Experimental pattern (black symbols), fit (red curves) and differential (green line) are reported.

In **Fig. 3.9** the experimental *G(r)* functions (black symbols) of Aldrich samples (**Fig. 3.9(a)**), Iolitec samples (**Fig. 3.9(b)**), C179 (**Fig. 3.9(c)**), C178 (**Fig. 3.9(d)**) and C177 (**Fig. 3.9(e)**) are shown together with the best fits (red lines) and residuals (green lines). For the fits we used the same structure models (ordered or disordered maghemite, depending on the sample) of the *Reciprocal Space Rietveld* refinement varying the same parameters.

The average crystallite diameters D_V were determined also in the real space, evaluating the damping of *G(r)* oscillations with the interatomic distance *r* **[26]**. It should be noted that also the instrumental peak broadening produce the damping of *G(r)* peaks. It is the case, for instance, of the data collected at ID15 beamline. However, thanks to the high-*Q* resolution of the ID22 beamline, the instrumental effect is negligible and the particle size can be accurately determined.

Tab. 3.4 compares the D_V values obtained with the PDF refinements and the W-H method.

Particle size comparison		
Sample	**D_v / nm**	
	W – H	**PDF**
Aldrich	55(5)	50(4)
Iolitec	11(1)	13(1)
C179	17(2)	12(2)
C178	3.8(1)	5.4(8)
C177	2.3(1)	2.4(3)

Table 3.4: Particle size comparison.

As before stated we used the *Pair Distribution Function* analysis to gain insight into the local structure. To this purpose we used the *G(r)* functions obtained at ID15 at four different temperatures (120, 180, 240 and 295 K). Unfortunately, we cannot compare the C179 sample to the other ones

because of the presence of magnetite in this specimen; the close correlation between magnetite and maghemite structures make difficult to discern the contributions of the two phases in the *G(r)* peaks. In **Fig. 3.10** are shown the experimental *G(r)* functions for Aldrich (a), Iolitec (b), C178 (c) and C177 (d) samples collected at the above listed temperatures. The *G(r)* peaks seem to have scarce dependence on *T*: only small broadening is apparent by increasing temperature.

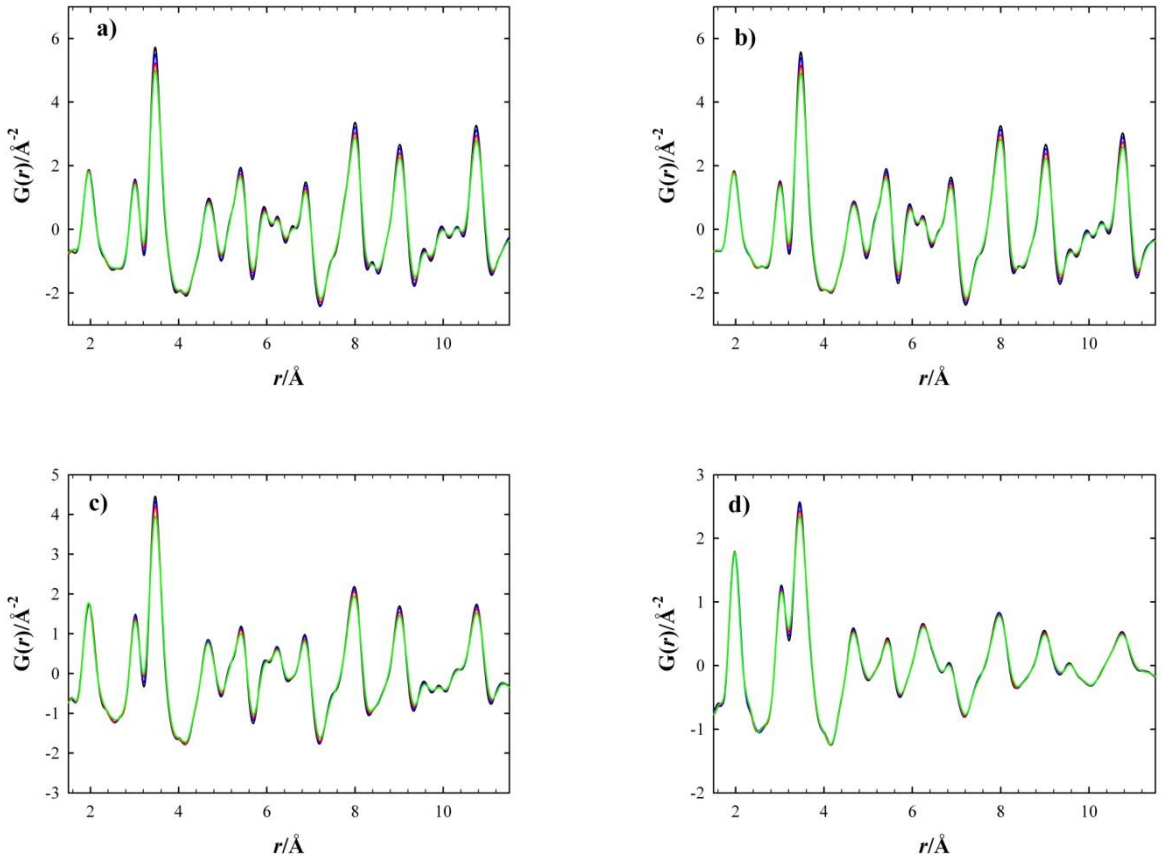

Figure 3.10: *G(r)* functions of Aldrich (a), Iolitec (b), C178 (C) and C177 (d) samples at 120K (black curves), 180 K (blue curves), 240 K (red curves) and 295 K (green curves).

In **Fig. 3.11(a)** is shown the short range *G(r)* functions at 120 K for Aldrich (green curve, $D_V \approx 50$ nm), Iolitec (red curve, $D_V \approx 15$ nm), C178 (blue curve, $D_V \approx 5$ nm) and C177 (black curve, $D_V \approx 2$ nm) samples. The intensity of the peak at ≈ 2 Å, which corresponds to the shortest Fe-O distances,

is almost equal for all the samples. As expected, by increasing the interatomic distances, the amplitude of the *G(r)* peaks decreases more rapidly for samples with the smallest crystallite dimensions. However, this effect is not "monotonic". In **Fig. 3.11(b)** and **3.11(c)** are shown as examples, two small portions of the experimental *G(r)* functions.

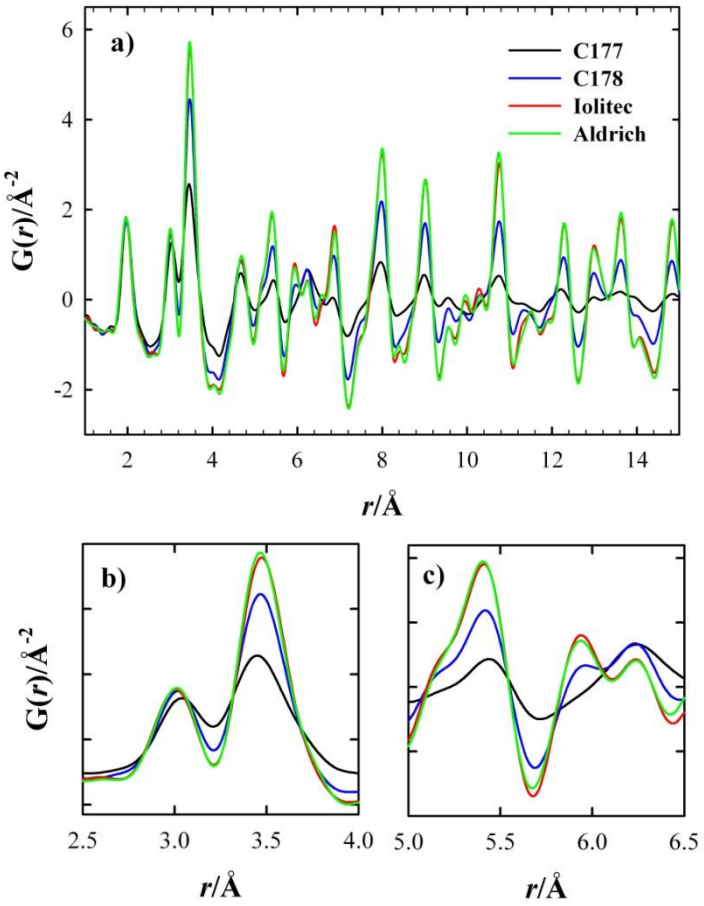

Figure 3.11: *G(r)* functions of Aldrich sample (black curve), Iolitec sample (red curve), the C178 (green curve) and the C177 (blue curve).

The amplitude of the peaks at ≈ 3 Å shown in **Fig. 3.11(b)** does not change much by changing D_V, while the one pertinent to peaks at ≈ 3.5 Å decreases steeply for samples C178 and C177. At the same time, the peaks width seems to increase. In **Fig. 3.11(c)** we can note that the peak amplitude is

proportional to crystallite dimension for peaks at ≈ 5.1, 5.4 and 5.9 Å while the opposite stands at 6.2 Å. Even in this *r* range the peak width seems to increase by decreasing D_V.

To fully understand the findings described above it is useful to break the total *G(r)* function into the so called *partial G(r)s* which are the contribution of the different atomic couples to the total *G(r)*. In particular, in **Fig. 3.12(a)** are shown the calculated partial and total functions for magnetite. Fe1 and Fe2 in the legend are tetrahedral and octahedral iron ions respectively. In **Fig. 3.12(b)** are shown the same functions for disordered maghemite. The latter case is more complex as a consequence of the symmetry decrease which in turn causes the split of octahedral iron site into two non equivalent ones. In the following we will discuss the contribution of tetrahedral (hereafter Fe1) and octahedral (hereafter Fe2) iron ions to the different *G(r)* peaks, which are easily recognizable in **Fig. 3.12(a)**. However, we have to take in mind that this is a simplification in respect to the more complex structure of maghemite described in the right hand side of the same figure.

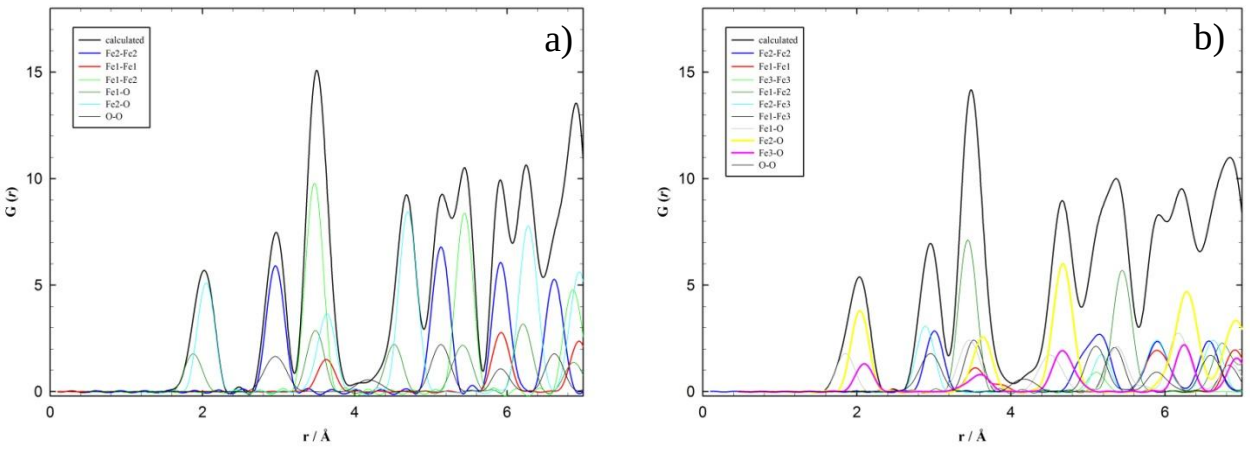

Figure 3.12: Partial PDFs of magnetite phase, space group *Fd*-3*m* (a), and maghemite phase, space group $P4_332$ (b).

Let us focus on the $2.5 \leq r \leq 4.0$ Å of **Fig. 3.11(b)**. The peak at ≈ 3 Å is due to Fe2-Fe2 and O-O contributions, while the one at ≈ 3.5 Å contains also contribution of Fe1 ions.

We performed the so called direct analysis of all the *G(r)* functions shown in **Fig. 3.11** in the $2.5 \leq r \leq 4.0$ Å range, fitting each of the two peaks using a Gaussian function. In **Fig. 3.13** are reported the *Full Width at Half Maximum* (FWHM) for the peaks at ≈ 3.0 Å (left) and ≈ 3.5 Å (right).

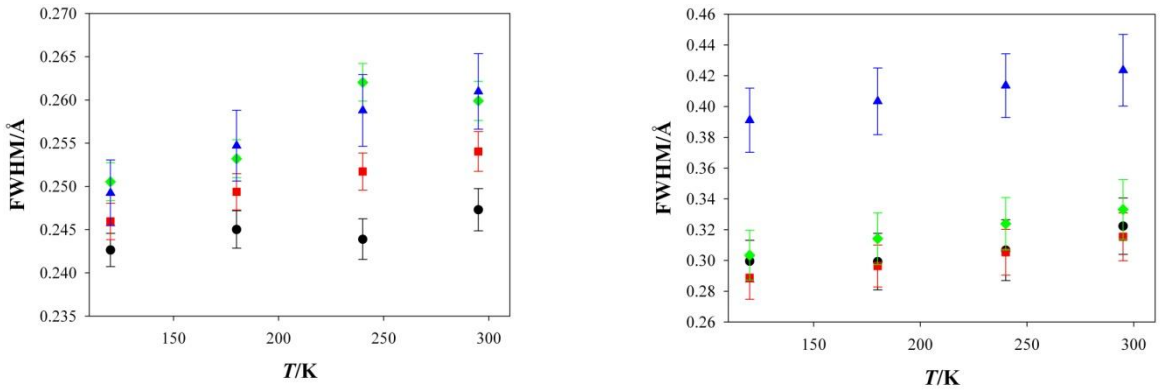

Figure 3.13: FWHM values of the peaks at ≈ 3.0 Å (left) and ≈ 3.5 Å (right) for Aldrich (black circles), Iolitec (red squares), C178 (green diamonds) and C177 (blue triangles) samples.

FWHM values increase smoothly by increasing temperature as a consequence of thermal vibration. This is consistent with the small broadening of *G(r)* peaks above noted. More interestingly, taking fixed *T*, FWHM increases by decreasing D_V (see **Fig. 3.14**, for *T*=120 K).

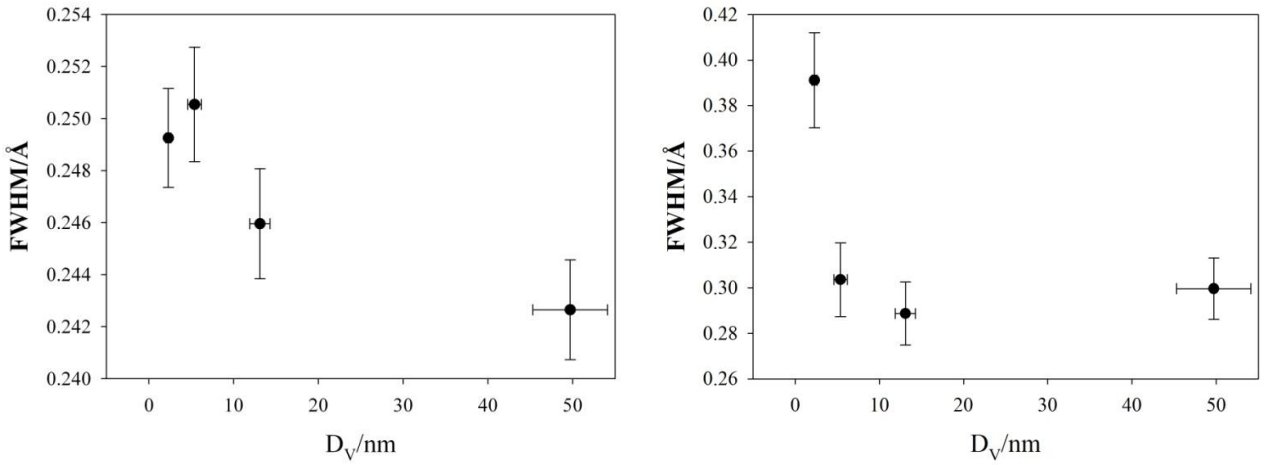

Figure 3.14: FWHM values of the peaks at ≈ 3.0 Å (left) and ≈ 3.5 Å (right) at 120 K as a function of crystallite dimension.

This effect is small for the peak at ≈ 3.0 Å (3-4%) but is about 30% for the one at ≈ 3.5 Å if we compare the Aldrich and C177 samples. Since at fixed *T* the vibrational contribution atomic mean square displacement should be similar for all the samples, this suggests that "static disorder" exist in the smallest nanoparticles, especially when distances involving Fe1 ions are considered. Moreover, the intensity of the peak at ≈ 3.5 Å decreases by decreasing D_V.

The data at 120 K have been analyzed using the so called *Real Space Rietveld* method. Experimental *G(r)* functions have been fitted in the $1.7 \leq r \leq 10$ Å interval against structural model of "disordered maghemite" **[18]**. The results of the fit are shown in **Fig. 3.15(a)** (Aldrich sample), **Fig. 3.15(b)** (Iolitec), **Fig. 3.15(c)** and **Fig. 3.15(d)** (C178) and **Fig. 3.15(e)** and **Fig. 3.15(f)** (C177). The structural model fits well the experimental *G(r)* functions for Aldrich and Iolitec samples while a poorer accord is obtained for C178 and C177 samples.

In a succeeding refinement the occupational factor (o.f.) of tetrahedral and of partially occupied octahedral sites have been varied taking fixed the Fe_2O_3 stoichiometry. While for Aldrich and Iolitec samples the o.f. of tetragonal iron site remained unaffected, the same o.f. decreased to ≈ 0.91 and ≈ 0.82 for C178 and C177 sample respectively, bringing also to an improvement of the fit quality.

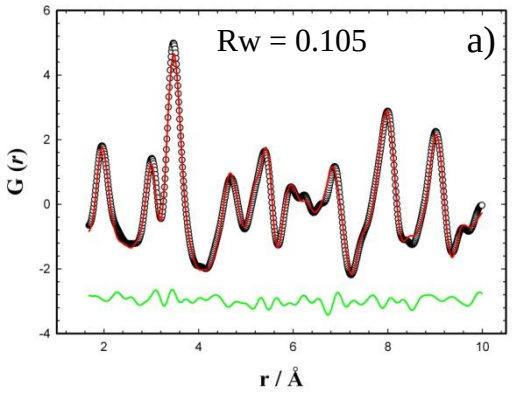

Figure 3.15(a): PDF fit of Aldrich sample using the occupational parameters from **[18]**.

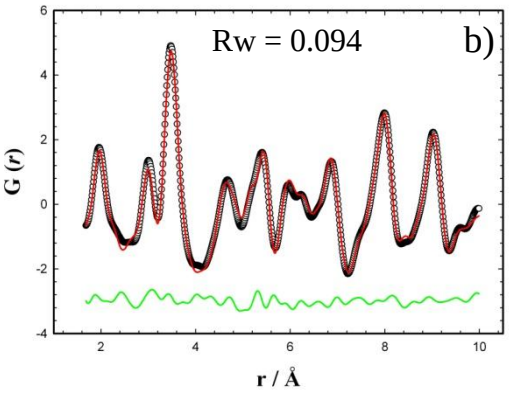

Figure 3.15(b): PDF fit of Iolitec sample using the occupational parameters from **[18]**.

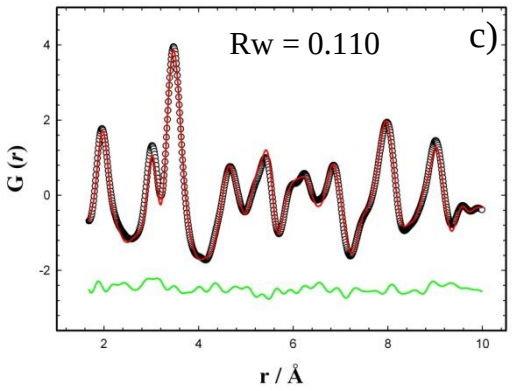

Figure 3.15(c): PDF fit of C178 sample using the occupational parameters from **[18]**.

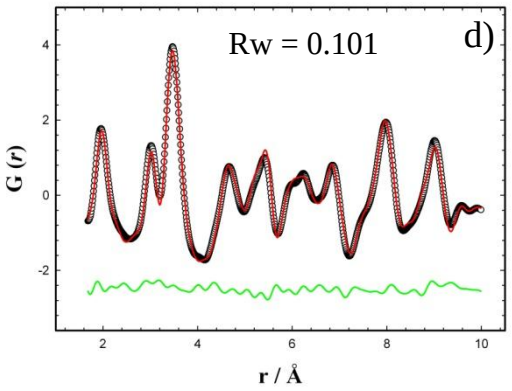

Figure 3.15(d): PDF fit of C178 sample varying the parameters related to the tetrahedral/octahedral Fe occupation.

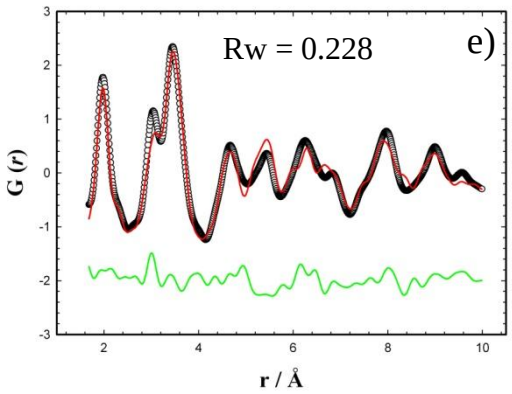

Figure 3.15(e): PDF fit of C177 sample using the occupational parameters from **[18]**.

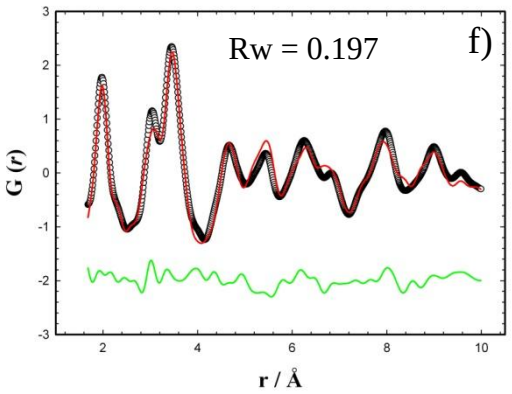

Figure 3.15(f): PDF fit of C177 sample varying the parameters related to the tetrahedral/octahedral Fe occupation.

Fig. 3.15(d) and **Fig. 3.15(f)** report the fits for the two samples. It should be noted that attempts to vary the o.f. of the fully occupied octahedral iron site did not bring to any fit improvement.

Thus, combining the reciprocal space and real space results we can note that the main effect of nano-structuring on the structure of γ-Fe_2O_3 is the progressive disordering of iron vacancies.

In particular, the Aldrich sample (≈50 nm) retains the tetragonal "ordered maghemite" structure; decreasing D_V to ≈12 nm (Iolitec sample) the cubic "disordered maghemite" structure emerges, with

one partially and randomly occupied octahedral iron site; in the C178 (5.4 nm) and C177 (2.4 nm) samples, iron vacancies are shared by both octahedral and tetrahedral iron sites and the o.f. of the latter decreases by decreasing D_V.

3.1.6 ESR Analysis

In the ESR analysis only three sample were investigated: Aldrich, C178 and C177 sample.

The ESR spectra of Aldrich sample was formed of a broad band with a profile changing with temperature (**Fig. 3.16**).

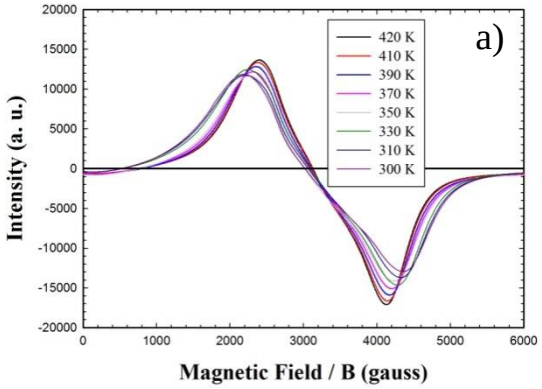

Figure 3.16(a): EPR spectra of Aldrich sample in warming.

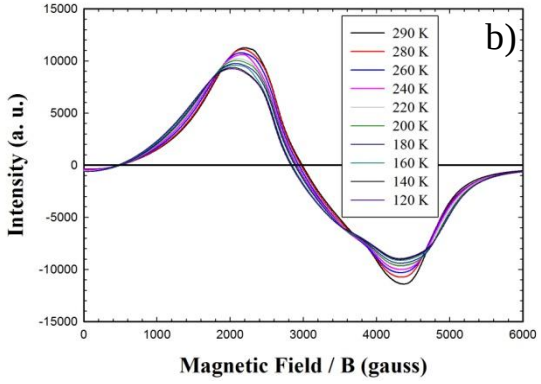

Figure 3.15(b): EPR spectra of Aldrich sample in cooling.

The left part of this pattern was shifting toward lower magnetic field values with decreasing temperature in the range 120 K < T < 300 K. This can be attributed to the fact that at lower temperature the anisotropy field H_a affects more markedly the resonance field profile, while at higher temperature H_a is almost completely cancelled by the thermal fluctuations **[27]**.

Both left and right part of the spectrum were shifting toward the central field at higher temperatures, suggesting that also spin exchange phenomena were becoming active, causing a symmetric narrowing of the spectral profile. However, the whole ESR pattern seems composed of many different contributions, so that a more detailed interpretation seems very difficult with this sample.

A more clear situation was noticed with C178 (**Fig. 3.17**) and C177 (**Fig. 3.18**) superparamagnetic samples. Indeed, their ESR pattern is composed of a single nearly Lorentzian-shaped line broadening with decreasing temperature.

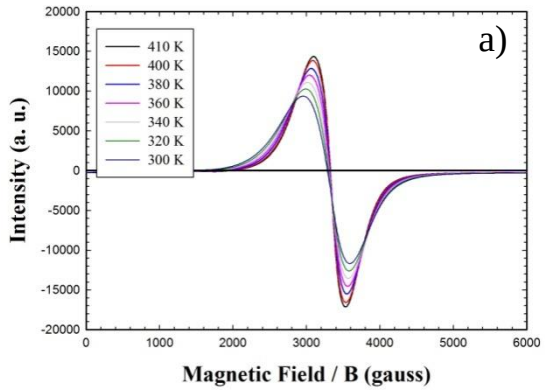

Figure 3.17(a): ESR spectrum of C178 sample in warming.

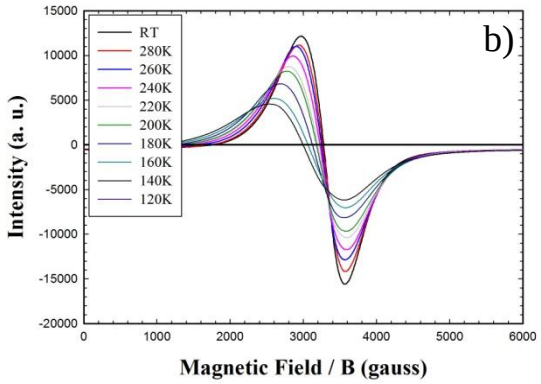

Figure 3.17(b): ESR spectrum of C178 sample in cooling.

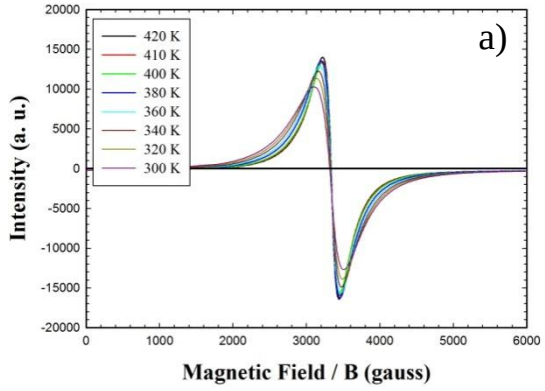

Figure 3.18(a): ESR spectrum of C177 sample in warming.

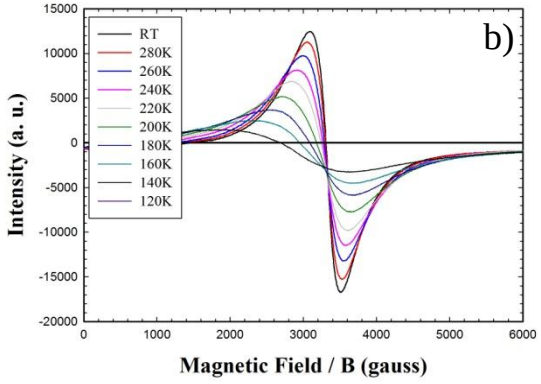

Figure 3.18(b): ESR spectrum of C177 sample in cooling.

Similar situations were reported in **[28]** with superparamagnetic particles with diameters ranging between 16 and 23 nm, i.e. by far larger than those here examined. A model was there proposed assuming that at enough high temperature the anisotropy energy of those samples was much smaller than kT, so that the thermal motion was able to wash out the anisotropic internal field H_a. However, a deeper analysis of the spectra here reported in the **Fig. 3.17** and **3.18** indicates that, with

decreasing temperature, in the low temperature range the line broadening is essentially attributable to a shift toward lower fields of the left part of the spectrum. This effect is more accentuated with the smaller (C177) particles than with the larger (C178) ones. By contrast, at higher temperature both the spectral lobes merge toward the central field with increasing temperature. This suggests that two different phenomena cause the ESR line narrowing with increasing temperature also with these two samples, as already above suggested for the larger Aldrich sample.

Indeed, the shift at low temperature of the left spectral portion can be mainly attributed to the fact that the anisotropy field H_a is not completely washed out and that it becomes increasingly more effective at lower temperature **[27]**, whereas at higher temperature it would be almost completely cancelled by the thermal fluctuations. By contrast, at higher temperature the exchange phenomena would become more active, causing a line narrowing.

By keeping in mind these considerations, we report in **Fig. 3.19** the plot of the ESR line width of these two samples as a function of the detection temperature.

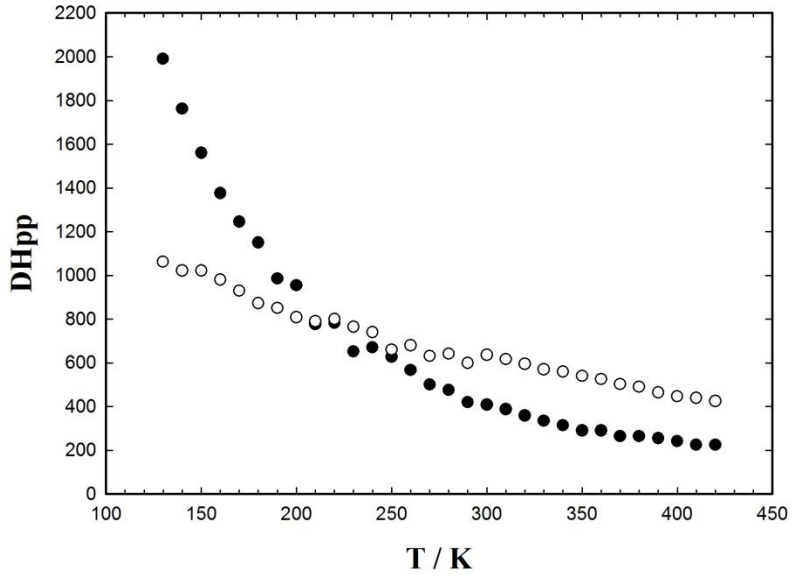

Figure 3.19: Peak to peak line width (DHpp) of C177 (full circles) and C178 (empty circles).

We have tried to apply here the model adopted in **[28]**, by plotting the peak-to-peak ESR line width of these two samples as a function of 1000/T (K^{-1}). However we obtained reliable results for the 5nm particles only, C178 sample. In this case, the best-fitting straight line $\Delta H = \alpha + \beta/T$ was characterized by the parameters α = 0.01828 (Tesla) and β = 12.408 (Tesla K). Conversely, for C177 sample, α = -0.06448 (Tesla) and β = 32.449 (Tesla K).

The following equation has been also proposed in **[28]**:

$$V = \frac{\beta}{\alpha\gamma} \qquad \text{Eq. 3.1}$$

where V is the volume of the particles and

$$\gamma = \frac{M_S * H_0}{2\pi\mu_0 k_B} \qquad \text{Eq. 3.2}$$

with H_0 = spectral central field ≅ 0.33 tesla, $\mu_0 = 4\pi*10^{-7}$ (tesla m s C^{-1}), $k_B = 1.3806488*10^{-23}$(JK^{-1}) and M_S is the saturation magnetization equal to 35 Gg^{-1} detected on the same sample by magnetization measurements **[29]**.

In the case of C178 sample, the calculated nanoparticle diameter on the basis of equations (1) and (2) is very close to the experimental one (≈5 nm) while in the case of C177 a negative meaningless volume of the nanoparticle would be obtained due to the negative value of α. This indicates that the model reported in **[28]** is adequate for the former sample, but no more for the latter. The larger line broadening occurring with the $D_V \approx 2$ nm sample at low temperature indicates the presence of a new contribution to its internal magnetic field, which was negligible with the $D_V \approx 5$ nm sample.

On the other hand, the internal anisotropic magnetic field is given by **[27, 30]**

$$H_a = \frac{2K}{M_S} \qquad \text{Eq. 3.3}$$

where the anisotropy constant K is given by **[31]**

$$K = K_C + \frac{6K_S}{d} \qquad \text{Eq. 3.4}$$

in which K_C is the "core" anisotropy constant and K_S is the "surface" anisotropy constant. The surface contribution has a negligible effect on H_a with large enough particles, as here with those with $D_V \approx 5$ nm, but it can increase the H_a anisotropic field even of a pair of order of magnitude when the particles are very small, as the $D_V \approx 2$ nm particles here investigated **[31]**.

In the latter case, the thermal energy kT becomes inadequate to overcome completely the anisotropy energy so that the ESR line is not Lorentzian-shaped and its first derivative has a broader left lobe, as above reported.

As reported above, the most important structural effect of size reduction is the progressive increase of tetrahedral iron vacancies concentration. At the same time, ESR measurements show that the surface anisotropy constant becomes more and more important.

We suggest that iron tetrahedral vacancies lay mainly on the surface and that the variations in exchange phenomena related to defects formation cause the different magnetic behavior of C177 and C178 samples. Further investigations are necessary to shed light on this subject.

References

[1] S. H. Brown, " *Green Chem.: Green Catal.*", **2009**, 2, 1 –36

[2] F. E. Osterloh, *Chem. Mater.***, 2008**, 20, 35–54

[3] J.H. Lee, *Sens. Actuators B*, **2009**, 140, 319 –336

[4] J. D. Heidel and M. E. Davis, *Pharm. Res.*, **2011**, 28, 187– 199

[5] D. Vollath, D.V. Szabó, R.D. Taylor and J.O.J. Willis, *Mater. Res.*, **1997**, 12, 2175

[6] B. Martinez, A. Roig, X. Obrador, E. Molins and C.J. Monty, *Appl. Phys.*, **1996**, 79, 2580

[7] L. Zang, G.C. Papaefthymiou, and J.Y.J. Ying, *Appl. Phys.*, **1997**, 81, 6892

[8] J.L. Pascal, F. Favier, M.L. Elidrissi Moubtassim, and C. Payen, *Chem. Mater.*, **1999**, 11, 141

[9] Pankhurst et al., *J. Phys. D: Appl. Phys.*, **2009**, 42, 224001

[10] Laurent et al., *Chem. Rev.*, **2008**, 108, 2064

[11] Kachkachi et al., *J. Magn. Magn. Mater.*, **2000**, 221, 158

[12] Morales et al., *Chem. Mater.*, **1999**, 11, 3058

[13] Dutta et al., *Phys. Rev. B*, **2004**, 70, 174428

[14] Morales et al., *J. Phys.: Condens. Matter*, **1997**, 9, 5461

[15] Luigjes et al., *J. Phys. Chem. C*, **2011**, 115, 14598

[16] Levy et al., *Chem. Mater.*, **2011**, 23, 4170

[17] K.E. Sickafus and J.M. Wills, *J. Am. Ceram. Soc.*, **1999**, 82, 3279-3292

[18] A.N. Shmakov, G.N. Kryukova, S.V. Tsybulya, A.L. Chuvilin and L.P. Solovyeva, *J. Appl. Cryst.*, **1995**, 28, 141-145

[19] Z. Somogyvari, E. Svab, G. Meszaros, I. Nedkov and F. Bouree, *Appl. Phys. A*, **2002**, 74, 1077-1079

[20] F. Bosi, U. Halenius and H. Skogby, *Am. Mineral*, **2009**, 94, 181-189

[21] H.S. Shin, *J. Korean Ceram. Soc.*, **1998**, 35, 1113-1119

[22] R. Grau-Crespo, A.Y. Al-Baitai, I. Saadoune and N.H. De Leeuw. *Phys.: Condens. Matter*, **2010**, 22 255401

[23] S.J. Billinge and I. Levin, *Science*, 2007, 316, 561

[24] P. Juhas, T. Davis, C.L. Farrow and S.J.L. Billinge, *J. Appl. Cryst.*, **2013**, 46, 560-566

[25] C.L. Farrow, P. Juhàs, J.W. Liu, D. Bryndin, E.S. Bozin, J. Bloch, T. Proffen and S.J.L. Billinge, *J. Phys.: Condens. Matter*, **2007**, 19, 335219

[26] A.S. Masadeh, E.S. Bozin, C.L. Farrow, G. Paglia, P. Juhas and S.J.L. Billinge, *Phys. Rev. B*, **2007**, 76, 115413

[27] V.N. Nikiforov, Yu.A. Koksharov , S.N. Polyakov, A.P. Malakho, A.V. Volkov, M.A. Moskvina, G.B. Khomutov, V.Yu.Irkhin, *J.Alloys and Compounds*, 2013, 569, 58-61

[28] C. Oliva and L. Forni, *Applied Magnetic Reson.*, **2001**, 20, 531-538

[29] S. Schlabach private communication

[30] M. Fittipaldi, C. Innocenti, P. Ceci, C. Sangregorio, L. Castelli, L. Sorace, and D. Gatteschi, *Phys. Rev. B*, **2011**, 83, 104409

[31] G.C. Papaefthymion, *Nano Today*, **2009**, 4, 438-447

3.2 (MP-NHs) Magneto-Plasmonic Nano-Heterostructures

Nanocrystals (NCs, i.e. below 100 nm) are at the current forefront of nanoscience, serving both as model systems for authenticating the basic laws of nanoscale solids and as key elements for realizing innovative devices, fabricating mesoscopic materials, and achieving outstanding functional properties. NCs exhibit order-of-magnitude enhanced and even unprecedented properties, not otherwise observable for their bulk counterparts, which systematically depend on their composition, size, and shape. Well known examples include general alterations in thermodynamic (e.g., melting point decrease, structural metastability) and catalytic properties due to the dominance of surface states, as well as significant changes in electronic band structure for semiconductors (e.g., alterations in band-gap width and energy level spacing at the band-edge) and noble metals (e.g., the emergence of intense surface plasmon oscillations) due charge carrier confinement. Current research on NCs is now being oriented towards development of "smarter" multifunctional

nanostructures able to perform several tasks simultaneously, on one side, and to exhibit abnormal properties with switchable behavior, on the other side **[1-3]**.

During the last decade, researchers have begun to explore heterostructured nanoparticles by integrating multiple nanoparticle components assembling into a single nanoparticle (NP) (into a single nanosystem) **[4-8]**. Within this class of materials metal oxide magnetic nanoparticles are particularly intriguing as exhibit magneto-optical response and spectra that critically depend on the complex chemical and structural properties. On the other hand metallic nanoparticles can present a weak enhanced magneto-optical response in the UV-Vis due to plasmonic excitations.

For this reason development of a novel concept of advanced nanostructured material is based on a proper combination of magneto-optically active and plasmonic inorganic components tailored at the nanoscale. This approach will deliver a new class of multifunctional magneto-plasmonic nano-heterostructures (MP-NHs) whose the properties can be controlled in more than one way, an opportunity prohibited to conventional single-component nanomaterials. Double-components system received much attention because of the improve properties in respect to single constituents **[8-10]**. In fact, traditional "nanocomposite" systems obtained by combining two or more different nanoparticles via bridging molecules or embedding organic/inorganic matrices often suffer from poor stability, degradation of the native responses of the components, and irreproducible performances. For this reason an alternative approach to smart nanomaterials concerns creation of multi-component NC-based heterostructures, in which two or more domains of different inorganic materials are permanently interconnected through direct epitaxial interfaces in controlled three-dimensional spatial arrangements. In particular many efforts have been spent in the design of magneto-plasmonic nano-heterostructure, made of plasmonic metals and magnetic materials, because they have unique properties which are expected to arise from interactions between the electromagnetic field associated with the plasmon resonance of the noble metal component and the

spontaneous magnetic polarization of the magnetic component involved. None of such unusual effects could be otherwise accessed with any of the single components alone or their physical mixture counterparts **[10,11]**. In nanostructures made of noble metals, especially Au and Ag, intense localized surface plasmon resonance leads to peculiar optical properties such as size-, shape-, and medium- dependent enhanced light absorption. Moreover, their magneto-optical (MO) properties seem to depend on size, shape and connectivity of the nano-heterostructures (NHs). Magnetic transition metals, such as Fe, Ni, and Co, also exhibit plasmonic as well as magneto-optical effects, but in such materials the plasmon resonance is damped due to their large optical absorption coefficients and its influence on the MO phenomena are typically negligible. Suitable combinations of transition metals or transition metal compounds and noble metals can be expected to enhance the MO effects due to the strong electro-magnetic field localization that arises from the surface plasmon excitation in the noble metal. Development of magneto-plasmonic nano-heterostructures (MP-NHs) in which plasmonic metals and magnetic materials are epitaxially coupled has been to date restricted to a small selection of material combinations and topologies. For this reason the systems reported in this thesis are composed by iron oxides (magnetite, Fe_3O_4), whose magnetic properties are well known, for the magnetic part and Au, which shows surface plasmon phenomena and optical activity, for the plasmonic counterpart **[12]**. Examples include mainly core@shell systems of Au@Fe_3O_4 **[7,13-15]** and fewer prototypes of heterodimers made of Au-Fe_3O_4 **[13,14]**, in which nearly spherical material sections share small interfacial junctions. The interplay of magneto-optical and plasmonic activities is ultimately expected to pave the way to novel applications in several fields, and in particular, the coexistence of Au and Fe_3O_4 nanoparticles allows simultaneous use of MP-NHs for optical imaging, MRI, biomedical applications, potential contrast agents, high density magnetic recording, controlled drug delivery, biological targeting or separation, catalysis and others **[5,16,17]**.

Despite the intense experimental effort to produce nanocomposites with tailored physical properties, surprisingly, there are few works with an extended structural characterization of this system which allows to observe structural deviations in these nano-heterostructures in respect to single components and bulk materials. In most research papers on these systems only diffraction data from home diffractometers are supplied which often don't hallow to discern even the correct iron oxide phase without ambiguity, because of the close relationships between the structure of magnetite (Fe_3O_4) and maghemite (γ-Fe_2O_3) phases **[18]**.

We have started a complete structural characterization of MP-NHs, because, in our opinion, it is fundamental to interpret correctly the physical properties of these nanocomposites, in particular the differences in respect to the separated bulk/nano-phase **[19].** To reach this goal, high resolution synchrotron radiation X-Ray Powder Diffraction (SR-XRPD), Small Angle X-Ray Scattering (SAXS). Electron Spin Resonance (ESR) spectroscopy has supplied important complementary information.

In this thesis we will present two different investigations:

i) the microstructure of nanocomposites during Fe_3O_4 shell/dimer formation has been studied by means of SAXS measurement and ESR spectroscopy

ii) the structure of core@shell (hereafter CS) and heterodimer (hereafter HD) Fe_3O_4-Au MP-NHs as well as of the Au seeds used to produce them has been investigated by means of XRPD. Data were analyzed both in the reciprocal space and real space exploiting both the Rietveld and Pair Distribution Function (PDF) methods which supply complementary information on the structure and microstructure of these materials.

3.2.1 Synthesis

The synthetic strategy provides a scheme of "growth for insemination" two-stage, which consists in heating a mixture of a solvent (octadecene), appropriate surfactants (oleyl amine, oleic acid), calibrated amounts of $Fe(CO)_5$, and preformed nanocrystals of Au (synthesized by reduction of $HAuCl_4$ in oleyl amine at 100-150 °C) with the function of seeds of nucleation. The technique realizes the selective deposition of Fe_xO_y on Au seeds following the pyrolysis of complexes based oleate iron, which are generated by heating the above mixture at temperatures of 270-320 °C **[13]**.

3.2.2 Experimental Section

All XRPD patterns were recorded at the ID22 and BM26B beamlines of the ESRF as reported below. The ID22 measurements were collected to obtain Rietveld and PDF data and they are performed both at room temperature. The SAXS experiment, instead, was performed at the BM26B beamline to study size and shape of the particles and to understand the mechanism of formation of the nano hetero-structures.

We recall here that a PDF data collection at ID22 is performed by summing different scans, recording for much longer times the intensity at high angle to increase statistic significance. Conversely, to get reliable data for Rietveld analysis one scan is usually enough. A PDF data collection thus involves also the recording of high quality data for reciprocal space analysis. During each experiment, the empty capillary and the contribution of the air in the empty set up were measured in the same *Q* range in order to properly subtract the background for PDF analysis.

Here follows the list of the experimental conditions related to all the samples investigated in this chapter.

The Q_{max} reported below correspond to the highest 2θ value recorded. The actual Q_{max} employed for processing PDF was reduced to Q_{max} = 25 Å^{-1} to increase the signal to noise ratio.

- In the diffraction experiment (Rietveld and PDF) the samples were investigated at λ = 0.3542 Å in the angular range 0< 2θ <110°, covering a wave-vector Q region up to Q_{max} ~ 29.4 Å^{-1}, at Room Temperature. Measurements lasted about 8 hours for each sample. Kapton capillaries (0.7 mm diameter) were used.
- In the SAXS experiment the samples were analyzed with two different setups to investigate two different parts of the pattern. All the measurements were performed at room temperature and they lasted few minutes for every pattern. Glass capillaries (2.0 mm diameters) were used.
- In the ESR experiment the magnetic properties have been investigated. The measurements were performed on the samples as a function of time and temperature.

In the first experiment we measured three samples: a core@shell sample (hereafter CS), where the core is the noble metal Gold and the shell, the magnetic counterpart, is iron oxide in magnetite phase (Fe_3O_4); an heterodimer sample (hereafter HD), where gold and magnetite are shared in a small interfacial junctions; and a nanometric gold sample, the same gold used in the hetero system core@shell and heterodimer.

As to the BM26B measurements two series of samples were prepared starting from the same synthesis route described before, used for the previous samples, but, in this case, some aliquots have been extracted at different time during the synthesis and quenched to room temperature to stop the reaction.

The aliquots are listed in **Tab. 3.5** together with the sample taking times and temperatures. The same series of samples were studied by means of ESR.

N° Aliquot	Time	Temp.	Structure
Aliquot 0	0	120°C	Seeds
Aliquot 1	2’	150°C	Seeds
Aliquot 2	4’14’’	190°C	Seeds
Aliquot 3	n. a.	240°C	Seeds
Aliquot 4	7’	280°C	Seeds
Aliquot 5	9’40’’	293°C	Seeds
Aliquot 6	13’	300°C	Seeds
Aliquot 7	17’	300°C	Seeds
Aliquot 8	25’	300°C	Seeds
Aliquot 9	30’	300°C	HD
Aliquot 10	35’	300°C	HD
Aliquot 11	40’	300°C	HD
Aliquot 12	45’	300°C	HD
Aliquot 13	54’	300°C	HD

N° Aliquot	Time	Temp.	Structure
Aliquot 0	0	120°C	Seeds
Aliquot 1	n. a.	150°C	Seeds
Aliquot 2	3’13’’	180°C	Seeds
Aliquot 3	4’20’’	200°C	Seeds
Aliquot 4	n. a.	240°C	Seeds
Aliquot 5	5’13’’	260°C	Seeds
Aliquot 6	6’15’’	280°C	Seeds
Aliquot 7	7’16’’	300°C	Seeds
Aliquot 8	10’25’’	300°C	Seeds
Aliquot 9	17’26’’	300°C	CS
Aliquot 10	25’40’’	300°C	CS
Aliquot 11	33’30’’	300°C	CS
Aliquot 12	49’40’	300°C	CS

Table 3.5: Synthesis steps for series 1 (on the left) and Series 2 (on the right).

3.2.3 Study of Nanoparticles Synthesis

3.2.3.1 SAXS Experiment

As reported above, aliquots of reaction suspension have been extracted at different times during the synthesis and quenched to room temperature to stop the reaction. Sample taking times and pertinent temperatures for all the aliquots are listed in **Tab. 3.5**.

Fig. 3.20 shows TEM images performed on selected samples. We chose an aliquot before and an aliquot after the heterostructure formation, as examples. In **Fig. 3.20** only two TEM images per series is shown: aliquots 2 and 13 (**Fig. 3.20(a)** and **(c)**) and aliquots 1 and 10 (**Fig. 3.20(b)** and **(d)**)

for HD and CS series, respectively. As shown by TEM images we can define series 1 and series 2 as formed by heterodimer (hereafter HD series) and core@shell (hereafter CS series) structure, respectively.

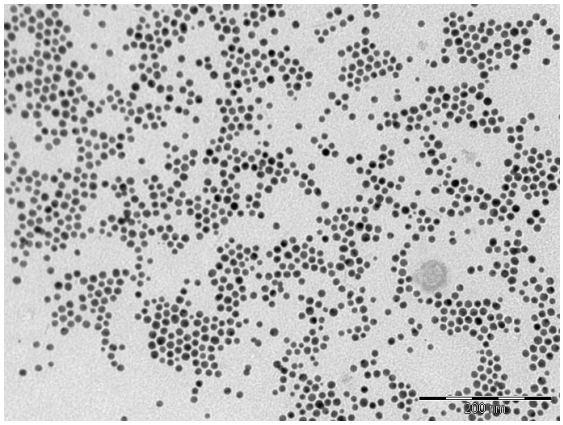

Figure 3.20(a): TEM image of aliquot 2 (gold seeds) of HD series.

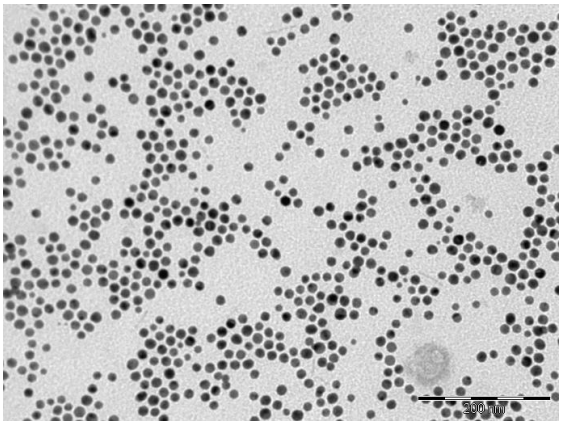

Figure 3.20(b): TEM image of aliquot 1 (gold seeds) of CS series.

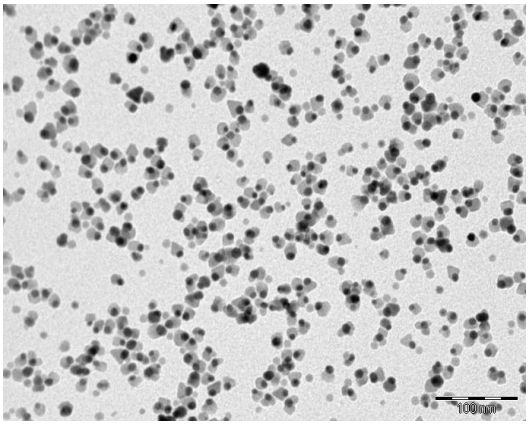

Figure 3.20(c): TEM image of aliquot 13 (HD) of HD series.

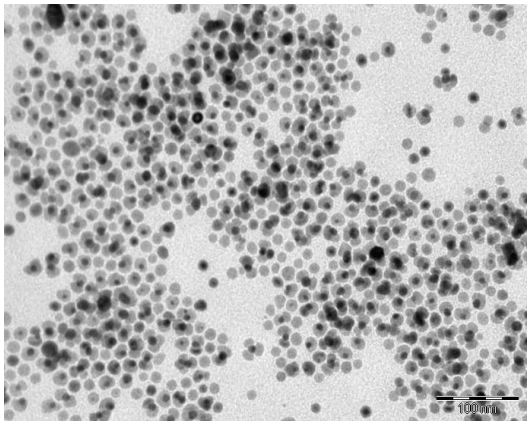

Figure 3.20(d): TEM image of aliquot 10 (CS) of CS series.

Being our SAXS experiment performed on different steps of the synthesis, it is possible to observe the evolution of the samples, during the reaction, from single gold seed to heterostructures plotting $I*Q^2$ as a function of Q.

In **Fig. 3.21** aliquot 13 in HD series is reported, as an example, to show the different parts of the patterns related to the different features of the samples.

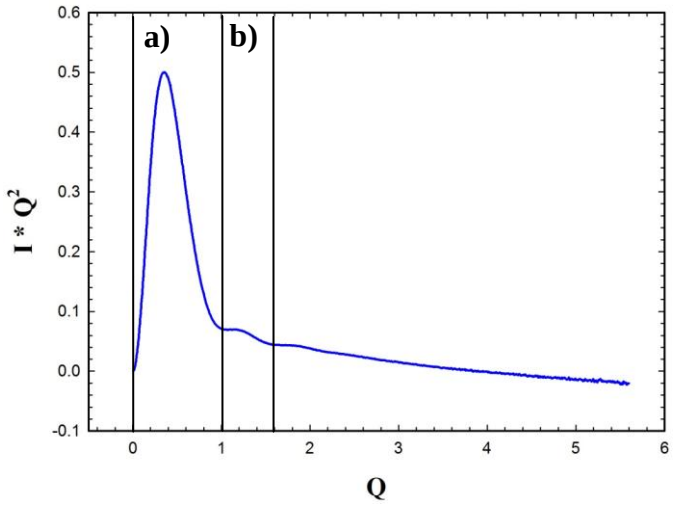

Figure 3.21: plot I* Q^2 Vs. Q.

The position of the most intense peak at $Q \approx 0.5$ (a) zone in **Fig. 3.21**) gives us an evaluation of the particle size (the bigger is the Q value the smaller is the particle size) and of particle size trend versus time; the presence and the higher angle intensity oscillations at $Q \approx 1.2$ (b) zone in **Fig. 3.21**) is an indication of heterostructure formation.

In **Fig. 3.22**, the aliquots with the presence of heterostructures in HD series (**Fig. 3.22(a)**) and CS series (**Fig. 3.22(b)**) are reported.

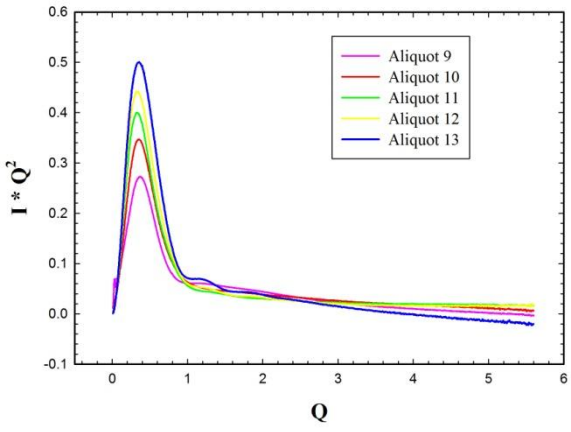

Figure 3.22(a): Evolution of HD series. Data were scaled to show the synthesis in progressive order.

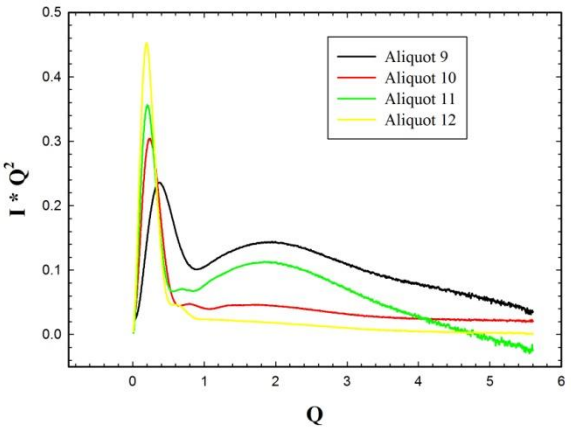

Figure 3.22(b): Evolution of CS series. Data were scaled to show the synthesis in progressive order.

In **Fig. 3.22(a)** the increase of the particle size from aliquot 9 to 11 is evident, while there is a little decrease in the last two steps. Conversely, in **Fig. 3.22(b)** from aliquot 9 to 12 we have a progressive increase of particle dimension according to the previous analysis (see above). As for the heterostructure formation the presence of satellite peaks is clear in the aliquot 13 in HD series and in aliquot 10, 11 and 12 in CS series, suggesting how the complete formation of nanocomposites involves only the last steps of the synthesis and it is more evident in core@shell samples.

The different behavior detected above should be strictly related to the different sample typologies. In the heterodimer case, by increasing time, the form of the particle does not change, while the number of constituted heterodimer increases. Conversely in the core@shell series, there is an increase of the Fe_3O_4 shell dimension with time up to the complete formation of the nanocomposite.

Fig. 3.23 shows some particulars of TEM images of aliquots 10 of CS series where some core@shell heterostructures present an incomplete shell.

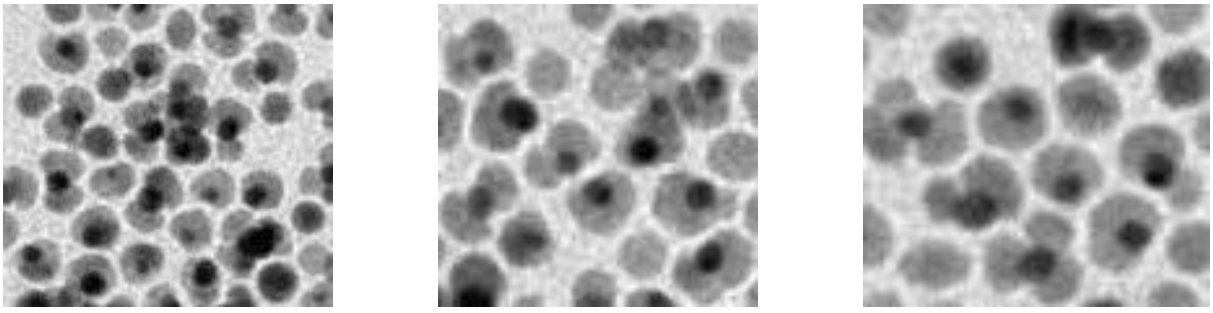

Figure 3.23: Incomplete Fe3O4 shell formation in the aliquot 10 in CS series.

For each series we selected three aliquots, one for gold seeds and two for heterostructures to perform SAXS analysis.

We selected in HD series (**Fig. 3.24(a)**) aliquots 2, 11 and 13, while in HD series (**Fig. 3.24(b)**) we selected aliquots 1, 10 and 12.

The pertinent SAXS patterns are shown in **Fig. 3.24**.

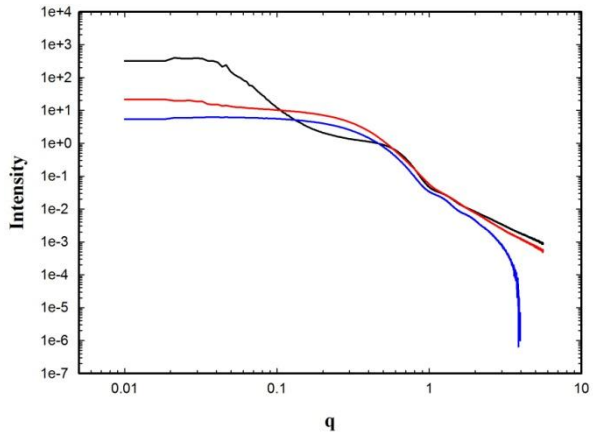

Figure 3.24(a): SAXS patterns for HD series: aliquot 2 (black curve), aliquot 11 (red curve) and aliquot 13 (blue curve).

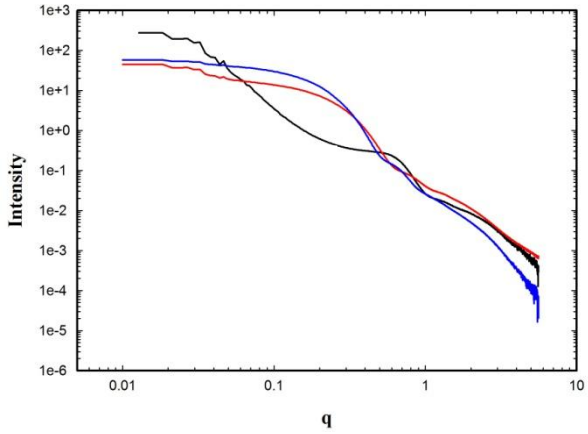

Figure 3.24(b): SAXS patterns for CS series: aliquot 1 (black curve), aliquot 10 (red curve) and aliquot 12 (blue curve).

There is a clear difference between the scattering produced by the Au seeds and the one produced by the heterostructures. The Au seed scattering curves from the two different series are very similar and show a distinct feature in log-log plots around Q = 0.7-0.8 nm^{-1}. This feature is due to both the form and structure factor of the Au spherical seed objects of dimension ~ 4.4 nm. On the contrary, the scattering curves from aliquots taken at larger reaction times show an increased intensity at low Q values, indicating scattering from objects with larger volume. The flat portion at low angles indicates that the structure factor contribution is negligible (no spatial interaction between particles). Moreover, the oscillations in the middle angle range denote that the system has limited polydispersity.

3.2.3.1.1 Guinier Analysis

In order to obtain an evaluation of the total particle diameter (D_v) we performed the Guinier analysis in the region (R_g* Q < 1) according to the equation 1.41, where R_g is the gyration radius.

R_g* Q < 1 defines the maximum Q value below which the Guinier law is valid. For a spherical object, the mean radius (R) of the particle is:

$$R_g^2 = \frac{3}{5} R^2 \qquad \text{Eq. 3.6}$$

To perform the Guinier analysis a flat Q region is needed; for this reason only few samples can be investigated with this method in particular aliquots 11, 12 and 13 for HD series and aliquots 10, 11 and 12 for CS series.

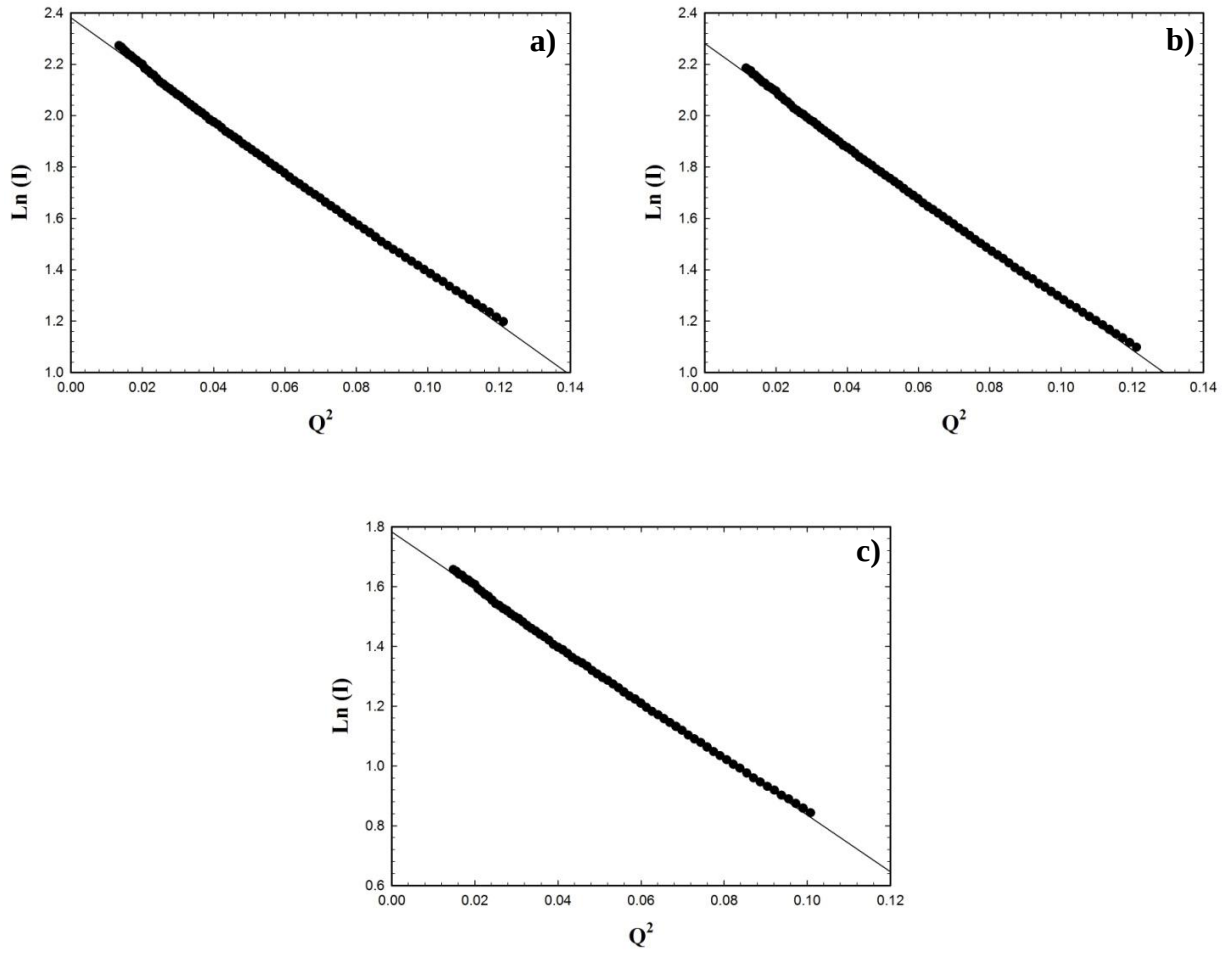

Figure 3.25: Guinier plots for HD series: a) aliquot 11, b) aliquot 12, c) aliquot 13.

In **Fig. 3.25** Guinier plots for the first series are reported, while in **Tab. 3.2** the results are shown.

	D_V total
Aliquot 11	14.20(4) nm
Aliquot 12	14.28(3) nm
Aliquot 13	13.76(2) nm

Table 3.6: Guinier results: mean diameters D_V are reported.

Probably the obtained values for the HD series are underestimate because of the sphere approximation. In HD series, the heterodimer samples have not a spherical shape and the obtained gyration radius R_g is not exact. In **Fig. 3.26** Guinier plots for the second series are reported.

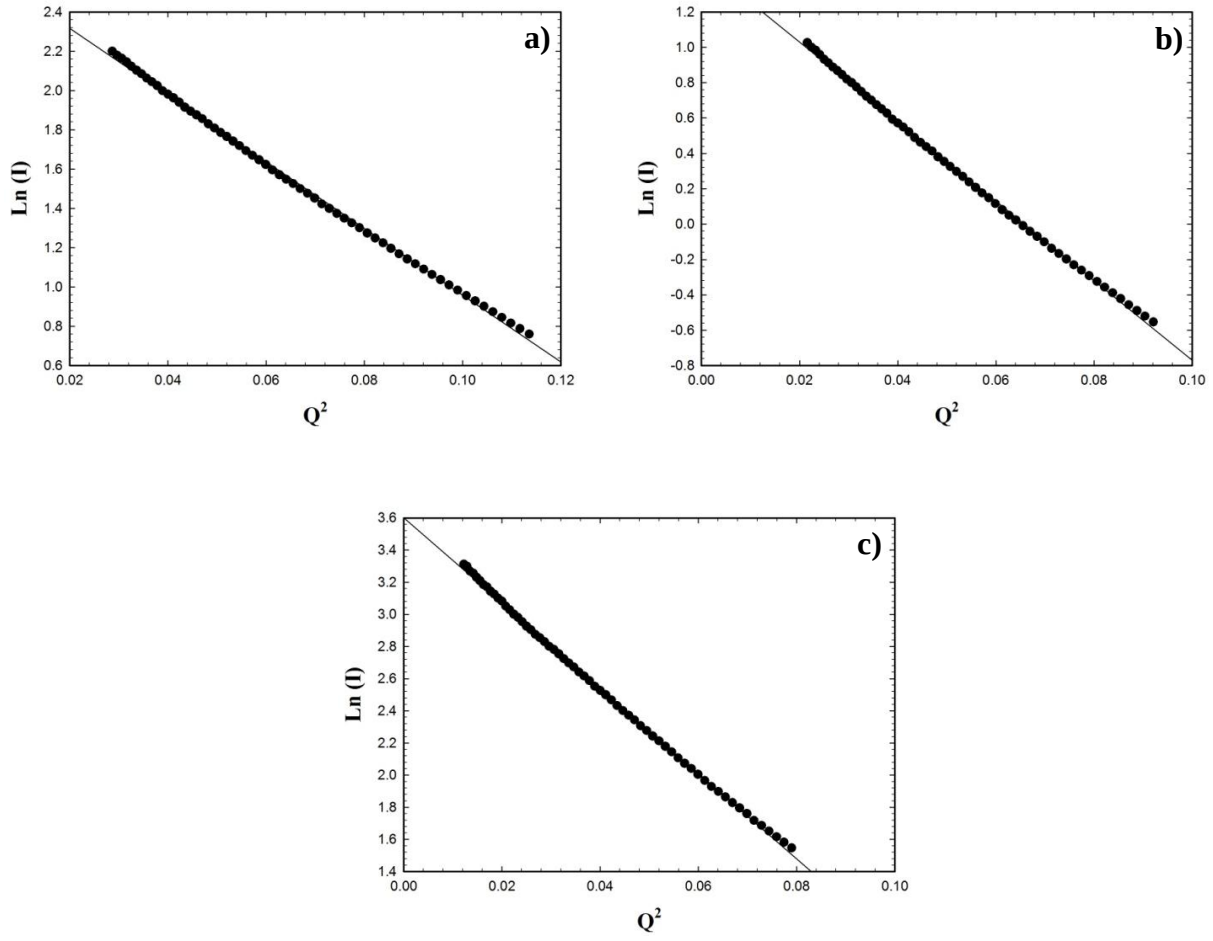

Figure 3.26: Guinier plots for CS series: a) aliquot 10, b) aliquot 11, c) aliquot 12.

In **Tab. 3.7** the Guinier analysis results of CS series are shown.

	D_V total
Aliquot 11	18.42(4) nm
Aliquot 12	21.21(5) nm
Aliquot 13	23.04(5) nm

Table 3.7: Guinier results: mean diameters D_V are reported.

The second series, related to core@shell sample, shows an increasing trend with regard to the mean diameter of the particle, with a value about 20 nm.

3.2.3.1.2 Modeling

Modeling starts with the aliquots with only gold seeds to find a gold radius value to keep fixed for the other refinements.

In **Fig. 3.27** we show the fits for the aliquot 2 in HD series (**Fig. 3.27(a)**) and for the aliquot 1 in CS series (**Fig. 3.27(b)**).

Due to the presence of two minima in the SAXS pattern for the first sample (**Fig. 3.27(a)**), two different populations of spheres are necessary in the refinement. Conversely, the presence of only one minimum in the SAXS pattern of the (**Fig. 3.27(b)**) indicates a monodispersion of gold seeds and a model with only one population of spheres allows to obtain a good refinement. For both samples we observed a gold radius about 4.4 nm, and this value was fixed for the other fits in order to obtain the iron oxide radius values. In HD series, since the presence of two populations of gold

seeds, the 4.4 value is related to the biggest one, but for the second population the gold radius value is about 4, very similar to 4.4 nm.

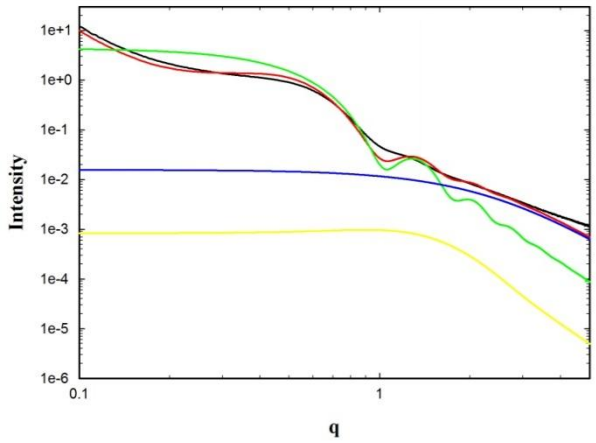

Figure 3.27(a): Aliquot 2, HD series. Raw data (black line), fit (red line), sphere1 (green line), sphere2 (yellow line) and background (blue line).

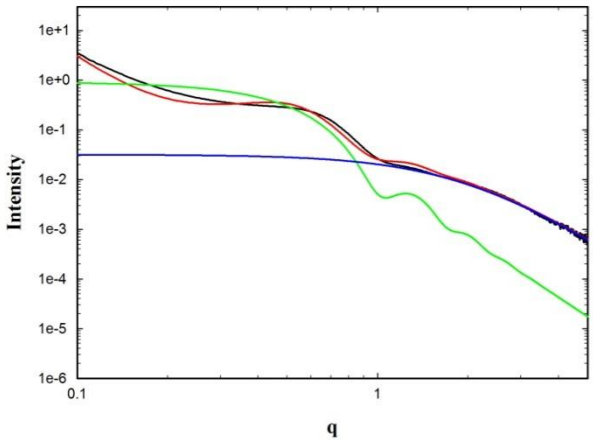

Figure 3.27(b): Aliquot 1, CS series. Raw data (black line), fit (red line), sphere 1 (green line) and background (blue line).

Then the refinements were performed on the heterostructures applying two different strategies and two different models to fit data of aliquots 11 and 13 for HD series and aliquots 10 and 12 for CS series.

As for the strategies, we fitted our data using both a monodispersed system (DBS – double shell system not interacting or interacting) and a polydispersed one (DBC – interacting or polydispersed core double shell), implemented in **[20]**. In both cases we kept fix the gold radius to the value obtained by the seeds (~ 4.4 nm).

In **Tab. 3.8** iron oxide radius values for all the samples are reported and **Fig. 3.28** shows their experimental data with their best fits.

HD series	Aliquot 11	Aliquot 13
Fe_3O_4 radius in monodispersed system	5.7(1) nm	5.7(6) nm
Fe_3O_4 radius in polydispersed system	4.4(1) nm	5.0(3) nm

CS series	Aliquot 10	Aliquot 12
Fe_3O_4 radius in monodispersed system	5.6(6) nm	6.6(2) nm
Fe_3O_4 radius in polydispersed system	7.5(4) nm	7.7(5) nm

Table 3.8: Fe_3O_4 radius for monodispersed and polydispersed systems.

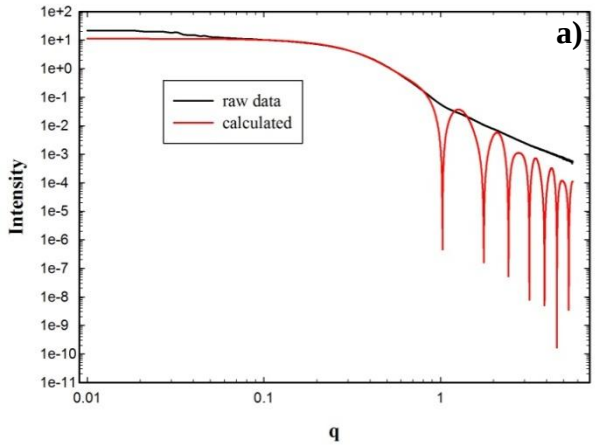

Figure 3.28(a): HD series, aliquot 11 in monodispersed system.

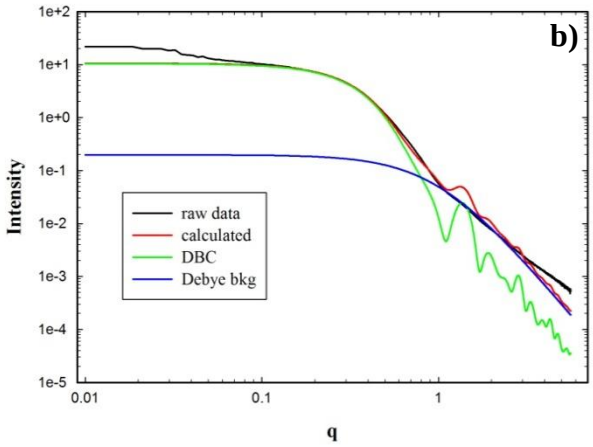

Figure 3.28(b): HD series, aliquot 11 in polydispersed system.

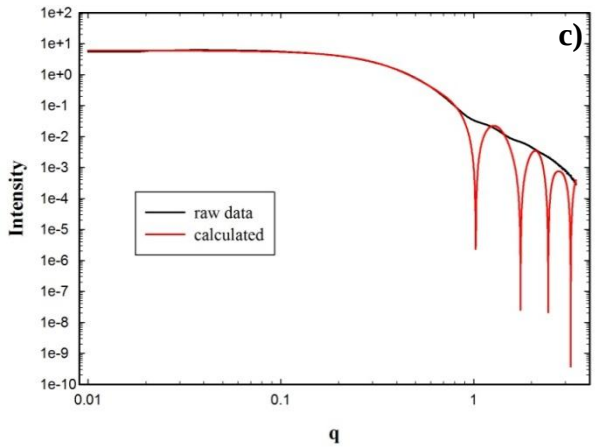

Figure 3.28(c): HD series, aliquot 13 in monodispersed system.

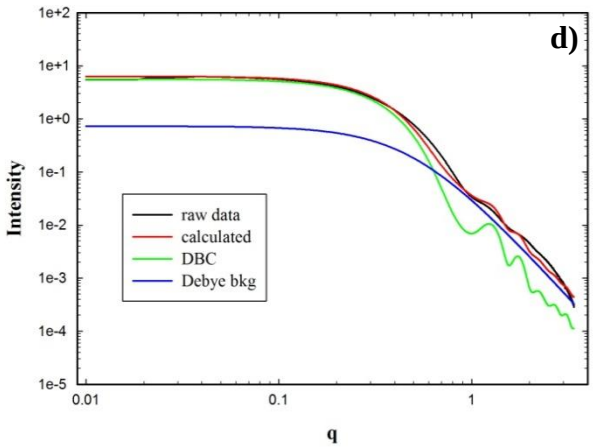

Figure 3.28(d): HD series, aliquot 13 in polydispersed system.

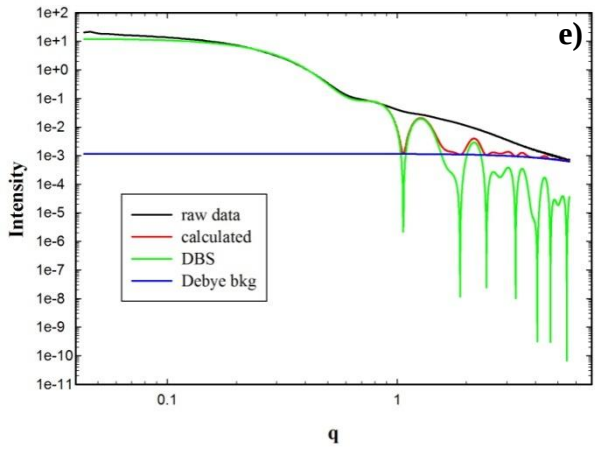

Figure 3.28(e): CS series, aliquot 10 in monodispersed system.

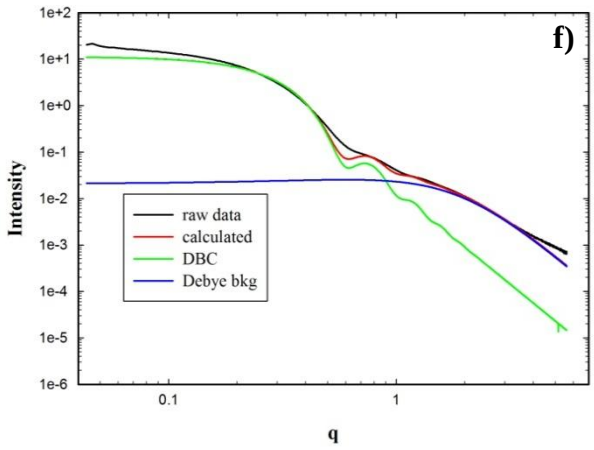

Figure 3.28(f): CS series, aliquot 10 in polydispersed system.

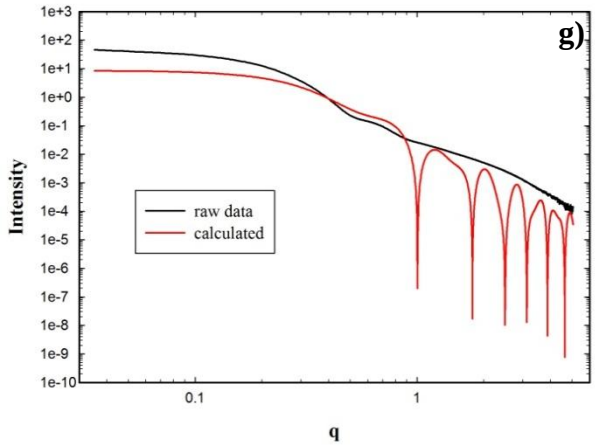

Figure 3.28(g): CS series, aliquot 12 in monodispersed system.

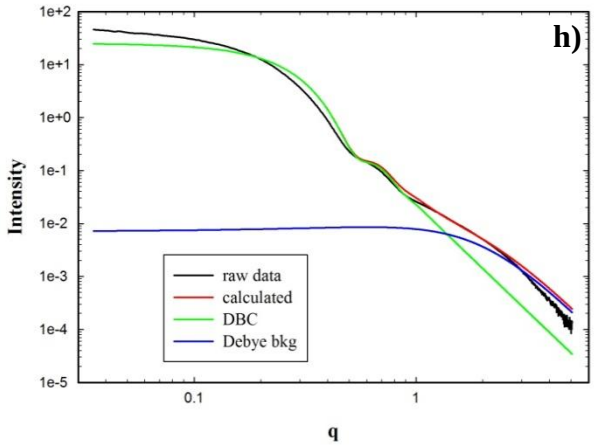

Figure 3.28(h): CS series, aliquot 12 in polydispersed system.

As for models, we used: i) two spheres model with two different spheres in contact (**Fig. 3.29(a)**) and ii) a core@shell model (**Fig. 3.29(b)**). As in the SAXS experiment we record the intensity averaged over all the possible orientation of the particles, it is possible to use of the core@shell model also for the heterodimer sample, as a first approximation.

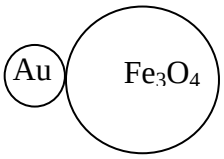

Figure 3.29(a): two spheres model.

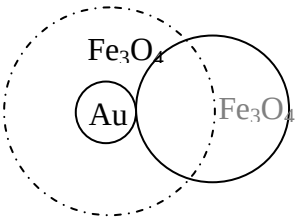

Figure 3.29(b): core@shell model.

Fig. 3.30 shows the fits obtained using the monodispersed approach, the best strategy, for both models (core@shell and two spheres) for the aliquot 13 of HD series. Both models are able to describe the cluster structure with good accuracy. In this case, the core@shell model works better as expected.

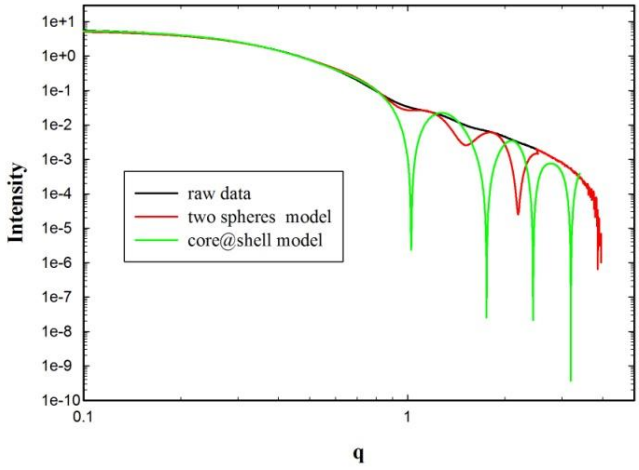

Figure 3.30: monodispersed system comparison for the two models.

However, the structural parameters calculated using the two models are quite similar and they are shown in **Tab. 3.9**.

HD series, Aliquot 13	Fe3O4 radius	Au radius
core@shell model	5.7(6) nm	5.0(3) nm
two spheres model	5.0(2) nm	4.1(3) nm

HD series, Aliquot 11	Fe3O4 radius	Au radius
core@shell model	5.7(1) nm	4.4(2) nm
two spheres model	6.1(3) nm	4.1(4) nm

Table 3.9: Fe_3O_4 radius for monodispersed and polydispersed systems in core@shell and two spheres model.

3.2.3.2 ESR Analysis

In **Fig. 3.31** the ESR spectrum of the HD sample is shown.

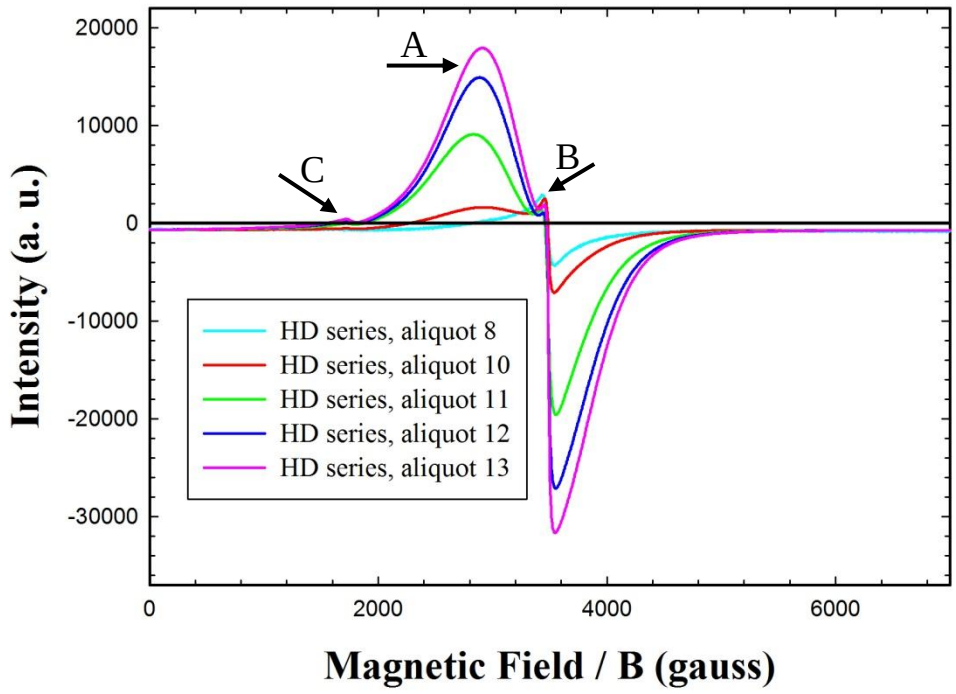

Figure 3.31: ESR spectra of HD series. X, Y and Z are related to the different features of ESR signal.

The spectrum is composed of three components. The most intense A and B features are characterized by nearly the same g ≅ 2 value but they have different spectral profile, the former being by far broader and more intense than the latter. The line C has a very low intensity and is detected at half the magnetic resonance field of the previous two features. The A line seems the most sensitive to the sample preparation time, as its intensity increases with it more markedly than the intensity of the other lines. Moreover, the A left peak moves towards higher field values with increasing temperature, as shown in **Fig. 3.32.**

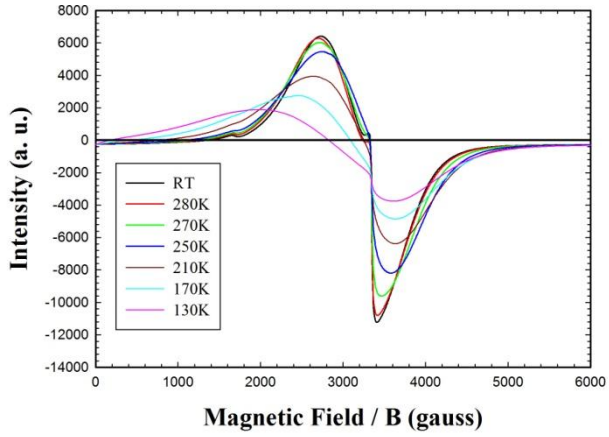

Figure 3.32(a): Aliquot 13, HD series. ESR signals as a function of temperature.

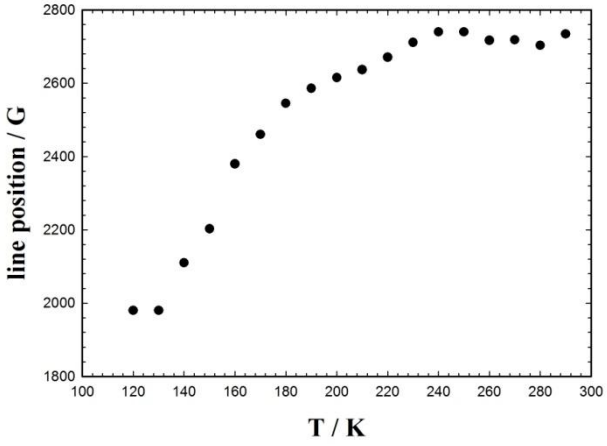

Figure 3.32(b): Aliquot 13, HD series. Line positions, related to ESR signals, as a function of temperature.

In **Fig. 3.33** the ESR spectrum of the CS sample is shown.

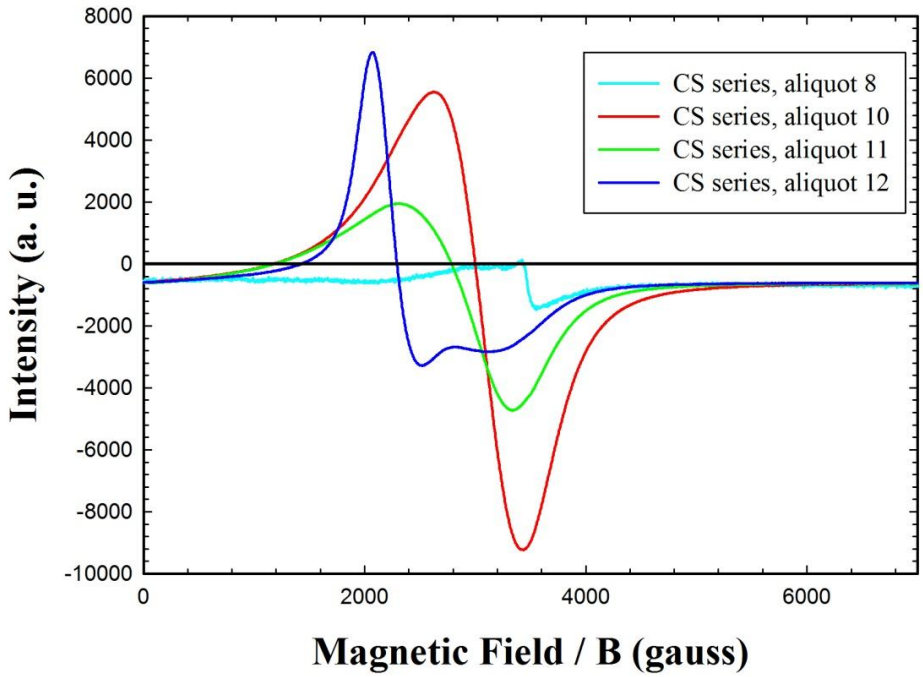

Figure 3.33: ESR spectra of CS series.

The ESR spectrum of the CS sample is completely different from that above discussed in **Fig. 3.31**. Indeed, after some preparation time, this sample shows a single, nearly symmetric line, broadening and moving towards lower field values at further delayed times and then splitting into two asymmetric features. The nearly symmetric broadens with increasing the detection temperature are shown for example in **Fig. 3.34** for aliquot 10.

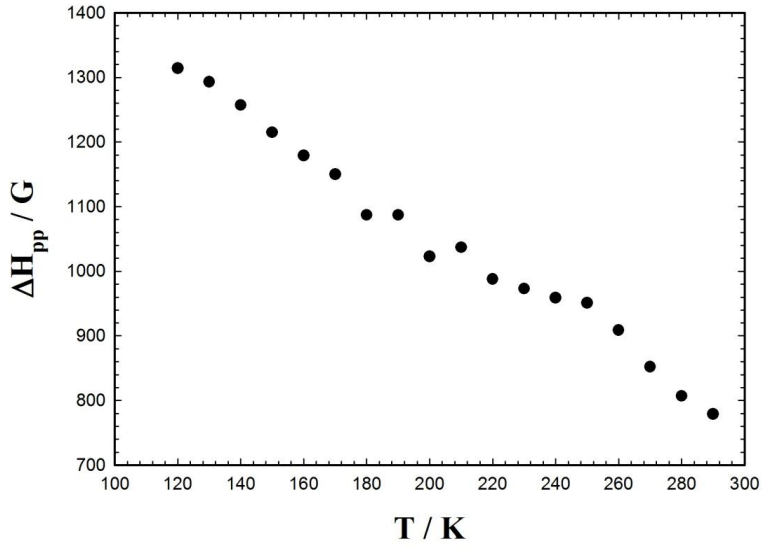

Figure 3.34: Aliquot 10, CS series. Broadening of the peak (ΔH_{pp}) as a function of T.

The ESR pattern of the HD sample is rather similar to that reported **[21]** with spinel-like iron oxide magnetic nanoparticles of 3.5 and 8 nm. A-like bands have been there attributed to particles characterized by bigger magnetic anisotropy with respect to those which cause the narrower B line. The latter particles could be smaller with respect to the former, and/or oriented with the easy axis making an angle close to the "magic angle" of 54.74° with the external magnetic field, so to minimize the broadening contribution due to the second-order Zero Field Splitting anisotropy field. An alternative explanation for the narrow B line is there proposed, attributing its appearance to the magnetic decoupling between the surface and the core of the MNPs. On the other hand, the broader A line narrows with increasing temperature because its left lobe moves towards higher field values

(see **Fig. 3.32**), suggesting that the large width of this ESR band is really due to the anisotropy field of the MNPs, becoming less effective at higher temperature. Finally, the C low-intensity band is attributed to the formally forbidden $\Delta M = \pm 2$ transition due to mixing of the $M = \pm 1$ states, perhaps occurring in distorted octahedral coordination sites **[22]**. Quite interestingly, it has been also reported **[21]** that the sharp signal B is due to MNPs with approximately the same orientation at which the $\Delta M = \pm 2$ appears, and quantum-mechanical considerations have been there proposed.

But the most interesting consideration is that the anisotropy field of the MNPs are not affected by the delayed preparation time. Indeed, samples analyzed after increasing preparation times have ESR spectra of increasing intensity, as expected, but with the same width (see **Fig. 3.31**). This means that these samples contain an increased concentration of MNPs, but that the size of the last does not increase with time. In fact, an increased size of the MNPs would lead to a larger anisotropy field and therefore to a broader ESR feature.

Conversely, the changes of the ESR spectral profile above reported for CS (see **Fig. 3.33**) indicates that its anisotropy field changes with the time delayed during the sample preparation. In particular, the intense nearly symmetric ESR line of aliquots 10 and 11 can be attributed to the formation of small (single magnetic domain) superparamagnetic particles as in **[23]**. This is confirmed by the fact that the ESR line of aliquot 11 is a bit broader than aliquot 10. Indeed, thermal motions are a bit less effectual in mediating the magnetic anisotropies with larger superparamagnetic particles **[24]**. Furthermore, the ESR line-width of the superparamagnetic particles narrows with increasing temperature **[23, 24]**, as also here reported in **Fig. 3.34** for the aliquot 10 of CS series. At last, when the CS particles becomes too large to be single-domain, they become ferromagnetic, with a significant magnetic anisotropy as for the aliquot 12 of CS, analogously to what reported in literature **[22, 25]** for similar systems.

3.2.4 Structural Study

3.2.4.1 Reciprocal Space Analysis

Au nanoparticles and NHs have been characterized with Transmission Electronic Microscopy and Visible light Absorption Spectroscopy to confirm the configuration core@shell or heterodimer. **Fig. 3.35(a)**, **(c)** and **(e)** (left) show the TEM images pertinent to Au nanoparticles, HD and CS nanocomposites respectively. On the right hand side of the same figure the UV-Vis spectra for the same samples are displayed. The TEM image show that Au nanoparticles are almost spherical. In the pertinent UV-Vis spectrum the plasmonic band is apparent at about 540 nm. We recall that plasmons are surface fluctuations of the free electron density in metals. The TEM image of **Fig. 3.35** shows small dark Au spheres and big gray Fe_3O_4 nanoparticles connected by small surfaces typical of HD configuration. Since the Au nanoparticles are only partially surrounded by Fe_3O_4 the plasmon band is still present in the UV-Vis spectrum. In the TEM image of CS sample the Au dark spheres are embedded in the big gray Fe_3O_4 ones. Since no free Au surface is present, the plasmon resonance peak is absent in the CS spectrum (see **Fig. 3.35**, right).

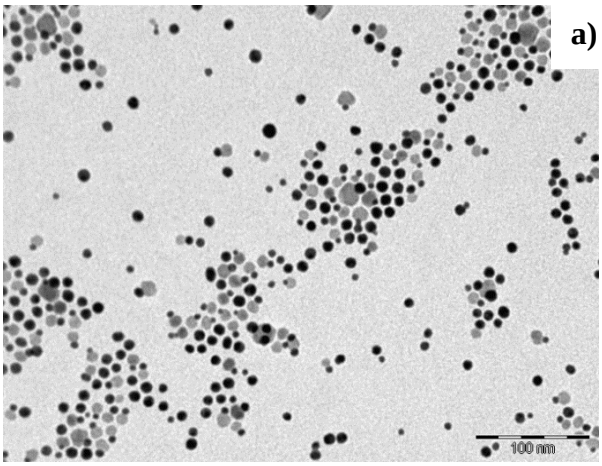

Figure 3.35(a): TEM image Au nanoparticles sample.

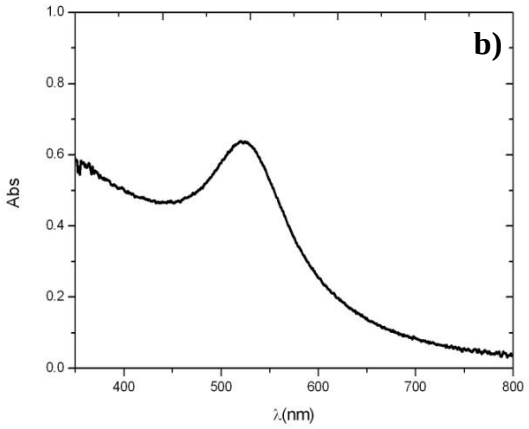

Figure 3.35(b): Absorption spectrum of Au nanoparticles sample.

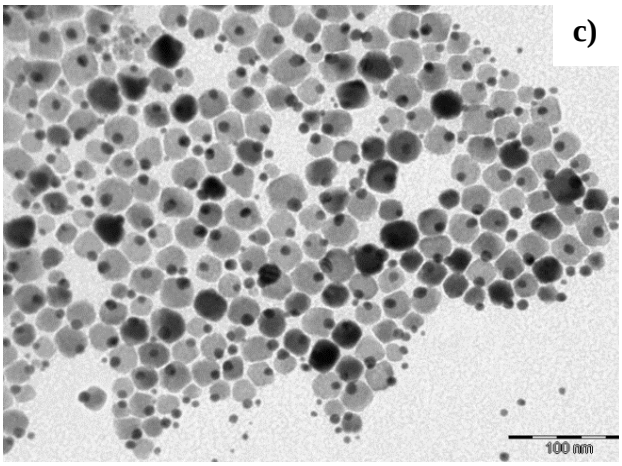

Figure 3.35(c): TEM image of heterodimer sample.

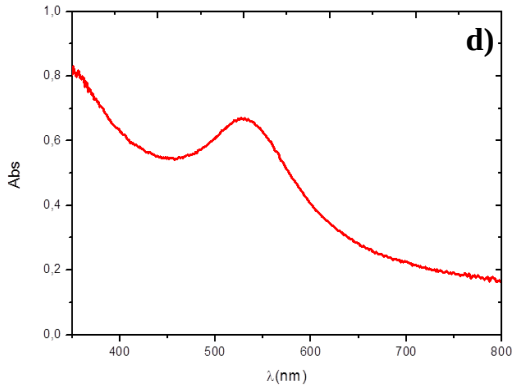

Figure 3.35(d): Absorption spectrum of heterodimer sample.

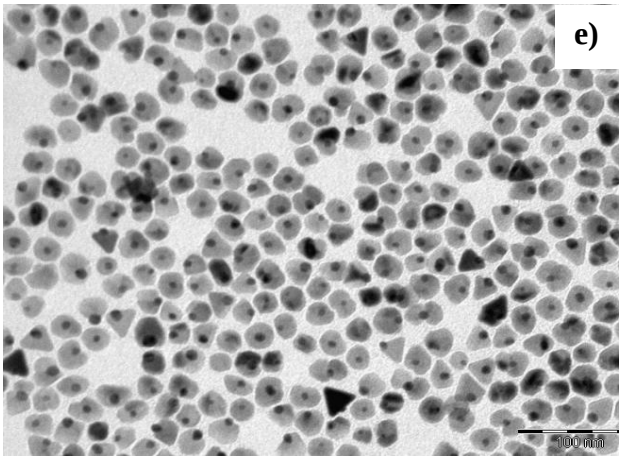

Figure 3.35(e): TEM image of core@shell sample.

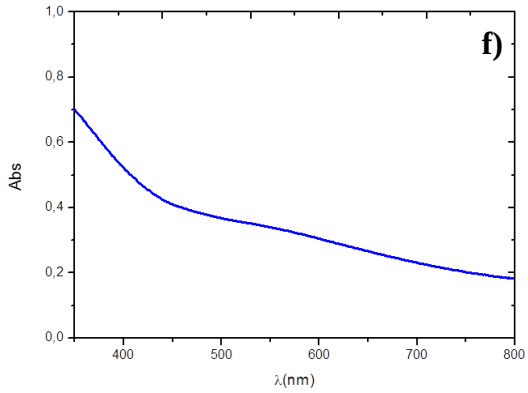

Figure 3.35(f): Absorption spectrum of core@shell sample.

PDF quality synchrotron radiation powder diffraction patterns have been collected on the above samples. Data have been analyzed using the Rietveld method, the Williamson-Hall method and the PDF analysis.

The average crystallographic structure was determined through Rietveld method varying in each refinement the cell parameter, the oxygen position and using an average isotropic mean square displacement (*msd*).

A biphasic system is observed both in core@shell and heterodimer samples. In particular, the Fe_3O_4 magnetite phase, and the metallic gold phases are present, both displaying space group *Fm*-3*m*.

Fig. 3.36 shows the experimental patterns (black crosses) of Au seeds nanoparticles (**Fig. 3.36(a)**) and Fe_3O_4-Au nanocomposites in CS (**Fig. 3.36(b)**) and HD (**Fig. 3.36(c)**) configuration together with their best fits (red curves). Results of the refinements are reported in **Tab. 3.10**.

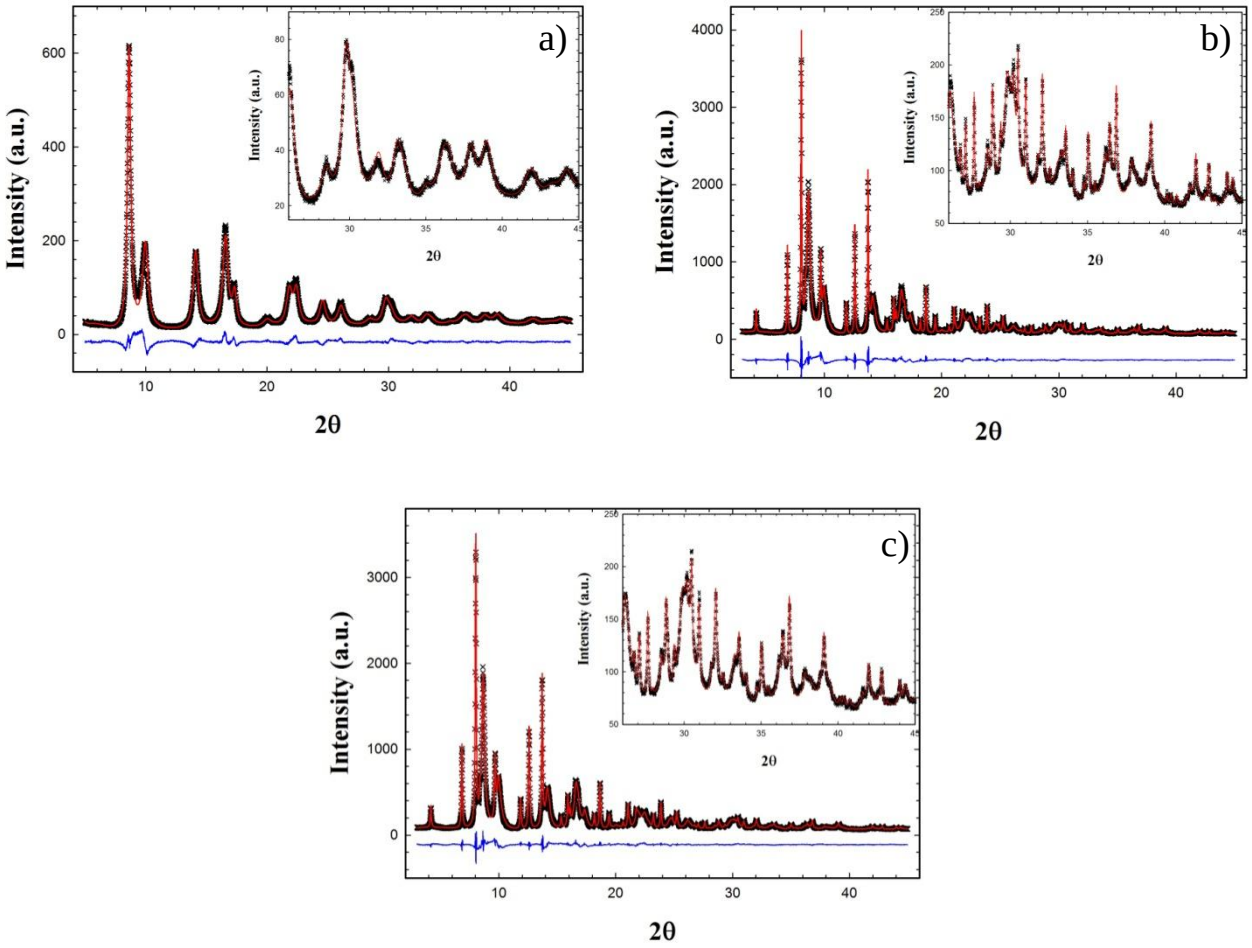

Figure 3.36: Rietveld refinements for Au (Fig. X1a), heterodimer (Fig. X1b) and core@shell (Fig. X1c). Experimental pattern (black crosses), fit (red curves) and differential (blue line) are reported. In the insets the high 2θ range is highlighted.

The pattern in **Fig. 3.36(a)** can be fitted using a cubic face centered Au phase, space group *Fm*-3*m*. The patterns in **Fig. 3.36(b)** and **3.36(c)** are fitted using the Au phase and a spinel-like Fe_3O_4 magnetite phase, space group *Fd*-3*m*.

As to the iron oxide phase, the high-*Q* resolution and to the high statistics obtained at the ID22 beamline allow to establish the presence of only Fe_3O_4 magnetite phase in both samples; in fact, the presence of γ-Fe_2O_3 can be excluded on the basis of the absence of superstructure peaks typical of maghemite phase and of the experimental cell constants (see **Tab. 3.10**). In particular, the cell constant of CS sample (a=8.3902) is slightly larger of the HD sample one (a=8.3844).

Phase	Parameter	Au nanoparticles	heterodimer	core@shell
Au	**Space Group**	F*m-3m*	F*m-3m*	F*m-3m*
	a / Å	4.0770(3)	4.0672(4)	4.0545(6)
	***msd* / Å^2**	0.0045 (2)	0.0049(2)	0.0056 (1)
	% Weight	100	27.3(2)	22.5(5)
	D_v / nm (W-H)	6.5(1.0)	6.4(1.5)	6.2(1.0)
	ε (W-H)	4.1(4)e-2	4.8(7)e-2	3.2(5)e-2
Fe_3O_4	**Space Group**		F*d-3m*	F*d-3m*
	a / Å		8.3844(2)	8.3902(2)
	x(O)		0.2565(2)	0.2565(2)
	***msd* (Fe) / Å^2**		0.0058 (2)	0.0058(1)
	***msd* (O) / Å^2**		0.0026 (5)	0.0033(4)
	% Weight	0	72.7(9)	77.5(6)
	D_v / nm (W-H)		19.7(7)	15.6(5)
	ε (W-H)		1.3(4)e-3	3.4(5)e-3
G.o.f.	**R (F^2)**	0.0202	0.0264	0.0263

Table 3.10: Rietveld refinement and WH parameters.

As to the Au phase, the cell parameter of seeds nanoparticles (4.077 Å) is close to metallic gold materials one (a=4.078 Å) **[26, 27]** while a contraction is well apparent for nanocomposites, which is more evident for the CS sample (~0.6%) with respect to HD one (~0.3%).

The size and strain analysis of the samples was carried out using the Williamson-Hall method. The pertinent plots are shown in **Fig. 3.37**, while the results are displayed in **Tab. 3.10**. The diffraction peaks have been fitted using pseudo-Voigt function and the instrumental contribution to peaks broadening has been determined using a CeO_2 standard and subtracted to the experimental width.

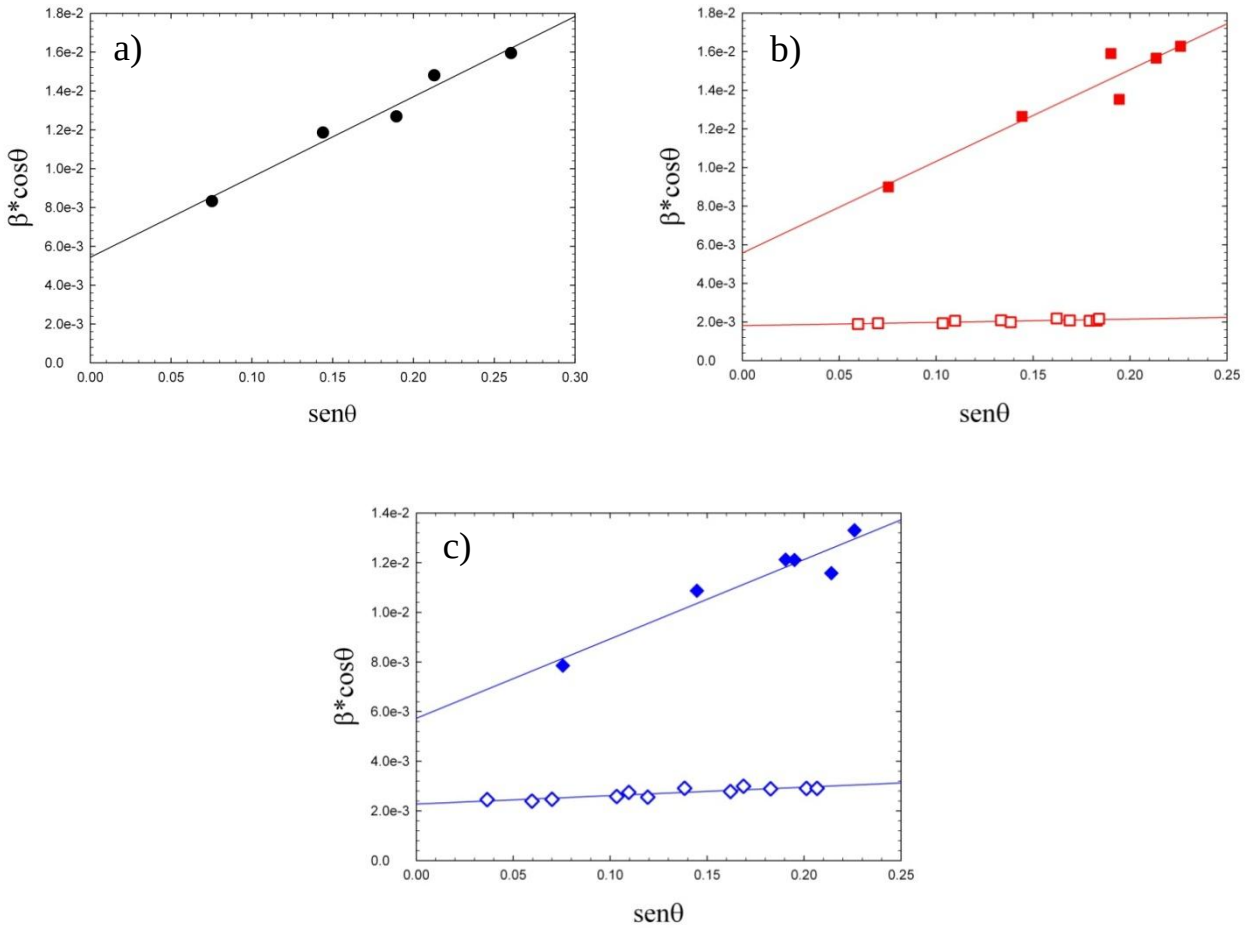

Figure 3.37: Williamson–Hall plot analysis for Au (a), HD (b) and CS (c) samples. Full and empty symbols refer to Au and Fe_3O_4 phases, respectively.

For all the samples D_V for the Au phase is about ~6 nm, while D_V is ~19 and ~16 Å for magnetite in HD and CS configuration respectively. The gold phase seems to be mainly affected by strain in respect to magnetite: $\varepsilon \approx 3\text{-}5 \cdot 10^{-2}$ for the former and $\approx 1\text{-}3 \cdot 10^{-3}$ for the latter.

Focusing on Au phase, the above results can be understood in the framework of both homogeneous strain (HS) and inhomogeneous strain (IHS), where HS causes a uniform shift (contraction) of the cell parameters in the nanocomposite samples, in respect to Au nanoparticles, while IHS is related to the dispersion of cell constants, seems to be similar for the three samples **[28]**.

3.2.4.2 Real Space Analysis

The experimental *G(r)* functions for the three samples considered are shown in **Fig. 3.38** (black symbols) together with the best fits (red lines) and residuals (blue lines) of the PDF fits. The insets report the low r region of the same PDF functions.

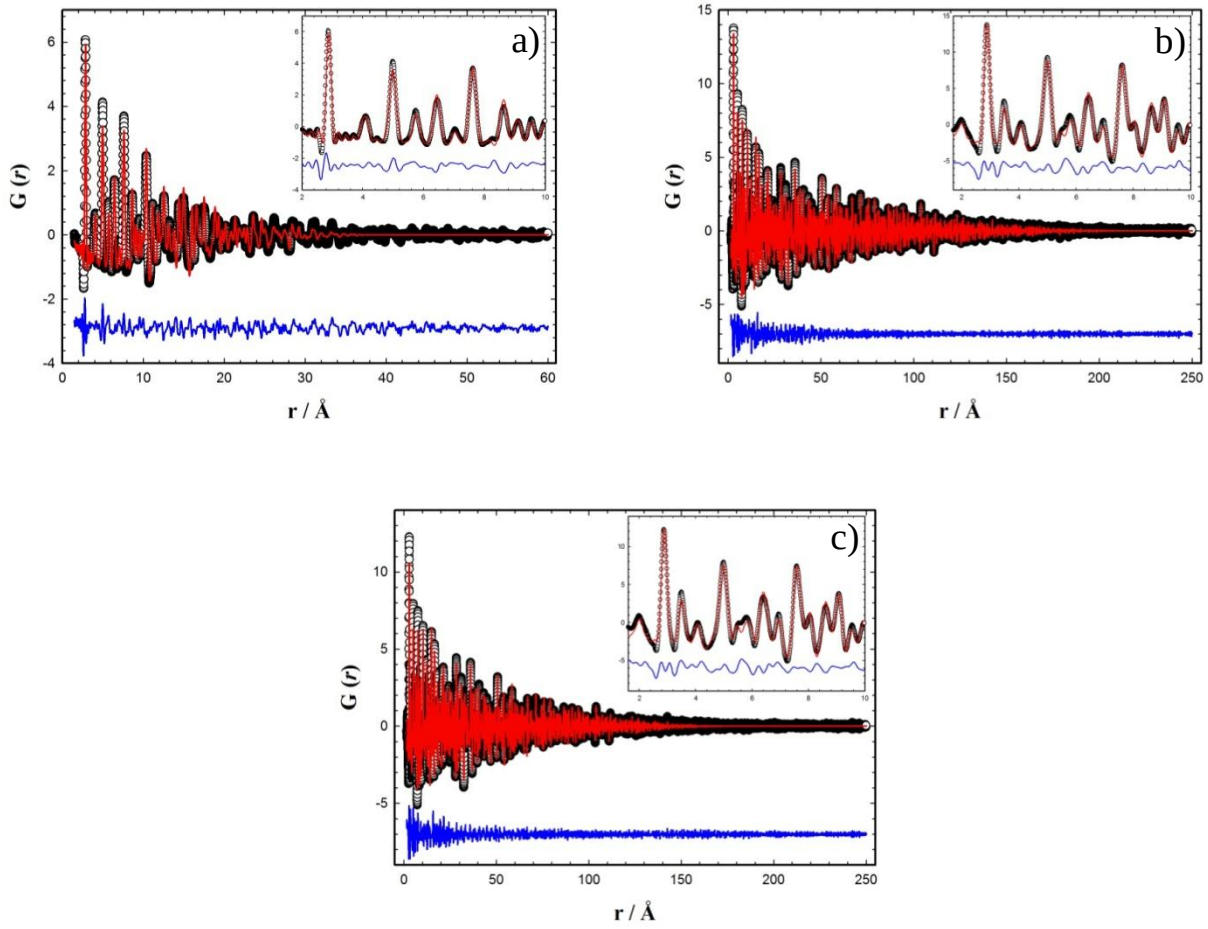

Figure 3.38: PDF refinements for Au (Fig. X2a), heterodimer (Fig. X2b) and core@shell (Fig. X2c). Experimental pattern (black circles), fit (red curves) and differential (blue line) are reported. In the three insets the $1.5 < r < 10$ Å range is shown.

The PDF fits were performed using the same gold and magnetite phases described above for the reciprocal space analysis. In each refinement, cell parameter(s) and *msd* parameters were varied as well as the scale factors and the envelope parameter. The latter takes into account the damping of

the *G(r)* peaks arising from the limited coherence length of the nanocrystals. The size values obtained by this approach, and shown in **Tab. 3.11,** are comparable to those found through the WH method. The structural parameters obtained fitting the *G(r)* curves in the *r* ranges displayed in **Fig. 3.38** are shown in **Tab. 3.11**.

Phase	Parameter	Au nanoparticles	heterodimer	core@shell
Au	**Space Group**	F*m-3m*	F*m-3m*	F*m-3m*
	a / Å	4.0751(12)	4.0697(1)	4.0600(5)
	***msd* / Å^2**	0.00863(48)	0.01004(21)	0.00917(18)
	Mass fraction	100	0.3671(36)	0.3025(33)
	D_v	4.8(3)	5.1(1)	4.8(7)
Fe_3O_4	**Space Group**		F*d-3m*	F*d-3m*
	a / Å		8.3851(2)	8.3904(2)
	***msd* (Fe1) / Å^2**		0.00519(25)	0.00450(26)
	***msd* (Fe2) / Å^2**		0.00815(24)	0.00800(26)
	***msd* (O) / Å^2**		0.01634(96)	0.01493(97)
	Mass fraction		0.6329(36)	0.6975(33)
	D_v		22.6(3.1)	17.7(3.2)
G.o.f.	**Rw**	0.2446	0.2054	0.2304

Table 3.11: PDF fit parameters.

As a general comment we observe that the Au and magnetite structural models fit well the experimental *G(r)*s. This suggests that nanostructuring and nanocomposite formation do not induce significant changes in any of the two phases. As to the Au seed, we can note that the Au cell constant reported in **Tab. 3.11** (a≈4.075 Å) is in line with the results of Page et *al*. **[27]** (a≈4.076 Å) for nanoparticles of similar dimension (diameter ≈4 nm).

As to NHs samples, in accord to the reciprocal space analysis, the Fe_3O_4 phase in CS sample expands in respect to the HD one and, compared to Au seeds the gold phase is observed to contract in nanocomposites, especially in CS configuration (see **Tab. 3.11**).

To map the coherence domain of Au-Au bonds contraction, fits were performed also in small (each 5 Å wide) different *r* ranges to check for the possible presence of short range disorder. To avoid

over-parameterization the weight fractions and the envelope parameters have been fixed to the values of **Tab. 3.11**.

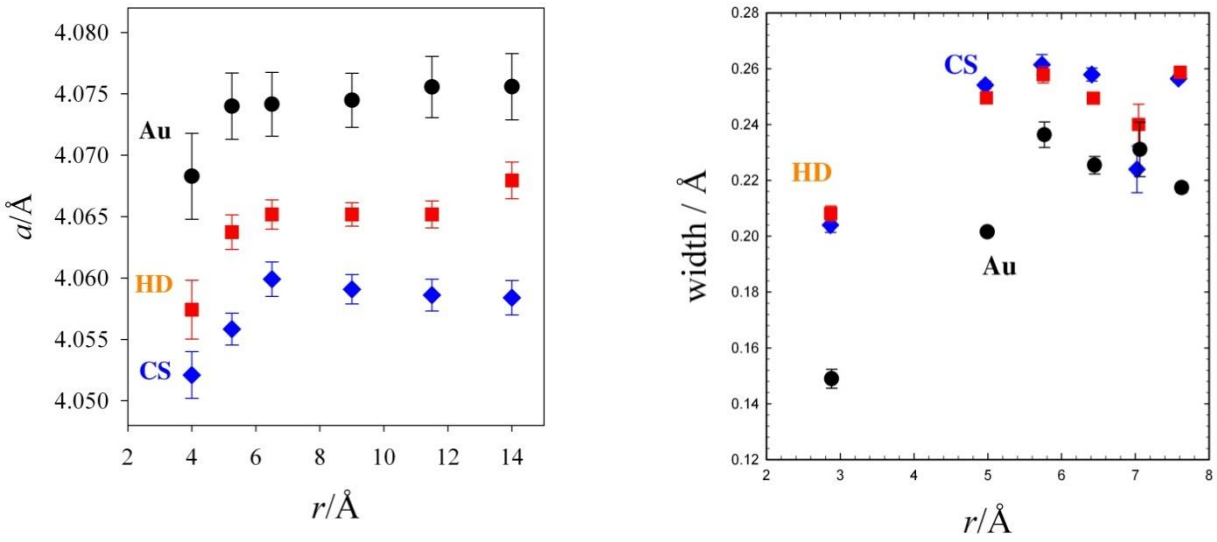

Figure 3.39: Left: Au cell parameters a as a function of r. The r values are the centroids of the fitting intervals. Right: width of *G(r)* peaks Vs. r. In both panels the black, red and blue symbols refer to Au seeds, HD and CS samples respectively.

Fig. 3.39 shows the Au cell parameters *a* obtained as a function of *r*. The *r* values are the centroids of the fitting intervals. At very low *r* values, for all the samples, *a* is smaller than the one obtained with the fit in a wide *r* range. However, at increasing *r*, *a* cell constants rich rapidly the values displayed in **Tab. 3.11**.

Tab. 3.11 also shows that *msd* values for gold in both nanocomposites are larger with respect to Au seeds. In the *G(r)* curves the *msd* values, due to both thermal vibration and disorder, causes the broadening of the *G(r)* peaks as a consequence of broader bond length distribution.

Experimental *G(r)* peaks pertinent to Au-Au distances have been also fitted using Gaussian Functions after baseline subtraction as described in **[26, 29]**. **Fig. 3.39** (right panel) reports the full width at half maximum of peaks for gold seeds nanoparticles (blue circles), heterodimer (red circles) and core@shell (black circles) as a function of *r*. The width of Au nanoparticles is smaller

than for CS and HD samples, especially at very low *r* values, suggesting that a wider distribution of interatomic distances is present.

All the above results can be visualized comparing the *G(r)* functions of the three samples (see **Fig. 3.40**).

In the left hand side panel are shown low-*r* portions of PDFs for all the samples. In the case of NHs the fitted Fe_3O_4 contribute has been subtracted to the experimental *G(r)*s obtaining "differential" $G(r)_{Au}$ in order to highlight the Au contribution. At the left side of the break in **Fig. 3.40** it is possible to note the broadening of the first neighbour Au-Au peaks pertinent to NHs in respect to Au seeds; at the right side, the same effect goes along with the shift of *G(r)* peaks pertinent to CS and HD samples towards smaller *r* values in respect to Au.

Focusing on the Fe_3O_4 phase, in the upper panel of **Fig. 3.40** is shown, as an example, the 74≤r≤78 Å interval of the *G(r)*s pertinent to the two nanocomposites (HD red curve, CS blue curve); at these high-*r* values, *r* range where the contribution of Au is negligible, the rigid shifts of the CS sample peaks towards high *r* values in respect to the HD sample is apparent.

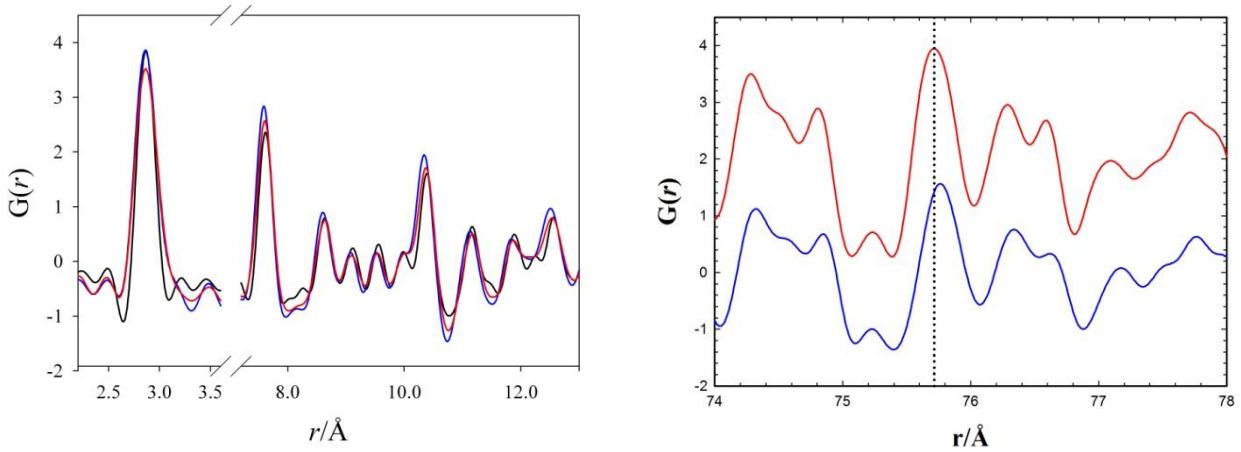

Figure 3.40: Left: short *r* range portions of the xperimental *G(r)* curve of Au seeds and of the "differential" ones of HD and CS samples obtained subtracting the calculated Fe_3O_4 contributions. Right: Portion of the xperimental *G(r)* curves of HD and CS samples. In both panels the black, red and blue curves refer to Au seeds, HD and CS samples respectively.

3.2.5 Discussion

In Au seeds, the peak width is ≈0.15 Å for the next neighbour (NN) Au-Au distance and it increases rapidly at increasing *r* reaching a plateau (width ≈0.22-0.23 Å) for distances larger than 5 Å. This is consistent with Au-Au motion correlation at very low distances. In the NHs case, the peak width for the Au-Au NN distance is ≈0.20 Å. Since all the measurements have been performed at the same temperature, this suggests that a larger distribution of Au-Au distances (disorder) is present in these samples. By increasing *r*, the peak width increases too, but at a smaller extent in respect to Au seeds. However, as testified by the average cell constant values reported in **Tab. 3.11,** the average Au-Au distances are shorter than in Au seeds. Besides, The *r*-series PDF analysis showed a contraction of the Au cell constants (which is related to the position of Au-Au *G(r)* peaks) at low *r* values, but they increase rapidly and, reach the "average" values for r≈5-6 Å (see **Fig. 3.39**).

Both the peak enlargement and the cell contraction at low interatomic distances suggest that, in NH materials, "zones" with different equilibrium Au-Au interatomic distances exists and that the coherence length of these "zones" is very short (about 5 Å). Moreover both the effects should be considered a feature induced on gold by the Fe_3O_4 counterpart. In fact, the cell contraction is more evident in the CS sample where the Au/Fe_3O_4 surface is bigger.

The Au cell contraction can be considered as a chemical pressure effect induced on Au by the Fe_3O_4 shell. Several papers **[30, 31]**, measured the Au cell parameters as a function of *P*. In particular, on the basis of the data interpolation of **[31]** it was possible to estimate, an "average" chemical pressure on gold of ≈3 and ≈1.5 GPa in CS and HD, respectively, while it is about 0 for the gold "naked" seed, see **Fig. 3.41** and **Tab. 3.12**.

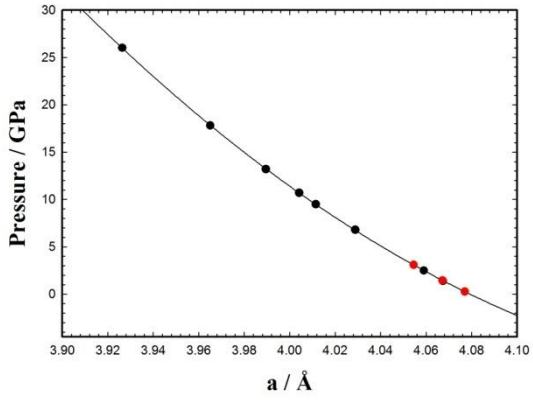

Figure 3.41: Plot of data interpolation of **[30]**.

a (Au) (Å)	Pressure (GPa)
4.0770	0.3
4.0674	1.4
4.0672	1.5
4.0590	2.5
4.0545	3.1
4.0288	6.8
4.0115	9.5
4.0042	10.7
3.9895	13.2
3.9651	17.8
3.9264	26

Table 3.12: Results of data interpolation of **[30]**.

However, on the basis of the width of the NN Au-Au peak in NHs, it is worth supposing that in CS and HD samples the compressive strain is not uniform but is larger at the interface than in the inner part of the gold nanoparticle; since for spherical particles of 5 nm in diameter about 40% of Au atoms are within 4-5 Å from the surface (the coherence length of the strain-inhomogeneity on the basis of **Fig. 3.39**) the chemical pressure induced on gold by Au-Fe_3O_4 interface should be almost doubled (≈5-7 GPa) in respect to the average one.

As to the magnetite shell, it is possible to note in Cs sample, in respect to the HD one, the concomitant increase of ε ($3.4*10^{-3}$ vs. $1.7*10^{-3}$) and cell parameter (~0.07%), which suggest that the interphase surface induces strain also in this phase; however in Fe_3O_4 the strain effect seems to be less evident because of the much smaller percentage of Fe and O ions at the interphase surface.

Thus, our SR-XRPD study in the reciprocal and real space has revealed that in Au-Fe_3O_4 nano-hetero-structure the main effect of the Au-Fe_3O_4 interface formation s to induce compressive strain on metallic gold and tensile strain on magnetite. Obviously, our investigation cannot supply a detailed description of the (possible) structure reconstruction at the interface since XRPD is a bulk technique and, especially for the Fe_3O_4 phase, only a small percentage of atom are nearby interface.

However, in the case of Au, it is possible to infer that strain is not uniform within the nanoparticle and the surface should experience a chemical pressure which is higher than in the core of Au nanoparticles.

This suggests that iron oxide grows epitaxially on gold and the mismatch between the two phases induces big strain on both of them, and in particular on gold. How shown by the results presented in this chapter, this strain is bigger in core@shell structure where the contact surface area between iron oxide and gold, in respect to the heterodimer one, is bigger.

The epitaxially growth and the consequent strain induced by it could be the reason why the coupling of two different phase can bring to unique physical properties non accessed with any of the single components alone.

References

[1] K.S. Kumar, H. Van Swyggenhoven, S. Suresh, *Acta Mater.*, **2003**, 51, 5743

[2] M.A. Meyers, A. Mishra, D.J. Benson, *Prog. Mater. Sci.*, **2006**, 51, 427

[3] M. Dao, L. Lu, R.J. Asaro, J.T.M. De Hosson, E. Ma, *Acta Mater.*, **2007**, 55, 4041

[4] Z. Xu, Y. Hou and S. Sun, *J.Am. Chem. Soc.* **2007**, 129, 8698-8699

[5] L. Wang, J. Luo, Q. Fan, M. Suzuki, I.S. Suzuki, M.H. Engelhard, Y. Lin, N. Kim, J.Q. Wang and C.J. Zhong, *J. Phys. Chem. B* **2005**, 109, 21593-21601

[6] C. Xu, J. Xie, D. Ho, C. Wang, N. Kohler, E.G. Walsh, J.R. Morgan, Y.E. Chin and S. Sun, *Angew. Chem. Int. Ed.* **2008**, 47, 173-176

[7] E.V. Shevchenko, M.I. Bodnarchuk, M.V. Kovalenko, D.V. Talapin, R.K. Smith, S. Aloni, W. Heiss and A.P. Alivisatos, *Adv. Mater.* **2008**, 20, 4323-4329

[8] K.L. Krycka, J.A. Borchers, G. Salazar-Alvarez, A. Lopez-Ortega, M. Estrader, S. Estrade, E. Winkler, R.D. Zysler, J. Sort, F. Peirò, M.D. Barò, C.C. Kao and J. Nogues, *ACS Nano* **2013**, 7, 921-931

[9] J.J. Urban, D.V: Talapin, E.V. Shevchenko, C.R. Kagan and C.B. Murray, *Nat. Mater.* **2007**, 6, 115

[10] F. Pineider, C. de Julian Fernandez, V. Videtta, E. Carlino, A. al Hourani, F. Wilhelm, A. Rogalev, P.D. Cozzoli, P. Ghigna and C. Sangregorio, *ACS Nan**o*** **2013**, 7, 857-866

[11] M.B. Cortie, A.M. McDonagh, *Chem. Rev.* **2011**, 112, 3713-3735

[12] P.D. Cozzoli, T. Pellegrino and L. Manna, *Chem. Soc. Rev.* **2006**, 35,1195-1208

[13] L. Carbone, P.D. Cozzoli, *Nano Today*, **2010**, 5, 449

[14] W. Shi, *Nano Lett.*I, **2006**, 6, 875

[15] H.T. Zhang, *Langmuir*, **2008**, 24, 13197

[16] J. Bao, W. Chen, T. Liu, Y. Zhu, P. Jin, L. Wang, J. Liu, Y. Wei and Y. Li, *ACS Nano*, **2007**, 4, 293-298

[17] K. Sokolov, M. Follen, J. Aaron, I. Pavlova, A. Malpica, R. Lotan, R. Richards-kortum, *Cancer Res.*, **2003**, 63, 1999-2004

[18] R. Frison, G. Cernuto, A. Cervellino, A. Guagliardi and N. Masciocchi, *Chem. Mater.*,**2013**, 25 (23), 4820-4827

[19] P. Podsadlo, S.G. Kwon, B. Koo, B. Lee, V.B. Prakapenka, P. Dera, K.K. Zhuravlev, G. Krylova and E. Shevchenko, *J. Am. Chem. Soc.* **2013**, 135, 2435-2438

[20] G. Portale private communication

[21] M. Fittipaldi, C. Innocenti, P. Ceci, C. Sangregorio, L. Castelli, L. Sorace and D. Gatteschi, *Physical Review B*, **2011**, 83, 104409

[22] H. Fischer, J. Luster, and A.U. Gehring, *Geophys. J. Int*., **2007**, 169, 909-916

[23] Y. Köseoğlu, F. Yıldız, D.K. Kim, M. Muhammed, and B. Aktas, *Physica Status Solidi C*, **2004**, 1, 3511-3515

[24] L. Bonneviot and D. Olivier, "*Catalyst Characterization: Physical Techniques for Solid Materials*", B.Imelik and J.C.Vedrine, eds., Plenum Press, New York, **1994**

[25] S. Watanabe, S. Akutagawa, K. Sawada, T. Iwasa, and Y. Shimoyama, *Materials Transactions*, **2009**, 50, 2187-2191

[26] Q.F. Gu, G. Krauss, W. Steurer, F. Gramm and A. Cervellino, *Physical Review Letters*, **2008**, 100, 045502

[27] K. Page, T, Proffen, H. Terrones, M. Terrones, L. Lee, Y. Yang, S. Stemmer, R. Seshadri and A.K. Cheetham, *Chemical Physics Letters*, **2004**, 393, 385-388

[28] X. Yang, A.S. Masedah, J.R. McBride, E.S. Bozin, S.J. Rosenthal and S.J.L. Billinge, *Phys. Chem. Chem. Phys.*, **2013**, 15, 8480

[29] J. Luo, M.M. Maye, V. Petkov, N.N. Kariuki, L. Wang, P. Njoki, D. Mott, Y. Lin and C.J. Zhong, *Chemistry of Materials*, **2005**, 17, 3086

[30] C.D. Martin, S.M. Antao, P.J. Chupas, P.L. Lee, S.D. Shastri and J.B. Parise, *Appl. Phys. Lett*,. **2005**, 86, 061910

[31] H.K. Mao, R.J. Hemley, Y. Fei, J.F. Shu, L.C. Chen, A.P. Jephcoat and Y. Wu, *Journal of Geophysical Research*, **1991**, 96, 8069-8079